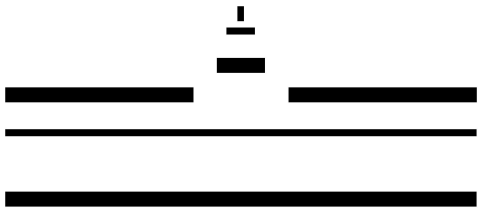

Westfälische
Wilhelms-Universität
Münster

Master's thesis

# Investigations of Time-of-Flight Methods for the KATRIN Experiment

Untersuchung von Flugzeitmethoden für das KATRIN-Experiment

Alexander Fulst

26.08.2016

Institut für Kernphysik
der Westfälischen Wilhelms-Universität Münster

Themensteller: Prof. Dr. Christian Weinheimer
Zweitgutachter: Prof. Dr. Alexander Kappes

# Contents

# 1. Introduction

Neutrinos belong to the most exciting particles in modern astro- and particle physics as well as in cosmology. Since their postulation by Wolfgang Pauli in 1930 and their first direct detection in the Cowan-Reines neutrino experiment in 1956, many investigations have been launched in order to examine the properties of these particles. In 1998 the first evidence for neutrino flavor oscillation was announced by the Super-Kamiokande Collaboration [SK98], which was confirmed for solar neutrinos by the Sudbury Neutrino Observatory in 2001 [SNO01]. For these findings, which imply a nonzero neutrino mass, the Nobel Prize for Physics was awarded to Arthur B. McDonald and Takaaki Kajita in 2015. Since oscillation experiments are only able to determine the difference between the squared masses, the absolute mass scale has to be ascertained by other means and is being searched for by many current and future experiments. Even though neutrinos are much lighter than any other known massive particles, their high abundance of $336\,\mathrm{cm}^{-3}$ provides for a significant impact on structure formation. Furthermore there are other interesting topics directly linked to the neutrino mass, e.g. the see-saw mechanisms in particle physics to explain the smallness of the observed mass limits or the possible Majorana nature of neutrinos.

Although there are different ways to obtain the neutrino mass, many of the strongest limits today are model-dependent. The **KA**rlsruhe **TRI**tium **N**eutrino (KATRIN) experiment utilizes electrons created by tritium beta decay to measure the neutrino mass in a model-independent way. The aim of KATRIN is to achieve a sensitivity for the upper limit of 200 meV, with a 90% confidence level, and a discovery potential of 350 meV with $5\sigma$ significance. In order to reach the ambitious goal of 200 meV the KATRIN experiment needs to improve the results of its predecessor experiments in Mainz and Troitsk, which set an upper limit of around 2 eV, by two orders of magnitude, since the measured observable is $m^2(\nu_\mathrm{e})$.

The present thesis focuses on investigations questioning whether nonstandard operation or a possible upgrade of the KATRIN experiment would be able to push the sensitivity even further with reasonable additional effort.

# 2. Neutrino Physics

Before describing the KATRIN experiment in general and time-of-flight methods in particular, a brief introduction to neutrino properties and the history of neutrino physics will be given.

## 2.1. Postulation and Experimental Discovery

The postulation of neutrinos in 1930 followed the observation that products from beta decays (electron and daughter nucleus) have continuous energy and momentum spectra. Since for a two particle decay energy, momentum and angular momentum of the two particles are fixed by conservation laws, this observation could only be explained by introducing a third particle that carries a part of the total energy and momentum released in the decay. Hence, Pauli wrote down the $\beta$-decay as

$$n^0 \rightarrow p^+ + e^- + \bar{\nu}_\mathrm{e}\,, \tag{2.1}$$

where $\bar{\nu}_\mathrm{e}$ is the electron antineutrino. Because the neutrino is neutral in charge and the weak interaction is very short-ranged its cross section is very small. Therefore, it was clear at that time that it would be very hard to directly detect neutrinos in an experiment. To compensate for the small cross section of the weak interaction an experiment needs to exploit a huge detector-mass or a very strong neutrino source, neither of which where available in the beginning of the 1930s.

It took until 1956 until the Cowan-Reines neutrino experiment, utilizing the Savannah River reactor in South Carolina, delivered direct evidence for the existence of neutrinos [RC59] through observation of the inverse beta decay

$$\bar{\nu}_\mathrm{e} + p^+ \rightarrow n^0 + e^+\,. \tag{2.2}$$

In the Cowan-Reines experiment, the process written down in equation (2.2) on the preceding page took place inside two plastic target tanks filled with cadmium chloride dissolved in water. The water provides protons for the interaction with the electron antineutrino, while the cadmium serves as absorber for the created neutrons. The target tanks were sandwiched between scintillation detectors equipped with photo multipliers [RC97].

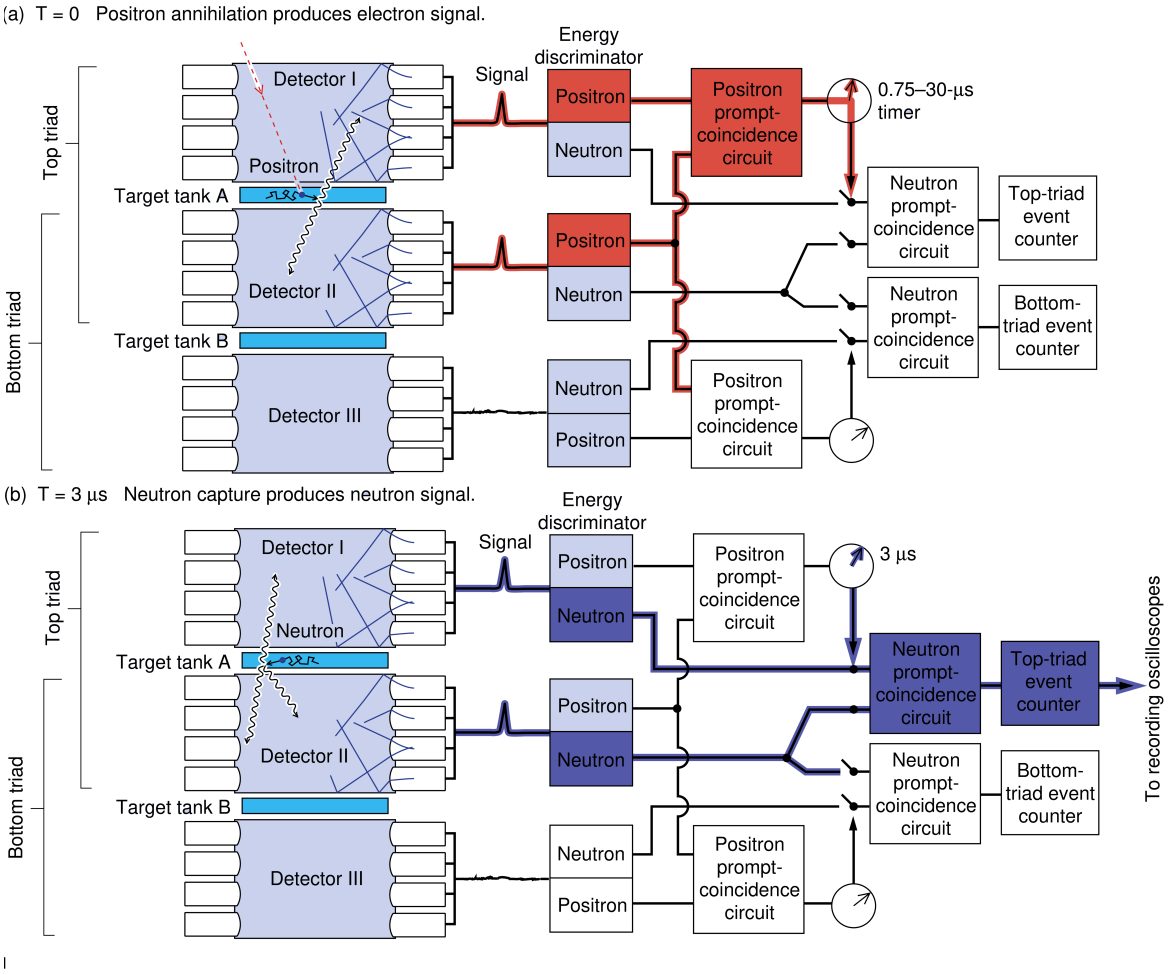


**Figure 2.1.** – **Delayed-Coincidence Signals from Inverse Beta Decay:** (a) positron annihilation, (b) neutron capture[RC97]

When an incoming electron antineutrino (red dotted line in figure 2.1 (a)) causes an inverse $\beta$-decay in one of the tanks, the created positron annihilates with a nearby electron, resulting in two photons (curly lines in figure 2.1 (a)), which are detected in the adjacent scintillation detectors. The neutron is moderated by the water and captured by a cadmium atom, which then de-excites through emission of $\gamma$'s. These photons are again detected by the neighboring scintillators and the time passed since the positron signal is used to differentiate between a coincidence and a random event. The third detector can be used as a veto to suppress background from cosmic rays,

which has been a problem in previous experiments, since $\gamma$'s from positron annihilation or neutron capture are too low in energy to reach the third scintillator.

Shortly after this breakthrough the muon neutrino has been discovered in 1962 after being postulated previously. The DONUT collaboration at Fermilab finally confirmed the existence of the tau neutrino in 2001, thus finding the last missing lepton in the Standard Model [DON01].

## 2.2. Neutrino Mass and Flavor Oscillations

When Wolfgang Pauli first postulated the electron neutrino (originally under the name *neutron*), he suggested the mass to be of the same order of magnitude as the electron mass and definitely lower than 1% of the proton mass [Pau30]. However, after its discovery the neutrino has been assumed massless in the Standard Model for several decades, until first evidence for neutrino oscillation was supplied by the Super-Kamiokande experiment in 1998. This has later been confirmed by the Sudbury Neutrino Observatory and several other independent experiments.

### 2.2.1. The Solar Neutrino Problem

The Sun, as all stars, generates light and heat through nuclear fusion. The main process powering stars the size of the Sun is the proton-proton chain reaction [LeB10]:

$$4p \rightarrow^4 \mathrm{He} + 2e^+ + 2\nu_\mathrm{e} + 26.732\,\mathrm{MeV}\,. \tag{2.3}$$

The neutrinos emitted in this process can be measured in an experiment on the Earth, for example in the Homestake experiment, which was the first one to detect solar neutrinos in the late 1960s. In order to achieve this, a $380\,\mathrm{m}^3$ tank of perchloroethylene was placed in the Homestake Gold Mine in South Dakota. The underground location was chosen in order to reduce background from cosmic rays, while neutrinos travel through the ground with nearly no interaction because of their very small cross section. An incoming electron neutrino can interact with a chlorine-37 atom, resulting in an argon-37 atom and an electron:

$$\nu_\mathrm{e} + {}^{37}\mathrm{Cl} \rightarrow {}^{37}\mathrm{Ar} + e^-\,. \tag{2.4}$$

Since the created argon isotope is radioactive, extracting it and measuring the decay rate gives information about the number of neutrino interactions inside the tank and thus about the neutrino flux. It was found that the measured value for the flux was only about one third of the one predicted by theory and this discrepancy became known as the *solar neutrino problem*.

### 2.2.2. Neutrino Flavor Oscillation

After excluding errors in the calculations and a malfunction in the experiment, a possible solution to the solar neutrino problem was neutrino oscillations. Until now the word neutrino was used to refer to a certain flavor eigenstate $\nu_\alpha$ ($\alpha = e,\mu,\tau$), but to explain oscillations, neutrinos need to have a second set of eigenstates, namely mass eigenstates $\nu_i$ ($i = 1,2,3$).

The flavor eigenstates can now be written as superposition of mass eigenstates connected by a unitary $3 \times 3$ mixing matrix $U$, analogous to the CKM-matrix in the quark sector [OW08]:

$$|\nu_\alpha\rangle = \sum_i U_{\alpha i} |\nu_i\rangle \ . \tag{2.5}$$

For the neutrino sector $U$ is called Pontecorvo-Maki-Nakagawa-Sakata (PMNS) matrix and, in case of Dirac neutrinos, can be written as

$$U = \begin{pmatrix} c_{12}c_{13} & s_{12}c_{13} & s_{13}e^{-\imath\delta} \\ -s_{12}c_{23} - c_{12}s_{23}s_{13}e^{\imath\delta} & c_{12}c_{23} - s_{12}s_{23}s_{13}e^{\imath\delta} & s_{23}c_{13} \\ s_{12}s_{23} - c_{12}s_{23}s_{13}e^{\imath\delta} & -c_{12}s_{23} - s_{12}c_{23}s_{13}e^{\imath\delta} & c_{23}c_{13} \end{pmatrix} , \tag{2.6}$$

where $c_{ij}$ is the cosine and $s_{ij}$ the sine of the mixing angle $\theta_{ij}$ and the phase $\delta$ accounts for a possible CP-violation, which has not been observed yet. In case neutrinos are Majorana particles, i.e. they are identical to their antiparticles, equation (2.6) has to be multiplied by the additional matrix

$$\begin{pmatrix} e^{\imath\alpha_1/2} & 0 & 0 \\ 0 & e^{\imath\alpha_1/2} & 0 \\ 0 & 0 & 1 \end{pmatrix} , \tag{2.7}$$

with the Majorana phases $\alpha_1$ and $\alpha_2$. However, these phases do not influence oscillation and are therefore neglected in further calculations.

For oscillation experiments, it is necessary to examine how a given initial flavor eigenstate changes with time. Since the flavor eigenstates are not eigenstates of the time

evolution operator, the mass eigenstates $|\nu_i\rangle$ are used. Their propagation can be expressed using plane waves:

$$|\nu_i(t)\rangle = e^{-\imath(E_i t - \vec{p_i}\vec{x})} |\nu_i(0)\rangle \ . \tag{2.8}$$

Applying the relativistic approximation $p_i \gg m_i$ gives

$$E_i = \sqrt{p_i^2 + m_i^2} \approx p_i + \frac{m_i^2}{2p_i} \approx E + \frac{m_i^2}{2E} \tag{2.9}$$

for the energy $E_i$ of a mass eigenstate, with the total energy $E$ of the particle. Additionally using $L \coloneqq x = c \cdot t$ for the traveled distance, equation (2.8) can be rewritten as:

$$|\nu_i(L)\rangle = e^{-\imath m_i^2 L/2E} |\nu_i(0)\rangle \ . \tag{2.10}$$

The probability that a flavor eigenstate $\alpha$ is transformed into flavor eigenstate $\beta$ is now given by

$$P_{\alpha\to\beta} = |\langle\nu_\beta(L)|\nu_\alpha\rangle|^2 = \left|\sum_i U_{\alpha i} U_{\beta i}^* e^{\imath m_i^2 L/2E}\right|^2 , \tag{2.11}$$

which can be expanded to

$$\begin{aligned} P_{\alpha\to\beta} = \delta_{\alpha_\beta} &- 4\sum_{i>j} \mathrm{Re}(U_{\alpha i} U_{\beta i}^* U_{\alpha j}^* U_{\beta j}) \sin^2\left(\frac{\Delta m_{ij}^2 L}{4E}\right) \\ &+ 2\sum_{i>j} \mathrm{Im}(U_{\alpha i} U_{\beta i}^* U_{\alpha j}^* U_{\beta j}) \sin\left(\frac{\Delta m_{ij}^2 L}{2E}\right) , \end{aligned} \tag{2.12}$$

with $\Delta m_{ij}^2 = m_i^2 - m_j^2$ as difference of the squared masses of $i$ and $j$.

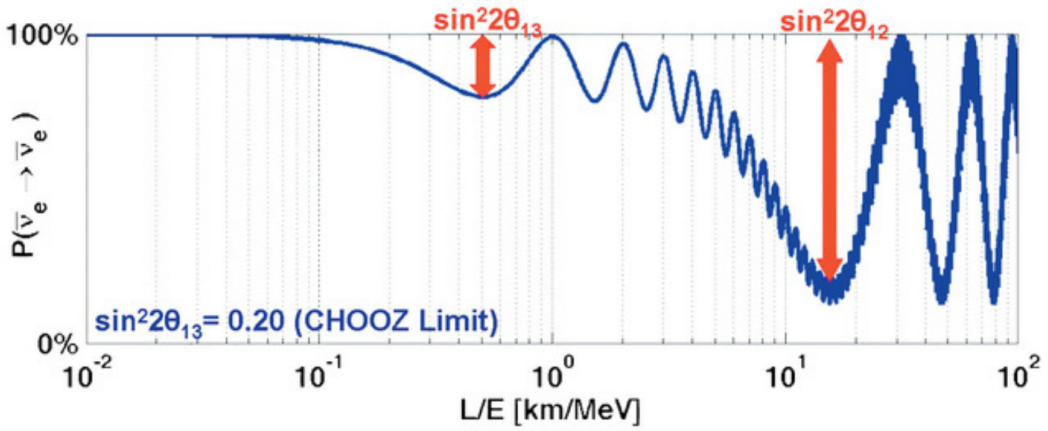


**Figure 2.2.** – **Transition probability for the $\bar{\nu}_e \to \bar{\nu}_e$ process:** For small $L$ to $E$ proportions, the probability to remain in the initial flavor eigenstate is nearly 1. As the L/E value rises, the probability starts oscillating and transition to other flavor eigenstates becomes allowed [KAT06].

The first experimental evidence for neutrino oscillations was provided by the Super-Kamiokande collaboration in 1998 [SK98]. Built from 11146 photomultiplier tubes and 50000 tons of ultra-pure water, the Super-Kamiokande experiment was used to detect atmospheric electron and muon neutrinos through Cherenkov radiation created by charged particles that are produced in reactions of neutrinos with the water target.

These neutrinos are created in the atmosphere by cosmic rays (which mainly consist of protons) interacting with atoms or molecules of the air. One example reaction in which neutrinos are created is shown in figure 2.3.

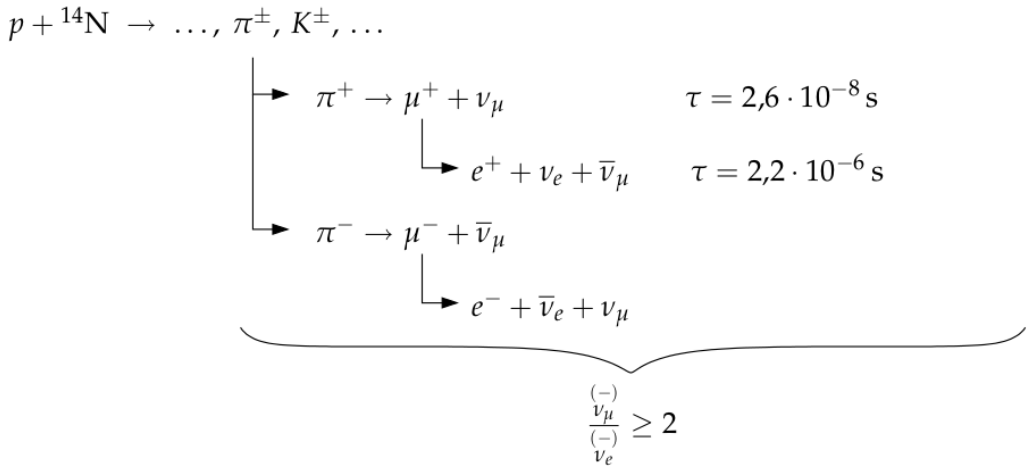


**Figure 2.3.** – **Example for an atmospheric neutrino creating reaction:** a primary reaction between a nitrogen atom and an incoming proton results in pions, which subsequently decay into $e^-, e^+$ and neutrinos [Wes15].

It was found that the flux for upward[1] and downward moving electron neutrinos matched the theoretical expectation. For muon neutrinos however, there was a deficit in upward moving particles. This is a hint to a $\nu_\mu \rightarrow \nu_\tau$ transformation while the neutrinos travel through the Earth. Using a best-fit method on the Super-Kamiokande data results in the following values for $\Delta m^2_{23}$ and the mixing angle $\theta_{23}$ [SK12]:

$$\Delta m^2_{23} = 2.11 \cdot 10^{-3}\,\mathrm{eV}^2 \tag{2.13}$$

$$\sin^2(\theta_{23}) = 0.525\,. \tag{2.14}$$

The mixing angle is unexpectedly large compared to the rather small mixing angles in the CKM matrix.

Unfortunately, the Super-Kamiokande experiment was not sensitive to tau neutrinos, so only a deficit in muon neutrinos could be observed, but not the implied surplus of tau

[1] Upward moving neutrinos are particles created in the atmosphere on the other side of the Earth, which travel through the ground and enter the detector from underneath.

neutrinos. In May 1999 the Sudbury Neutrino Observatory (SNO) started investigating high energetic neutrinos created in the decay of $^8$B in the sun and was sensitive to the total flux of all neutrino flavors as well as to electron neutrinos only. Therefor a tank filled with 1000 tons of heavy water was observed by about 9600 photomultiplier tubes to detect three different types of interactions, namely the **c**harged **c**urrent interaction (CC, equation (2.15)), the **n**eutral **c**urrent interaction (NC, equation (2.16)) and elastic **e**lectron **s**cattering (ES, equation (2.17)).

$$\nu_\mathrm{e} + d \to p + p + e^- \tag{2.15}$$

$$\nu_\alpha + d \to p + n + \nu_\alpha \tag{2.16}$$

$$\nu_\alpha + e^- \to \nu_\alpha + e^- \tag{2.17}$$

In the charged current interaction, an electron neutrino is absorbed by deuterium, transforming its neutron into a proton while emitting a high energetic electron, which can be detected through emission of Cherenkov radiation. Since neutrinos produced in the $^8$B decay only have energies up to 14.6 MeV, which is lower than the muon or tau rest mass, this reaction can only be induced by electron neutrinos.

Independent of its flavor, a neutrino can dissociate a deuteron into a proton and a neutron. The neutron can be captured by another deuteron, resulting in a characteristic photon with an energy of 6.25 MeV, which can be detected by the photomultiplier tubes.

In case of elastic scattering, a neutrino interacts with an atomic electron through weak interaction and accelerates it. Neutrinos of all flavors can exchange a $Z^0$ boson with the electron, but only the electron neutrino can additionally exchange a $W^-$ boson, so although elastic scattering is sensitive to all flavors, it is dominated by electron neutrinos.

Comparing the measured total flux to the electron neutrino flux results in the factor [SNO13]:

$$\frac{\phi(\nu_\mathrm{e})}{\phi(\nu_\mathrm{e}) + \phi(\nu_\mu) + \phi(\nu_\tau)} = 0.347 \pm 0.029\,. \tag{2.18}$$

Since the fusion reactions in the Sun only produce electron neutrinos, the measurement of other neutrino flavors proves that neutrinos indeed oscillate and, due to the $\Delta m^2_{ij}$ dependence of the oscillation probability in equation (2.12) on page 7, must have a nonzero mass. Additionally, the measured overall flux is in accordance with the prediction made by the Solar Standard Model.

Besides the production of neutrinos by the processes in the Sun and the atmosphere described above, neutrinos can also be produced in particle accelerators and nuclear fission reactors. MINOS and OPERA are two experiments where accelerated protons are collided with a target to create pions and kaons, which mainly decay into muon neutrinos. MINOS consists of two detectors, one a few hundred meters away from the target at Fermilab in Illinois and one in the Soudan mine in Northern Minnesota, and measures the disappearance of muon neutrinos and the appearance of electron neutrinos. OPERA observes taus produced by tau neutrino interactions and thus examines the transformation of $\nu_\mu$ into $\nu_\tau$. The KamLAND experiment at the Kamioka Observatory uses 53 nearby commercial nuclear reactors as electron antineutrino sources and also looks for their disappearance.

The currently best-fitting parameters for a three neutrino mixing with normal mass ordering are listed in table 2.1.

**Table 2.1.** – **Best-fit neutrino oscillation parameters:** The best-fit values of the 3-neutrino oscillation parameters, derived from a global fit of the current neutrino oscillation data (from [Cap+14]). The definition of $\Delta m^2$ used is: $\Delta m^2 = m_3^2 - (\Delta m_2^2 + \Delta m_1^2)/2$ [Oli+14].

| Parameter | best-fit ($\pm 1\sigma$) |
|---|---|
| $\Delta m_{21}^2$ | $7.54^{+0.26}_{-0.22} \cdot 10^{-5}\,\mathrm{eV}^2$ |
| $\lvert\Delta m^2\rvert$ | $(2.43 \pm 0.06) \cdot 10^{-3}\,\mathrm{eV}^2$ |
| $\sin^2(\theta_{12})$ | $0.308 \pm 0.017$ |
| $\sin^2(\theta_{23})$ | $0.437^{+0.033}_{-0.023}$ |
| $\sin^2(\theta_{13})$ | $0.0234^{+0.0020}_{-0.0019}$ |
| $\delta/\pi$ | $1.39^{+0.38}_{-0.27}$ |

### 2.2.3. The Neutrino Mass Scale

All of the aforementioned experiments show clear indications of neutrino oscillation and imply neutrinos with a finite mass. However, since they are oscillation experiments, neither of them can make a statement about the absolute mass scale of neutrinos, as only the mass square difference goes into equation (2.12) on page 7. While from observations of high-energy solar neutrinos the absolute value of $m_{21}^2$ can be determined due to the influence of the **M**ikheyev-**S**mirnov-**W**olfenstein effect, it is not known whether the eigenstate masses are in normal ($m_1 < m_2 < m_3$) or inverted ($m_3 < m_1 < m_2$) order. This is known as neutrino mass hierarchy problem.

Today, there are several different experiments, in progress or being prepared, trying to find the neutrino mass or at least improve the upper limit. All of them fall into one of three categories:

- **Cosmological observations:** Analyzing cosmological data, e.g. from the cosmic microwave background radiation, the Lyman-alpha forest or structure formation, leads to an upper limit for the sum of the neutrino masses. One of the currently best constraints is $\sum_i m(\nu_i) < 0.29\,\mathrm{eV}$ from [Sør+12]. Nevertheless, limits from cosmological observations are highly model-dependent.

- **Neutrinoless double beta decay ($0\nu\beta\beta$):** An alternative approach is to investigate the decay of special isotopes, e.g. $^{76}$Ge at the GERDA experiment, which are stable under normal beta decay, but can perform a double beta decay:

$$(Z,A) \rightarrow (Z+2,A) + 2e^- \,(+2\nu_\mathrm{e})\,. \tag{2.19}$$

  If neutrinos are Majorana particles, this can happen without emission of any neutrino and the rate of such a decay is given by

$$\Gamma = G|M|^2|m_\mathrm{ee}|^2\,, \tag{2.20}$$

  which depends on the coherent sum of neutrino mass eigenstates

$$m_\mathrm{ee}^2 = \left|\sum_i U_{\mathrm{e}i}^2 m(\nu_i)\right|^2\,. \tag{2.21}$$

  The GERDA collaboration found a lower limit of $2.1\cdot10^{25}$ (90% C.L.) years for the half life of this decay and till now it remains unknown if neutrinos are Majorana particles [Ago+13].

  A drawback of this method is the large uncertainty of the nuclear matrix elements required to extract $m_\mathrm{ee}^2$ and the possibility of destructive interference in the coherent sum of the mass eigenstates.

- **Measurement of the $\beta$ spectrum:** Another way to investigate the neutrino mass is to carefully measure the energy spectrum of the $\beta$-decay. Since this method is entirely based on relativistic kinematics, it is model-independent. Because the neutrino mass is nonzero, the neutrino takes at least its rest mass from the total decay energy. This means that the upper limit for the electron energy is directly connected to the effective

electron neutrino mass

$$m^2(\nu_\mathrm{e}) = \sum_i |U_{\mathrm{e}i}|^2 m(\nu_i)^2 \tag{2.22}$$

through the energy conversation law. Unfortunately the maximal value of the electron energy cannot be measured directly, because of very low statistics at the endpoint and an inevitable background. Consequently, it is necessary to measure a larger part of the energy spectrum down to several eV below the endpoint. By using Fermi's golden rule and neglecting the recoil energy because of the much higher mass of the nucleus compared to the electron and neutrino masses and the final state distribution of the daughter nucleus, the $\beta$ spectrum can be written as [OW08]:

$$\frac{\mathrm{d}\dot{N}}{\mathrm{d}E} = R(E) \cdot \sqrt{(E_0 - E) - m^2(\nu_\mathrm{e})} \cdot \Theta(E_0 - E - m^2(\nu_\mathrm{e}))\,, \tag{2.23}$$

$$\text{with } R(E) = \frac{G_F^2}{2\pi^3} \cos^2(\vartheta_C) |M|^2 F(Z+1,E) p(E + m_\mathrm{e})(E_0 - E)\,. \tag{2.24}$$

Here, $E$ is the energy of the electron, $E_0$ the endpoint energy of the $\beta$ spectrum, $G_F$ the Fermi constant, $\vartheta_C$ the Cabibbo angle, $M$ the nuclear matrix element, $Z$ the atomic number of the daughter nucleus and $m_\mathrm{e}$ the electron rest mass.

It is noteworthy that the effective neutrino mass $m(\nu_\mathrm{e})$ does not only affect the maximal electron energy, but also the shape of the beta spectrum, as illustrated for tritium in figure 2.4 on the next page.

It can also be seen that only a very small fraction of all decay electrons are located in the endpoint region. In the case of tritium, only about $2 \cdot 10^{-13}$ of the total decays are located in the interval of the last 1 eV. While in principle it is possible to use any beta decay for this kind of experiments, some isotopes have properties which make them more suitable than others. The KATRIN experiment for example, as well as its predecessors at Mainz and Troitsk, uses the tritium decay

$$^3\mathrm{H} \rightarrow {}^3\mathrm{He}^+ + e^- + \bar{\nu}_\mathrm{e} \tag{2.25}$$

because of the following reasons:

- The low endpoint of around 18575 eV entails that comparably many electrons with energies near the endpoint are produced, reducing the aforementioned problem of low statistics. The only isotope with an even lower endpoint of $E_0 = 2470\,\mathrm{eV}$ is $^{187}$Re [Gal+00]. $^{163}$Ho with a Q value of 2833 eV for electron capture represents another noteworthy isotope used in neutrino mass experiments [Eli+15].

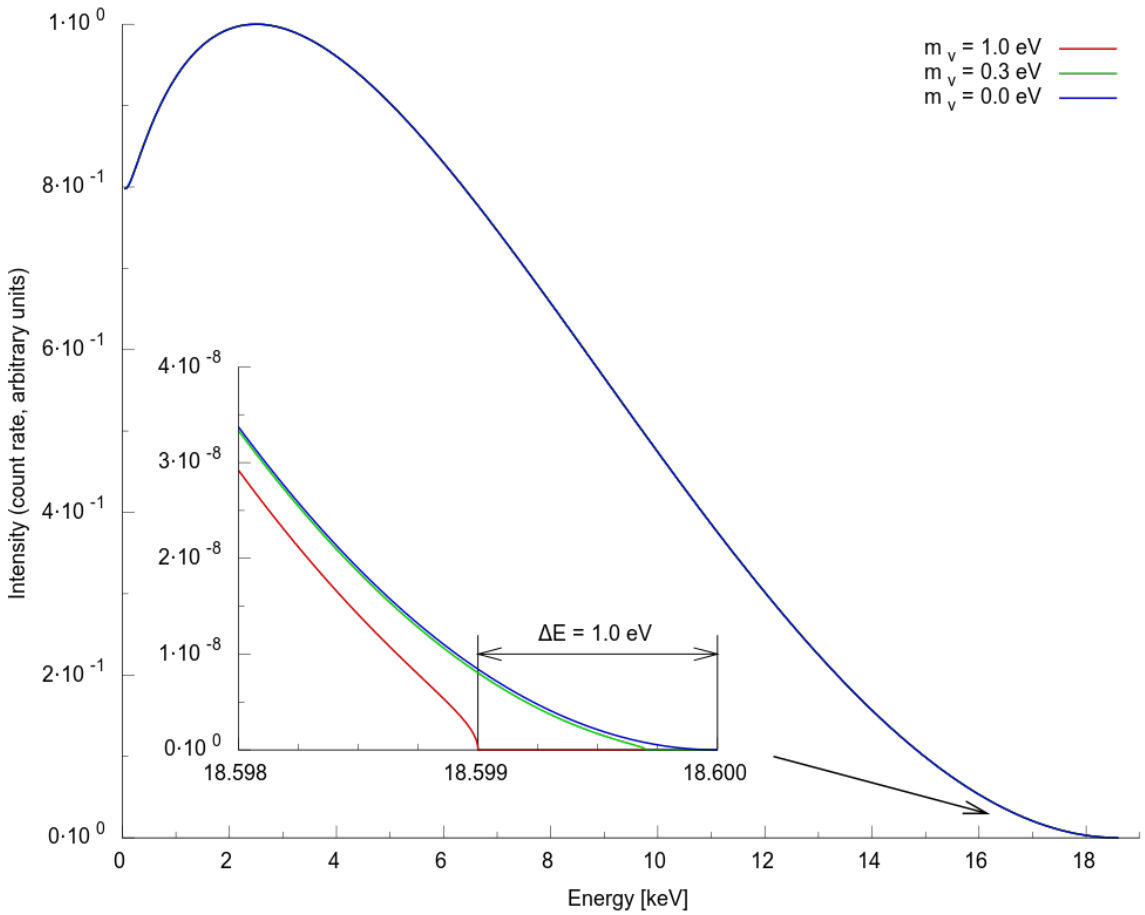


**Figure 2.4.** – **Energy spectrum of the tritium beta decay:** The energy spectrum for an endpoint energy of $E_0 = 18600\,\text{eV}$ and three different neutrino masses. The inset shows that both the maximal value for the electron energy, as well as the shape are dependent on the neutrino mass [Beh12].

- The simple atomic structures of tritium and $^3$He allow for precise calculations of atomic corrections.

- Tritium has a rather small half life time of 12.3 years, enabling the construction of strong, yet manageable sources in order to gain statistics.

- For super-allowed transitions like in the case of the tritium $\beta$-decay, the nuclear matrix element $M$ in equation (2.24) on the facing page is independent of the decay electron energy.

- Tritium has a low nuclear charge, reducing inelastic scattering of the produced electrons in the source.

Currently the best laboratory limits on the effective electron neutrino mass are given by the Mainz and Troitsk experiments, reaching a 2 eV limit with 95% confidence level

[Kra+05; Ase+11]. The KATRIN experiment aims to improve the mass limit by a factor of 10 by using the same measurement principle as these experiments and will be explained in detail in the next chapter of this thesis.

Since a lot of advances in cryo-bolometer development and production took place in recent years, their application in neutrino mass experiments becomes increasingly interesting. To compensate for the complicated electronic structure of $^{187}$Re and $^{163}$Ho the total released energy, except the one carried away by the neutrino, has to be measured to take advantage of the lower endpoint [Dre+13]. Cryo-bolometers are suitable to perform this task with a high energy resolution and will be used in upcoming experiments like ECHo [G+14].

# 3. The KATRIN Experiment

As mentioned in the previous section, the **KA**rlsruhe **TRI**tium **N**eutrino experiment (KATRIN), located at the Karlsruhe Institute of Technology, aims to improve the current upper neutrino mass limit down to 200 meV (90% C.L.) with model-independent measurements of the beta decay kinematics of tritium. The discovery potential will be around 0.35 eV with $5\sigma$ or at 0.3 eV with $3\sigma$ significance [Kat04]. While the Mainz and Troitsk experiments were based on the same idea of using a MAC-E energy filter to measure the integrated beta spectrum, KATRIN will improve the sensitivity on $m^2(\bar{\nu}_e)$ by a factor of 100. To reach this ambitious goal, many things have to be improved throughout the whole experiment from the source to the detector.

In the next section an overview over the experimental setup, together with a brief description of the different subsystems will be given. Afterwards, the MAC-E filter principle will be discussed in detail, because it is especially important for this thesis.

## 3.1. Experimental Setup and Structure of KATRIN

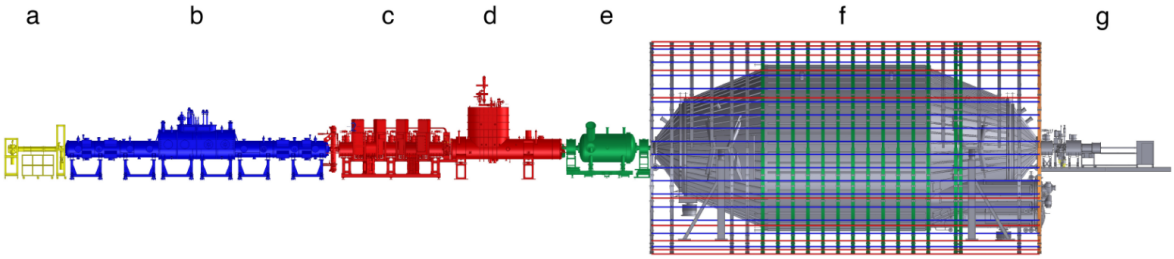


**Figure 3.1. – Schematic overview of the KATRIN experiment:** (a) **r**ear **s**ection (RS), (b) **w**indowless **g**aseous **t**ritium **s**ource (WGTS), (c) **d**ifferential-**p**umping **s**ection (DPS), (d) **c**ryogenic-**p**umping **s**ection (CPS), (e) **p**re-**s**pectrometer (PS), (f) **m**ain **s**pectrometer (MS) and air-coil system, (g) **f**ocal-**p**lane **d**etector system (FPD) [Ams+15].

The KATRIN experiment can be divided into two larger sections, namely the ***S**ource and **T**ransport **S**ection* (STS, (a) to (d) in figure 3.1) located in the **T**ritium **L**aboratory

**K**arlsruhe (TLK) and the ***S**pectrometer and **D**etector **S**ection* (SDS, (e) to (g) in figure 3.1 on the preceding page) placed in the adjacent KATRIN spectrometer hall. These two sections are physically divided by a wall between the cryogenic-pumping section and the pre-spectrometer with only a hole for the beamline due to radiation safety reasons. Both major sections can be divided further into smaller segments as shown in figure 3.1 on the previous page.

### 3.1.1. Rear Section

The rear section contains an electron gun for calibration purposes. It produces electrons that fly through the whole experiment and are used to determine the column density in the WGTS as well as the response function of the whole experiment. Additionally, the rear section monitors the source activity through incoming electrons.

### 3.1.2. Windowless Gaseous Tritium Source

The WGTS contains a large amount of cold ($T = 30\,\mathrm{K}$) tritium gas of high purity ($> 95\%$) in a 10 m long steel tube with a diameter of 90 mm [Gro+11]. It is designed to achieve a high activity of $10^{11}\,\mathrm{Bq}$, to deliver about $10^{10}\,\mathrm{e^{-}s^{-1}}$ into the acceptance of the spectrometers. The demand for such a high activity is the reason for the KATRIN experiment to be placed in Karlsruhe, since the TLK is the only facility in Europe providing the necessary tritium infrastructure and the required license to handle the high amount of tritium used in the experiment[Kat04].

The $^3H_2$ gas is injected in the middle of the source and diffuses to both ends of the WGTS, where it is pumped out by turbomolecular pumps and purified. To reach the design sensitivity of the experiment, the planned column density of $\rho d = 5 \cdot 10^{17}\,\mathrm{molecules/cm^2}$ has to be known down to a precision of 0.1%, because the column density determines the count rate and influences the scattering probability of decay electrons. The needed temperature stability of 30 mK is reached by a two-phase neon cooling system. The created electrons are adiabatically guided to both ends of the source by a magnetic field of 3.6 T, with the guided flux tube reaching $191\,\mathrm{Tcm^2}$.

### 3.1.3. Differential- and Cryogenic-Pumping Section

Since separating the source from the rest of the experiment through a window would lead to energy losses in it, reducing the obtainable sensitivity, the source was designed windowless. However, this creates another challenge because the turbomolecular pumps at the end of the WGTS are not sufficient to completely remove tritium from the following beamline. This presents a problem because a $^3$H atom decaying inside the spectrometer would lead to additional background. Therefore, special care has to be taken to reduce the tritium flow to a minimum.

Inside the **D**ifferential-**P**umping **S**ection (DPS), the beamline is bent and a turbomolecular pump at every corner pumps out the tritium as illustrated in figure 3.2.

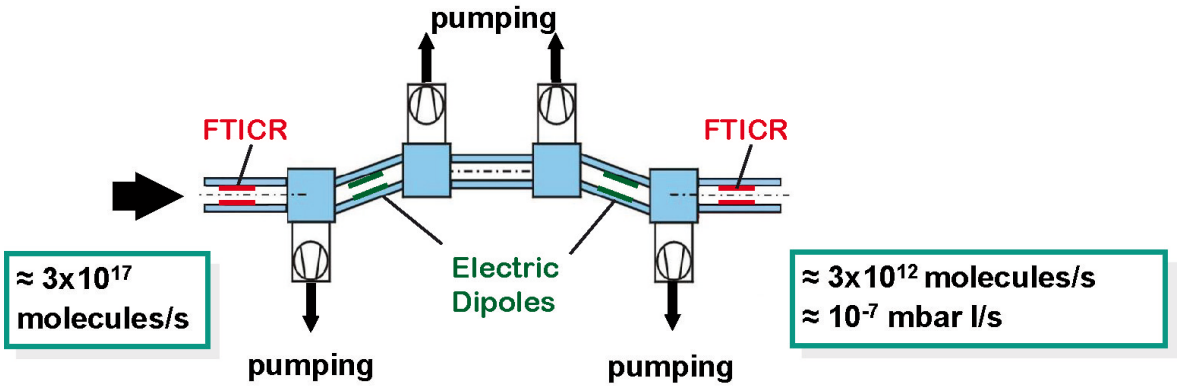


**Figure 3.2.** – **Schematic of the differential-pumping section:** Neutral tritium molecules flying in a straight line collide with the beamtube corners and are pumped out. Electric dipoles and **F**ourier **T**ransform **I**on **C**yclotron **R**esonators (FTICR) analyze and remove charged ions [Hac15; Kat16].

Electrons are magnetically guided through the bends and do not collide with the walls. The DPS is able to reduce the tritium flow by five orders of magnitude from $10^{-2}\,\mathrm{mbar\,l\,s^{-1}}$ down to $10^{-7}\,\mathrm{mbar\,l\,s^{-1}}$.

The reduced flow of $^3H_2$ molecules is still above the required levels, so the DPS is followed by a second pumping section, i.e. the **C**ryogenic-**P**umping **S**ection (CPS), shown in figure 3.3 on the next page.

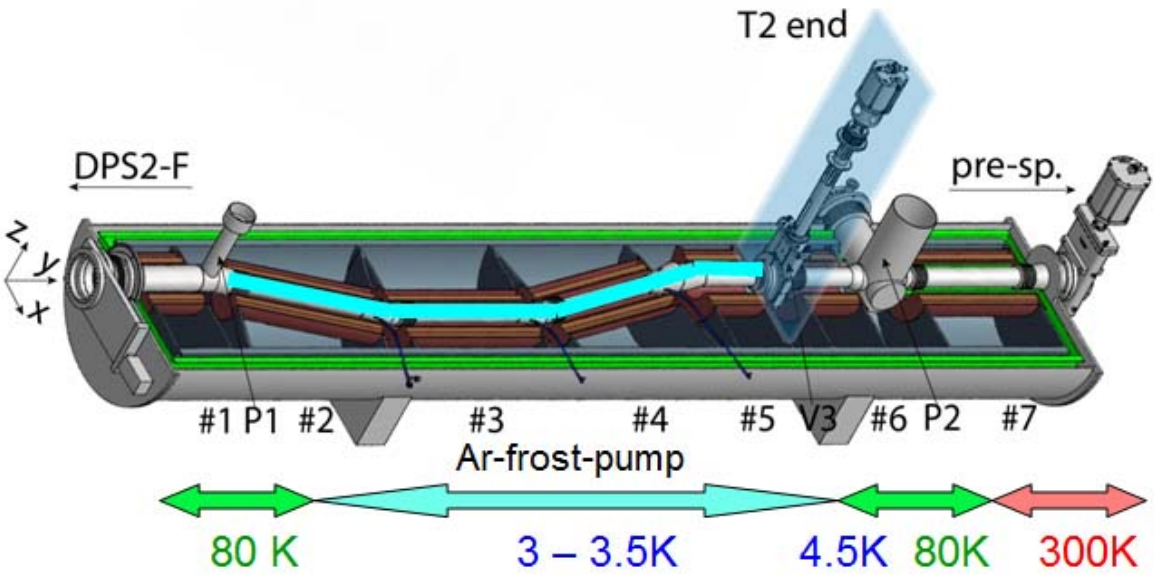


**Figure 3.3.** – **Schematic of the cryogenic-pumping section:** Besides the chicane concept also being employed in the DPS, the beamline parts below 4 K use a thin layer of Ar-frost for cryo-sorption of tritium [Kat16].

Tritium molecules colliding with the cooled down walls of the CPS are adsorbed by a layer of Ar-frost and hence are hindered from entering the spectrometer section. After 60 days of operation the Ar-frost layer is saturated and the beamline has to be heated up to 100 K to release the argon together with the tritium, which are then pumped out by turbomolecular pumps. Meanwhile the spectrometers are protected from tritium molecules by a closed valve to prevent a contamination. Afterwards the Ar-frost layer is newly prepared for the next cycle.

The partial pressure of tritium at the end of the CPS is reduced by a factor of $10^{14}$ compared to the center of the WGTS and the remaining tritium will generate a background rate of less than 1 mHz in the main spectrometer [Kat04; Val14].

### 3.1.4. The Pre-Spectrometer

The pre-spectrometer was constructed as one of the first parts for KATRIN, because it allowed for testing of new technologies, e.g. the wire electrode system also used in the main spectrometer, in a scaled down version. Like the main spectrometer it is also a MAC-E filter, but with a length of 3.4 m and an outer diameter of 1.7 m it is considerably smaller. Its magnetic field is defined by one 4.5 T magnet at each end and it is operated at a pressure of $10^{-11}$ mbar. Because the working principle is the same as the one of the main spectrometer, the pre-spectrometer was used for studies

on background reduction techniques and examination of the electro-magnetic design, e.g. to prevent Penning traps inside the spectrometer volume.

Besides the possibility to test a lot of things, the pre-spectrometer will be placed in the beamline of KATRIN to reduce the electron load on the main spectrometer. It is planned to set its retarding voltage to a value about 300 V below the endpoint, where the low energy resolution of around $\Delta E = 100\,\mathrm{eV}$ does not affect the overall sensitivity, since the endpoint region is solely analyzed by the main spectrometer. This reduces the electron flux to $10^3\,\mathrm{s}^{-1}$, which also lowers the amount of residual gas ionization in the main spectrometer. Hence, the background is cut down significantly. On the downside, this electro-magnetic configuration intrinsically creates a Penning trap between the two spectrometers, which can lead to a storage of electrons, increasing the background again. A lot of effort is placed into investigations on the removal of stored particles via tools like an electron catcher, a wire scanner or a pulsed coil [Hil11; Beh12], yet it is not decided if the pre-spectrometer will be operated at a high, low or even zero retarding potential. Further testing of electron removal options will be carried out in the near future to see how much they can reduce Penning trap related background.

### 3.1.5. The Main Spectrometer

The main spectrometer is the primary tool for energy analysis and provides the needed energy resolution of $\Delta E = 0.93\,\mathrm{eV}$. Consisting of a 23 m long tank with a diameter of 9.8 m and an attached inner wire electrode system, the main spectrometer represents the world's largest UHV recipient. To reach the nominal pressure of $10^{-11}$ mbar, the tank bears three dedicated pump ports and can be heated up to 350 °C.

At the exit of the main spectrometer lies the pinch magnet, delivering the strongest magnetic field of the whole experiment with a flux density of 6 T, rejecting electrons with polar angles in the source larger than 51° relative to the magnetic field direction. In the middle of the tank this field is reduced by a factor of 20000, defining the energy resolution as explained in section 3.2. Air coils surrounding the tank are used to fine tune the shape and strength of the magnetic field and to compensate for the Earth's magnetic field, while the inner electrode system allows to finely shape the electric potential inside the spectrometer and ensures a low background from cosmic rays, environmental radioactivity and radioactive impurities by reflecting secondary electrons produced by interactions of the primary particles with the tank back to the wall. In order to shape the potential, the inner electrode system is divided into 15 rings along the beam axis of which the central five ones (7-11) are connected, resulting

in the ability to apply eleven individual potentials. This feature is used in section 5, where a time-dependent potential is used on rings 12-16. Additionally the electrode system is split into two dipoles, allowing an asymmetric potential setting, which will not be used here. Figure 3.4 illustrates how the inner wire electrode system is built up and shows the separation into different rings.

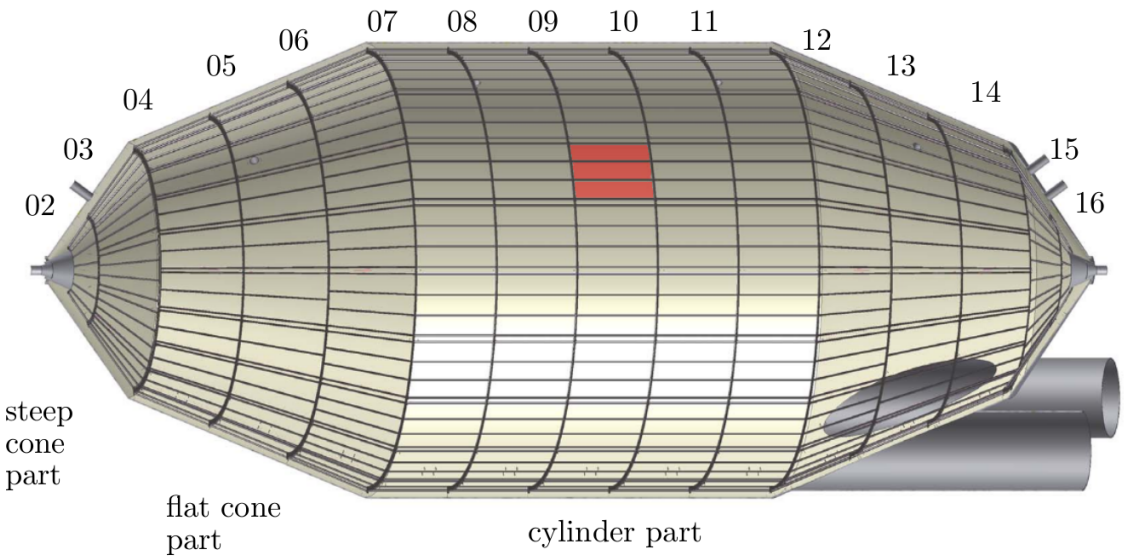


**Figure 3.4. – Cutaway drawing of the main spectrometer, revealing the inner electrode system:** The main spectrometer is shown without the surrounding vessel. Each ring is made up of several modules, one of which is highlighted in red. The tubes visible on the lower right represent the pumping ports [Zac09].

Depending on the retarding voltage, the electron flux is reduced down to $< 1\,\mathrm{s}^{-1}$ at the detector side.

### 3.1.6. The Focal-Plane Detector System

In principle the KATRIN detector only has to count arriving electrons, since the main spectrometer does the energy analysis. Nonetheless, to reach the full sensitivity of 200 meV the detector system has to be more sophisticated.

The core part of the system consists of a 148-pixel p-i-n-diode array on a single silicon wafer with a mean energy resolution of $(1.52 \pm 0.01)\,\mathrm{keV}$ (FWHM) at 18.6 keV and an efficiency of $95.0\% \pm 1.8\%_{\mathrm{stat}} \pm 2.2\%_{\mathrm{syst}}$ [Ams+15]. The energy resolution helps to discriminate between signal and background electrons and the spatial resolution given by the pixel design allows for independent calibration depending on the way

electrons take through the spectrometer, since they are mapped onto corresponding pixels. This enables corrections for inhomogeneities of the electric and magnetic fields in the analyzing plane of the main spectrometer.

Aside from the silicon wafer, the detector system also houses a shielding and veto system to reduce background from cosmic rays. For further background reduction, a post-acceleration electrode can increase the energy of an electron coming from the main spectrometer by up to 12 keV to shift it towards a more favorable region for the detector. Additionally, different calibration sources, i.e. $^{241}$Am and $^{109}$Cd delivering $\gamma$s for a dead-layer-independent absolute energy calibration and a UV-LED providing photo electrons, are available.

The detector and data acquisition system is able to achieve a time resolution of 50 ns, which is important for time-of-flight measurements and hence for this thesis.

### 3.1.7. The Monitor Spectrometer

In addition to the sections shown in figure 3.1 on page 15 the refurbished spectrometer from the Mainz experiment is used to monitor the high voltage stability. It is placed in an extra building next to the spectrometer hall and is connected to the high voltage supply of the main spectrometer. By measuring conversion electrons from the $^{83m}$Kr decay, which have a well defined energy, it is possible to observe changes in the retarding potential. Any variation of the potential results in a shift of the measured line shape and line position.

## 3.2. Magnetic Adiabatic Collimation Combined with an Electrostatic Filter

All of the three spectrometers described above, as well as the one used in the Troitsk experiment, are based on the **M**agnetic **A**diabatic **C**ollimation combined with an **E**lectrostatic (MAC-E) filter technique. Spectrometers based on the MAC-E principle have a high energy resolution ($\Delta E/E = 1/20000$ in case of the KATRIN MS) and a large angular acceptance. Both features are very useful for KATRIN because of the required precision and the low statistics near the endpoint region of the $\beta$-decay.

Note that electrons produced in the tritium beta decay have a maximal kinetic energy of about 18.6 keV, which translates to a small Lorentz factor of

$$\gamma = \frac{1}{\sqrt{1 - \frac{v^2}{c^2}}} = 1.04\,, \tag{3.1}$$

which is neglected in the following calculations.

### 3.2.1. Working Principle and Energy Resolution

The MAC-E filter, as first described in [BPT80], is based on a simple electrostatic filter where electrons moving towards a potential $U$ are either transmitted when their kinetic energy is high enough, i.e.

$$E_{\text{kin}} > e \cdot U\,, \tag{3.2}$$

or reflected otherwise. Such a simple filter can only analyze the longitudinal part of the kinetic energy

$$E_{\parallel} = E - E_{\perp}\,. \tag{3.3}$$

In order to also analyze $E_{\perp}$, magnets are added at the entrance and exit of the spectrometer. In case of KATRIN the maximal magnetic field $B_{\text{max}} = 6\,\text{T}$ is reached at the pinch magnet at the exit and the field drops down to its minimal value of $B_{\text{min}} = 3 \cdot 10^{-4}\,\text{T}$ in the middle of the spectrometer in the so called analyzing plane, where the retarding potential has its maximal absolute value $|U_0|$.

Electrons entering the spectrometer are following a cyclotron trajectory around a magnetic field line and if the change of the magnetic field over one cyclotron period is small, i.e.

$$\left|\frac{1}{B}\frac{\partial B}{\partial t}\right| \ll \omega_{\text{cyc}} = \frac{qB}{m_{\text{e}}}\,, \tag{3.4}$$

the motion is adiabatic, meaning the magnetic moment

$$\mu = \frac{q}{2m_{\text{e}}}\left|\vec{L}\right| = \frac{E_{\perp}}{B} \tag{3.5}$$

of the electron is constant. Thus, an electron flying from a strong field $B_{\text{i}}$ at the entrance of the spectrometer towards the minimal magnetic field $B_{\text{ana}}$ in the analyzing plane, has most of its transversal kinetic energy transformed into longitudinal kinetic energy:

$$E_{\perp,\text{ana}} = E_{\perp,\text{i}} \cdot \frac{B_{\text{ana}}}{B_{\text{i}}}\,. \tag{3.6}$$

Assuming the retarding potential $U_0$ in the analyzing plane is known exactly, the energy resolution of a MAC-E filter is solely defined by the maximal amount of transversal kinetic energy a particle has in the analyzing plane, which can be calculated by using equation (3.6) on the facing page:

$$E_{\perp,\max} = E_{\text{start},\max} \cdot \frac{B_{\text{ana}}}{B_{\max}} = \Delta E\,. \tag{3.7}$$

For the nominal KATRIN configuration this yields an energy resolution of

$$\Delta E = 18.6\,\text{keV} \cdot \frac{3 \cdot 10^{-4}\,\text{T}}{6\,\text{T}} = 0.93\,\text{eV} \tag{3.8}$$

$$\frac{\Delta E}{E} = \frac{1}{20000}\,. \tag{3.9}$$

Such a good energy resolution is not obtainable with conventional semiconductor detectors and shows one of the benefits of MAC-E filters.

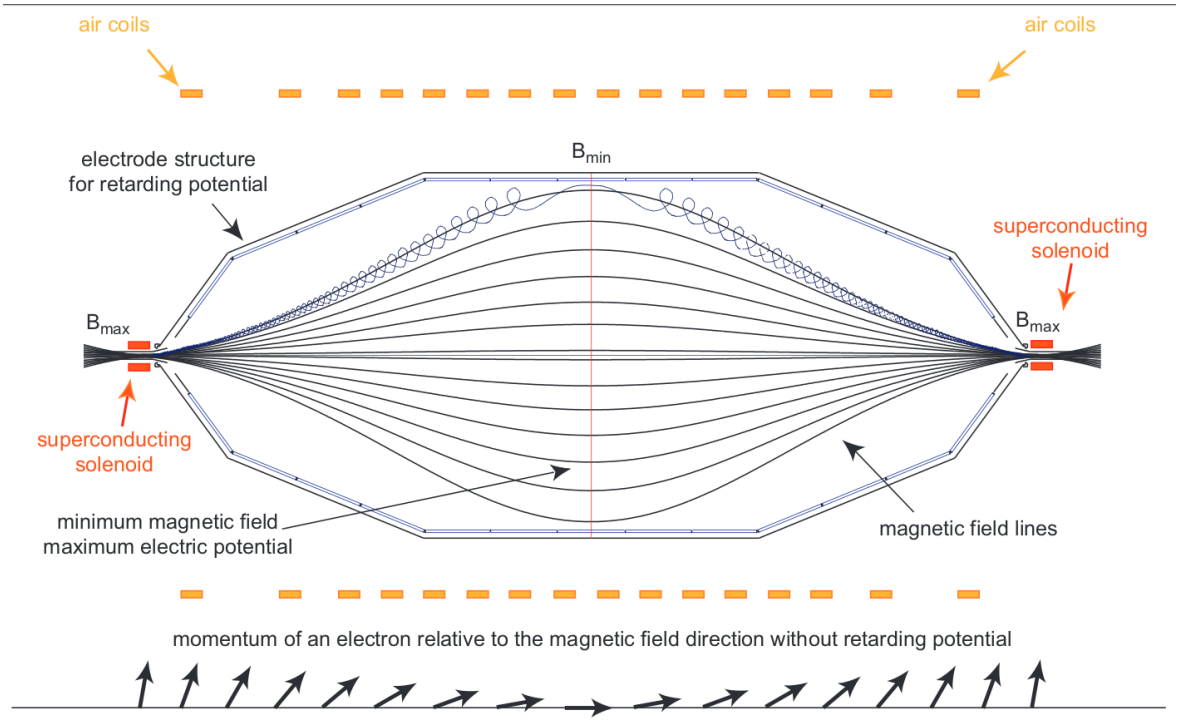


**Figure 3.5. – Schematic of the KATRIN main spectrometer as MAC-E filter:** Shown here is an electron performing a cyclotron motion (blue) around a magnetic field line (black) in the main spectrometer. The magnetic field is defined by two superconducting solenoids (red) and several air-coils (yellow), while the electric field is set by the vessel hull (black) and the inner electrode system (blue). The lower part shows how the electron momentum changes without any retarding voltage applied [Hug08].

### 3.2.2. Transmission Function of the KATRIN Main Spectrometer

The transmission condition for a simple electrostatic filter given in 3.2 becomes slightly more complex in the case of a MAC-E filter. Introducing the pitch angle $\theta$ as angle between the electron momentum and the magnetic field, the transversal and longitudinal parts of the kinetic energy can be written as

$$E_{\perp} = E_{\mathrm{kin}} \sin^2(\theta) \text{ and} \tag{3.10}$$

$$E_{\parallel} = E_{\mathrm{kin}} \cos^2(\theta)\,. \tag{3.11}$$

At the analyzing plane, the transmission condition now reads as

$$E_{\parallel,\mathrm{ana}} - qU_0 = E_{\mathrm{start}} \left(1 - \sin^2(\theta_{\mathrm{start}}) \frac{B_{\mathrm{ana}}}{B_{\mathrm{start}}}\right) - qU_0 > 0 \tag{3.12}$$

and can be rearranged to determine the transmitted region of $\theta_{\mathrm{start}}$:

$$\theta_{\mathrm{start}} \leq \arcsin\left(\sqrt{\frac{E_{\mathrm{start}} - qU_0}{E_{\mathrm{start}}} \frac{B_{\mathrm{start}}}{B_{\mathrm{ana}}}}\right). \tag{3.13}$$

This limits the theoretical angular acceptance of $2\pi$ of the MAC-E filter and the solid angle $\Delta\Omega$ accepted by the filter is connected to the maximal starting angle through

$$\frac{\Delta\Omega}{2\pi} = 1 - \cos(\theta_{\mathrm{start,max}})\,. \tag{3.14}$$

By using the relation $\cos(\arcsin(\sqrt{x})) = \sqrt{1-x}$, the transmission function can be written as

$$T(E_{\mathrm{start}},U_0) = \begin{cases} 0, & \text{for } E_{\mathrm{start}} < qU_0 \\ 1 - \sqrt{1 - \frac{E_{\mathrm{start}} - qU_0}{E_{\mathrm{start}}} \frac{B_{\mathrm{start}}}{B_{\mathrm{ana}}}}, & \text{for } qU_0 < E_{\mathrm{start}} \leq qU_0 + \Delta E \\ 1, & \text{for } qU_0 + \Delta E \leq E_{\mathrm{start}}\,, \end{cases} \tag{3.15}$$

where $\Delta E$ is the energy resolution derived in equation (3.7) on the previous page. From equation (3.15) it can directly be seen that the MAC-E filter works as an integrating high-pass filter.

In case of KATRIN, $B_{\mathrm{start}}$ is smaller than the magnetic field of the pinch magnet $B_{\mathrm{max}} = 6\,\mathrm{T}$ at the spectrometer exit, hence electrons can be reflected magnetically

when their starting angle is greater than

$$\theta_{\text{start,max}} = \arcsin\left(\sqrt{\frac{B_{\text{start}}}{B_{\text{pinch}}}}\right). \tag{3.16}$$

Modifying equation (3.15) on the preceding page to account for this change gives the KATRIN main spectrometer transmission function:

$$T(E_{start},U_0) = \begin{cases} 0, & \text{for } E_{\text{start}} < qU_0 \\ \frac{1-\sqrt{1-\frac{E_{\text{start}}-qU_0}{E_{\text{start}}}\frac{B_{\text{start}}}{B_{\text{ana}}}}}{1-\sqrt{1-\frac{B_{\text{start}}}{B_{\text{max}}}}}, & \text{for } qU_0 < E_{\text{start}} \leq qU_0 + \Delta E \\ 1, & \text{for } qU_0 + \Delta E \leq E_{\text{start}}\,, \end{cases} \tag{3.17}$$

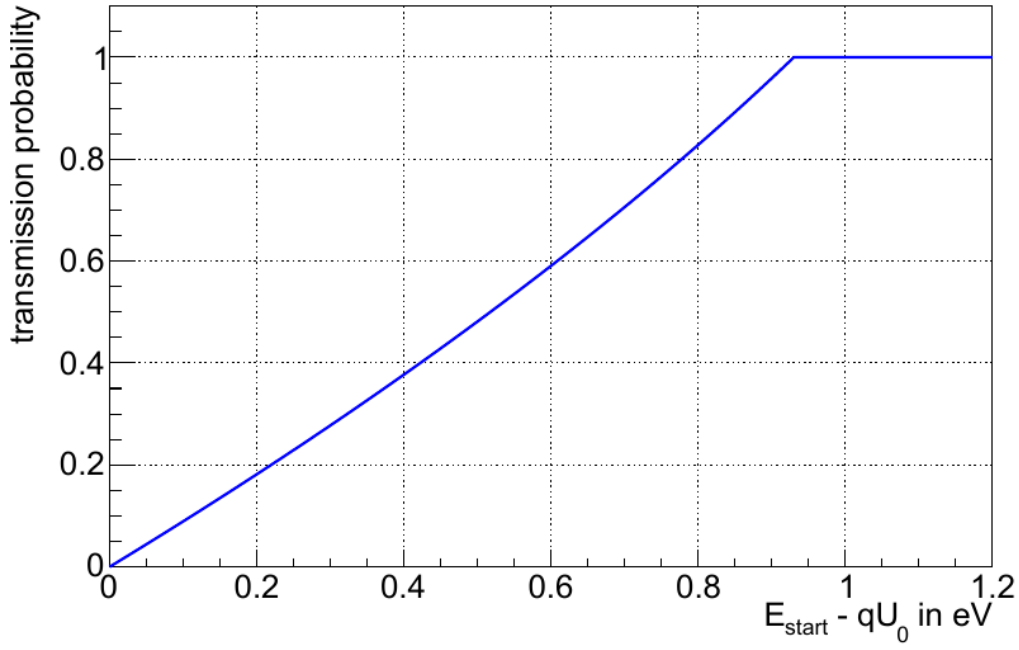


**Figure 3.6.** – **Transmission function of the KATRIN main spectrometer:** This is a plot of equation (3.17) for the KATRIN design values of $U_0 = 18.6\,\text{keV}$, $B_{\text{start}} = 3.6\,\text{T}$, $B_{\text{ana}} = 3 \cdot 10^{-4}\,\text{T}$, $B_{\text{max}} = 6\,\text{T}$ and an isotropic source. Electrons with a higher pitch angle $\theta$ also need a higher surplus energy $E_{\text{start}} - qU_0$ to get transmitted. Therefore the maximal transmission probability is reached at a surplus energy of $\Delta E = 0.93\,\text{eV}$ [Gro15].

# 4. Time-of-Flight

In addition to the standard KATRIN operation mode, which is planned to start in 2017, there have been ideas and proposals inside the collaboration for a slightly different approach to neutrino mass measurements with KATRIN, specifically **T**ime-**o**f-**F**light (ToF) methods.

## 4.1. Motivation

The general idea behind ToF methods is to eliminate the major drawback of only measuring an integrated spectrum with the standard MAC-E spectrometer setup. Recording an integrated spectrum only gives the total number of events above the current retarding voltage and for a complete neutrino mass analysis many different voltages have to be applied. ToF methods allow to retain the energy information of the transmitted electrons, effectively measuring a differential spectrum. Therefore the whole spectrum can be measured at once, so in principle it is sufficient to measure the tritium spectrum at a single retarding voltage, gaining in statistical sensitivity. For the standard mode it is currently planned to use about 40 different retarding voltages and a comparable result can be achieved with a small number of settings in ToF mode with larger statistical power, as shown in [Ste+13].

Because the flight time $\tau$ of an electron through the main spectrometer is a function of its energy and its pitch angle, measuring the time-of-flight gives information about the particle energy. This works better the less energy an electron has, because $\tau$ is inversely proportional to the square root of the longitudinal kinetic energy:

$$\tau \propto E_{\parallel}^{-\frac{1}{2}} \,. \tag{4.1}$$

For this reason, the KATRIN main spectrometer is perfectly suitable for time-of-flight spectroscopy, since electrons are slowed down to low velocities near the analyzing plane and the spectrometer is long enough for the different energies to result in distinguishable

flight times. In theory, it is even possible to resolve energy differences beyond the energy resolution of $\Delta E = 0.93\,\mathrm{eV}$, if the time resolution is sufficient [Ste+13].

In order to be able to perform flight time spectroscopy and benefit from the additional information about the electrons, it is necessary to get a start and a stop signal. The stop signal is conveniently provided by the detector system with a decent time resolution of 50 ns. However, a start signal is much harder to obtain without influencing the electrons too much and different ways will be discussed in the following two subsections.

## 4.2. Time-of-Flight Methods

To obtain an ideal time-of-flight spectrum, the start time has to be known precisely, which requires a detection of the electron prior to the spectrometer without excessive change to its energy. While the physical limits, e.g. set by Heisenberg's uncertainty principle, are of no concern, a technical realization of a single electron tagger suitable for KATRIN has yet to be developed.

Overall there are four different principles by which an electron can be tagged:

1. radiation emitted by an accelerated electron,
2. work done by image charges moving through a load circuit,
3. work done by magnetically induced currents flowing through a load circuit and
4. electrons interacting with other electrons, e.g. in atoms.

Each method is discussed in [Ste+13] and the cyclotron radiation detection seems to be the best option. Nevertheless, the needed long solenoids would not fit into the available space at KATRIN and other methods are not yet sensitive enough. Besides the ability to perform time-of-flight spectroscopy, an electron tagger could also be used for background discrimination through coincidence triggers, rejecting electrons created in the spectrometer.

Another way to obtain a start time is using a gated filter that periodically blocks electrons from entering the main spectrometer. In KATRIN this can be realized by a high-frequency voltage modulation of the pre-spectrometer or the source. The voltage has to be modulated between a setting where every electron in the endpoint region is transmitted and another setting, where every electron is blocked. Such a method

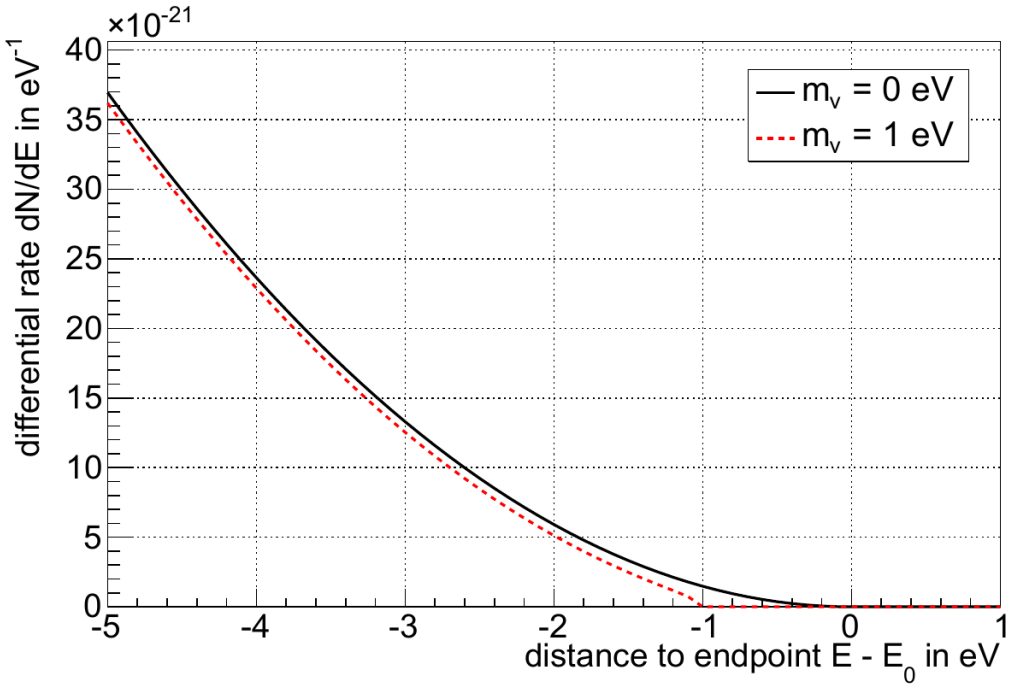


(a) Differential tritium spectrum

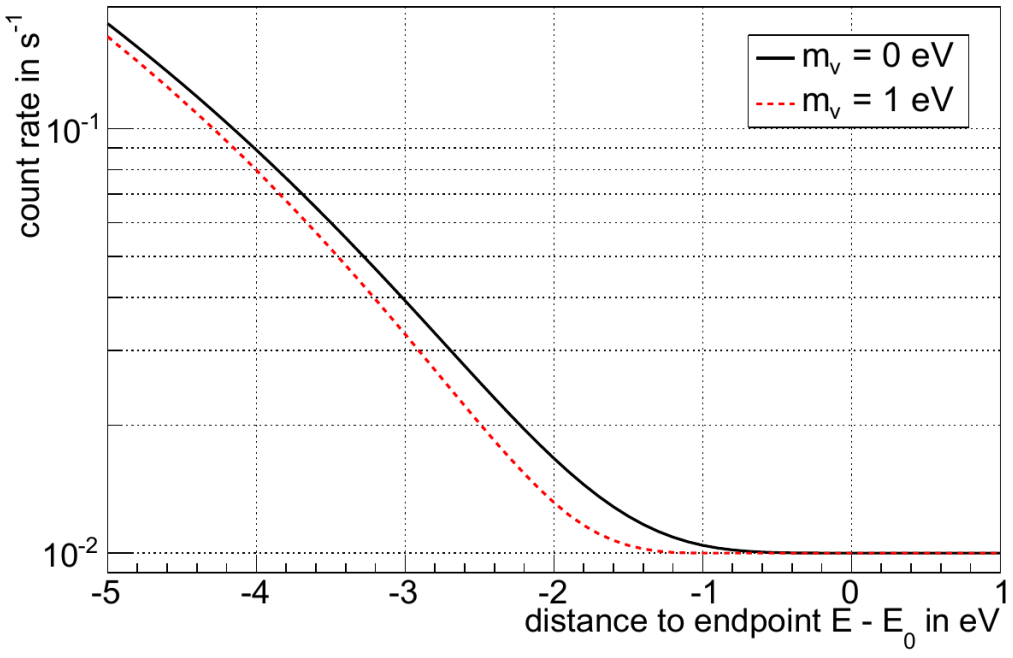


(b) Integrated tritium spectrum

**Figure 4.1. – Comparison between differential (a) and integrated (b) tritium spectrum:** The black line shows the spectrum for a neutrino mass of 0 eV, while the red line represents a neutrino mass of 1 eV. In the lower plot, the remaining count rate above the endpoint of 10 mHz represents the assumed background [Gro15]. Measuring the integrated spectrum for a fixed retarding potential yields only a single point of the spectrum, while in the differential case the whole spectrum above the retarding potential is measured at once.

has already been discussed and applied in [Bon+99] for a modulated source at the Mainz experiment, where the ToF information has been used as a low-pass filter to reject particles with high energies. Yet, with the pre-spectrometer being available in KATRIN it is more convenient to utilize it as gated filter because, in contrast to a modulated source, the exact value of the applied voltage does not have to be known.

The gated filter approach can be described by the period $t_\mathrm{p}$ of the modulating frequency and the time interval $t_\mathrm{o}$ in which electrons can pass. On the one hand a small $t_\mathrm{o}$ is desirable, because the start time can only be determined down to the time interval where electrons can pass and a smaller $t_\mathrm{o}$ lowers the start time uncertainty. On the other hand a small $t_\mathrm{o}$ reduces the number of electrons reaching the detector and hence decreases statistics. The period $t_\mathrm{p}$ and the open time $t_\mathrm{o}$ together define the duty cycle:

$$\eta = \frac{t_\mathrm{o}}{t_\mathrm{p}} \,. \tag{4.2}$$

Though the duty cycle increases by shortening $t_\mathrm{p}$ for a fixed $t_\mathrm{o}$, once $t_p$ is on the same order of the time-of-flight it also leads to more electrons from the previous periods arriving in the current one and hence increases background.

The gated filter approach is described in detail in [Ste+13] and a sensitivity analysis for an optimized duty cycle performed there yields a result of $\sigma_{\mathrm{stat,tof}}(m^2(\nu_\mathrm{e})) = 0.021\,\mathrm{eV}^2$, compared to the value of $\sigma_{\mathrm{stat,standard}}(m^2(\nu_\mathrm{e})) = 0.020\,\mathrm{eV}^2$ for the standard KATRIN method. This shows that time-of-flight methods bear a potential to improve the neutrino mass limits, since further optimizations of this approach may still be possible. Furthermore, the gated filter is an interesting method for the search for keV sterile neutrinos with KATRIN. Of course, the whole concept of using the pre-spectrometer as gated filter requires that the Penning trap between the two spectrometers can be controlled.

## 4.3. Time-Focusing-Time-of-Flight Methods

A further procedure to obtain a start time is based on the **T**ime-**F**ocusing-**T**ime-**o**f-**F**light (TFToF) method. The basic idea is similar to the gated filter method, namely applying a time-varying potential to one of the spectrometers. Instead of periodically blocking the electron flux though, electrons are accelerated depending on the time at which they enter the spectrometer. Electrons arriving later are accelerated more and thus can catch up with earlier ones. If done right, particles of the same energy and pitch angle arrive at the same time at the detector. This is comparable to the process of

bunching at a particle accelerator and the principle is illustrated in a simplified version in figure 4.2.

Assuming that electrons with an initial energy $E_0$ are only affected by the accelerating voltage $U_{\mathrm{acc}}$ at their start time $t_0$, the distance they have traveled at time $t > t_0$ can be expressed as:

$$s(t) = \sqrt{\frac{2(E_0 + qU_{\mathrm{acc}}(t_0))}{m_{\mathrm{e}}}} \cdot (t - t_0)\,. \tag{4.3}$$

Ideally all electrons with the same initial energy are focused onto a common arrival time, requiring a monotonically rising accelerating voltage. From equation (4.3) it follows, that the accelerating voltage has to be of the form

$$U_{\mathrm{acc}}(t_0) = \frac{\frac{s^2 m_{\mathrm{e}}}{2(t-t_0)^2} - E_0}{q} \tag{4.4}$$

for electrons with a certain energy $E_0$ to arrive at position $s$ at the time $t$. For the technical realization it is easier to use a sinusoidal waveform, hence a sine function is used in the simulations in section 5.

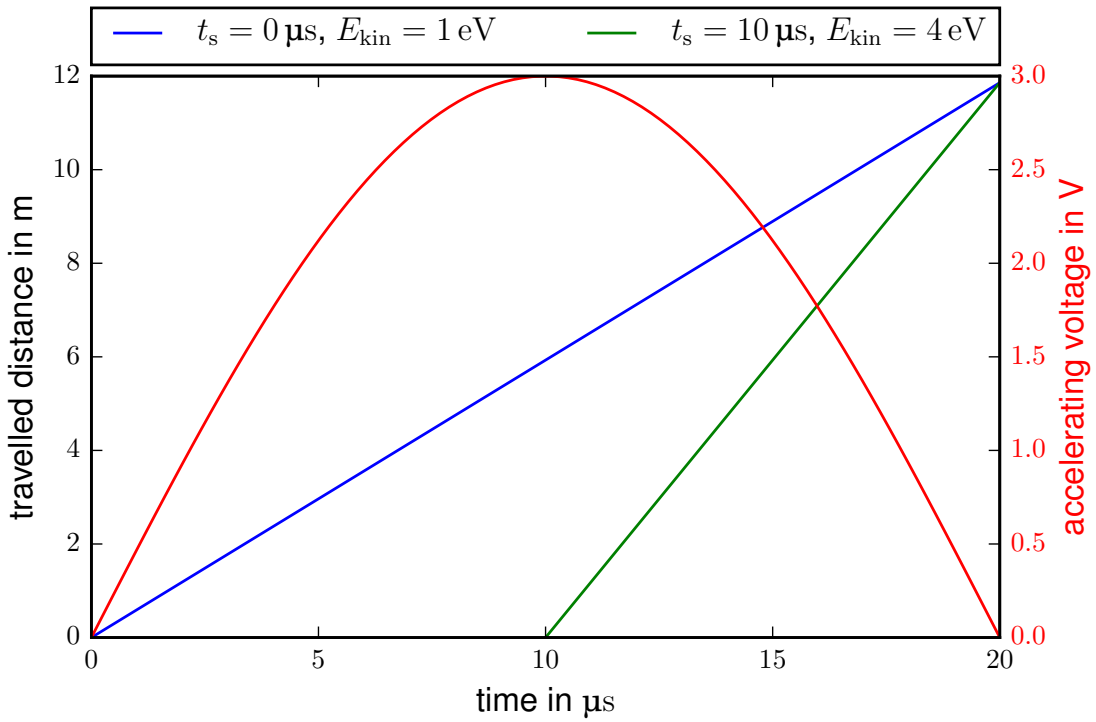


**Figure 4.2.** – **Time-focusing principle:** The blue line represents the distance traveled by an electron with a constant kinetic energy of $E_0 = 1\,\mathrm{eV}$. After $\Delta t_0 = 10\,\mu\mathrm{s}$ a second electron with $E_0 = 1\,\mathrm{eV}$ is started (green), but its energy is increased to $4\,\mathrm{eV}$ by the accelerating voltage (red, right scale). In this plot the electron energies are not affected by the accelerating voltage after the start time, resulting in a constant movement. At $t = 20\,\mu\mathrm{s}$ both electrons have traveled the same distance of $s \approx 11.86\,\mathrm{m}$. If a detector is placed at this position, the time-of-arrival is the same for both electrons.

For the time-focusing to work a long enough delay line, where electrons have low energies, has to be present for the different velocities to take effect. While the main spectrometer seems like a good option to act as accelerator and delay line, it can not simply be used in its standard setting. Since for the needed time-dependent acceleration the retarding potential also varies with time, the energy resolution of the main spectrometer would be limited to the peak-to-peak voltage of the modulating waveform. For values of $\Delta U_{\mathrm{pp}} \geq 25\,\mathrm{V}$, which are required for sufficient time-focusing of electrons with higher surplus energies, this trade-off is not acceptable. It is also necessary to use the delay line after the energy analyzer, because accelerating electrons before the analyzing plane lets particles pass the filter which otherwise would get reflected.

When using the TFToF method, the absolute flight time cannot be obtained, but only the time-of-arrival modulo the period $T$ of the accelerating voltage waveform. This results from taking a distinct point of the waveform as reference start time for all electrons during one period.

In this thesis two separate methods to use TFToF in KATRIN are investigated and laid out in the following subsections.

### 4.3.1. Split Main Spectrometer

The first method discussed here can be realized with only very little extensions of the experimental setup and non-standard voltage settings of the main spectrometer. This approach aims to use the main spectrometer as analyzer and delay line at once by shifting the analyzing plane towards the upstream side of the tank, while the downstream part of the electrode system is supplied by a time-dependent potential to accelerate electrons according to their start time. This setup is illustrated in figure 4.3 on the facing page. Compared to the standard setup, the only additions needed are a function generator and an amplifier connected to the electrode system of the downstream conic part of the spectrometer.

At the end of the SDS-Measurements Phase 2 in 2015, it was tested if the idea of the split main spectrometer could work and some measurements with an angular selective electron source (e-gun) were made [ELOG115]. Although the e-gun itself is highly complex, it is only used as a tool providing electrons with a defined energy, pitch angle, position and starting time here. Further information about the e-gun can be found in [Zac14] and [Win14]. The obtained data is evaluated and compared to simulations in section 5.2, while the experimental setup is described here.

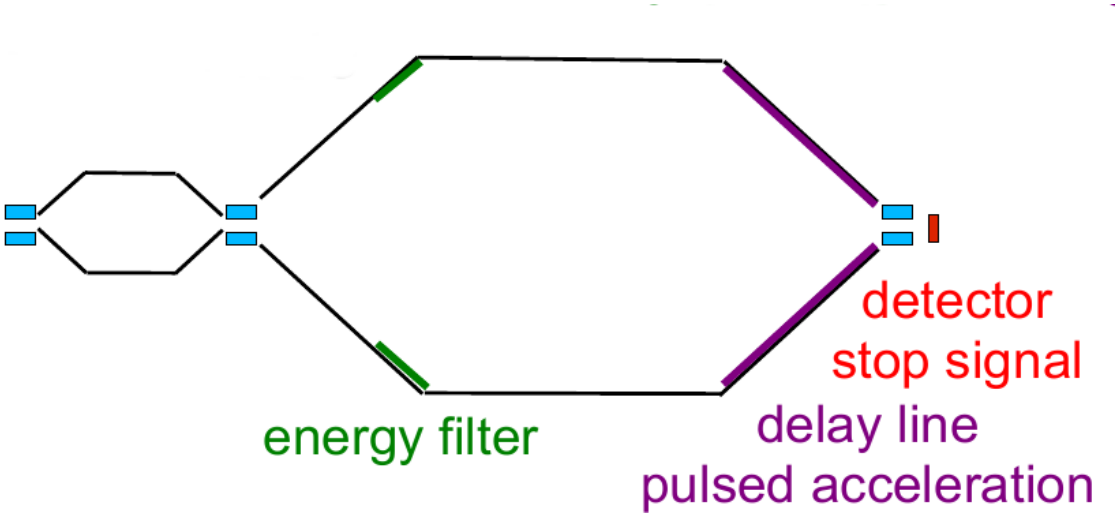


**Figure 4.3.** – **Principle of the split main spectrometer:** This graphic shows that the energy filtering is shifted towards the source side of the spectrometer (green) and the downstream part is used as acceleration and delay line (violet) [Wei16].

In addition to the standard main spectrometer setting an Agilent 33220A pulser provides a square waveform with a frequency of 1 kHz. It is connected to a Kepco BOP 1000M amplifier with an amplification factor of 100, providing the acceleration voltage for the time-focusing. An additional Tektronix AFG3102 pulser is used to trigger the e-gun and is connected to the sync output of the Agilent pulser. The e-gun pulser is set to a frequency of 24 kHz resulting in 24 short electron bursts during a waveform. For an even finer scanning, the measurements are repeated for different phase shifts $\Delta\phi$, altering the start time of the electron bursts compared to the waveform generated by the Agilent pulser. With ten shift values, from $\Delta\phi = 0°$ to $\Delta\phi = 13.5°$ in 1.5° steps, and 24 electron bursts each, 240 different start-times are utilized overall. Hence, the potential modulating waveform is scanned in 1.5° steps.

A schematic of the circuit layout is shown in figure 4.4 on the next page and the voltage settings noted in [ELOG115] can be found in table 4.1. The resulting electric potential is visualized in figure 4.5. Additionally, the optimized air-coil settings for the shifted analyzing plane setting found in table 4.2 are applied.

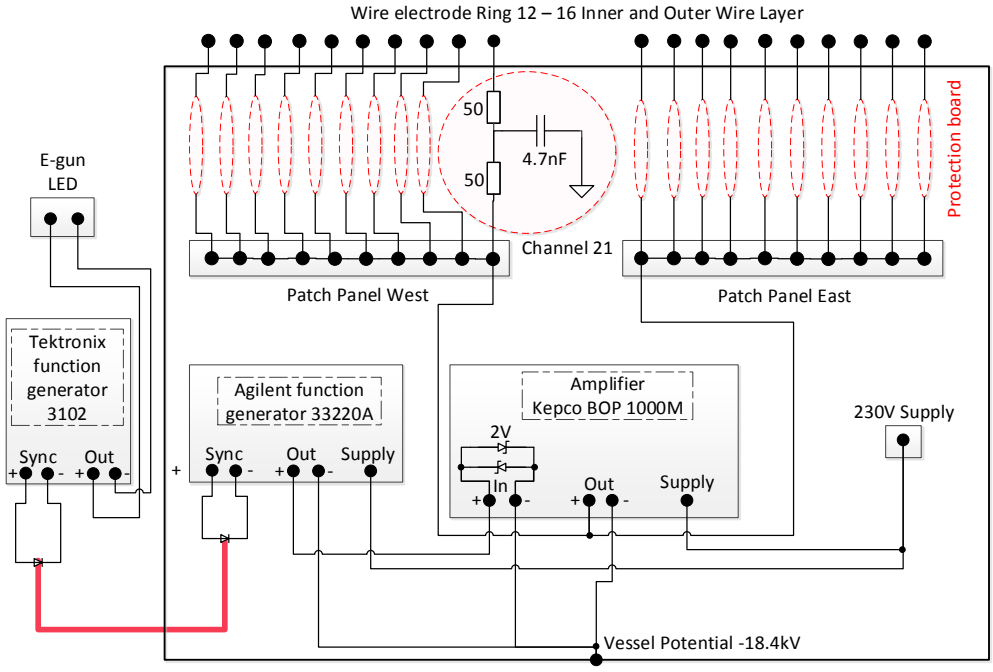


**Figure 4.4.** – **Circuit layout for the split spectrometer setup:** Shown here is the setup of the two pulsers and the connected amplifier. The output channel of the amplifier is connected to the two patch panels, supplying the acceleration voltage for rings 12-16, while the offsets for the remaining rings are constant[Res15].

**Table 4.1.** – **Voltage settings for the split main spectrometer compared to SDS 2 standard settings:** For ring 2-11 the resulting voltage is made up of the vessel, the IE common and the individual offset voltage. Ring 12-16 are connected to the Kepco amplifier and here the resulting voltage only consists of the vessel voltage and the offset.

| part | voltage | resulting voltage in V | standard voltage in V |
|---|---|---|---|
| vessel $U_{\mathrm{V}}$ | $-18500\,\mathrm{V}$ | $-18500$ | $-18400$ |
| IE common $U_{\mathrm{IE}}$ | $U_{\mathrm{V}} - 150\,\mathrm{V}$ | $-18650$ | $-18600$ |
| ring 2 | $U_{\mathrm{IE}} + 60\,\mathrm{V}$ | $-18590$ | $-18400$ |
| ring 3 | $U_{\mathrm{IE}} + 50\,\mathrm{V}$ | $-18600$ | $-18400$ |
| ring 4 | $U_{\mathrm{IE}} + 50\,\mathrm{V}$ | $-18600$ | $-18600$ |
| ring 5-6 | $U_{\mathrm{IE}} + 30\,\mathrm{V}$ | $-18620$ | $-18600$ |
| ring 7-11 | $U_{\mathrm{IE}} + 50\,\mathrm{V}$ | $-18600$ | $-18600$ |
| ring 12-14 | $U_{\mathrm{V}} - 50\,\mathrm{V}$ to $-100\,\mathrm{V}$ | $-18550$ to $-18600$ | $-18600$ |
| ring 15-16 | $U_{\mathrm{V}} - 50\,\mathrm{V}$ to $-100\,\mathrm{V}$ | $-18550$ to $-18600$ | $-18400$ |

**Table 4.2.** – **Air-coil settings for the split main spectrometer:** Shifted analyzing plane air-coil currents compared to the SDS 2 standard settings for a minimal magnetic field of 3.8 G.

| air-coil | TFToF mode current in A | SDS 2 3.8 G standard current in A |
|---|---|---|
| 1 | 9.0 | 21.14 |
| 2 | 51.7 | 25.66 |
| 3 | 33.4 | 20.30 |
| 4 | 40.6 | 28.36 |
| 5 | 75.6 | 38.82 |
| 6 | 93.3 | 27.52 |
| 7 | 73.7 | 34.37 |
| 8 | 92.9 | 50.68 |
| 9 | 66.2 | 10.37 |
| 10 | 0.8 | 44.44 |
| 11 | 31.2 | 37.19 |
| 12 | 40.1 | 20.96 |
| 13 | 88.3 | 43.32 |
| 14 | -17.2 | 50.35 |

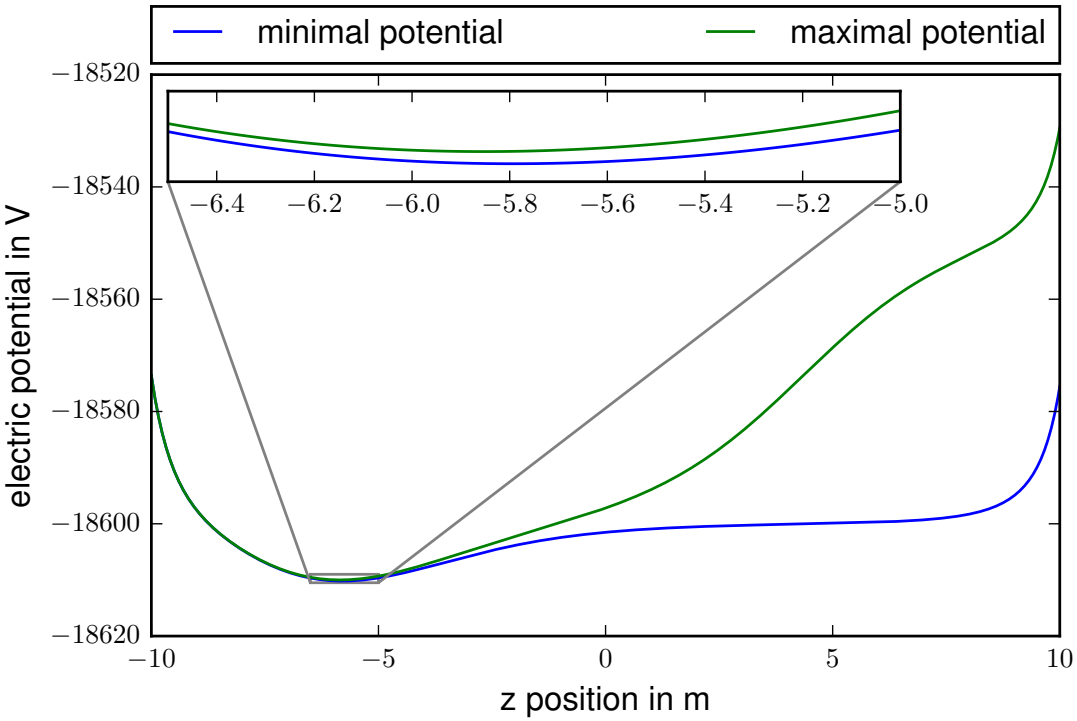


**Figure 4.5.** – **Electric potential inside the split main spectrometer:** The blue line shows the potential where the accelerating voltage is at its minimal value, while the green curve represents the maximal accelerating voltage. The variation of the retarding potential in the analyzing plane shown in the inset is about 0.2 V. The center of the main spectrometer is chosen to be at $z = 0$ m.

A drawback of this option is the decreased energy resolution of $\Delta E = 2\,\mathrm{eV}$ of the main spectrometer, due to the higher magnetic field of about $B_{\mathrm{min}} = 6.5 \cdot 10^{-4}\,\mathrm{T}$ in the analyzing plane, not taking into account deviations of the retarding potential in the analyzing plane due to the changing potential in the downstream part. The advantage lies in the very small effort needed to realize this setup experimentally.

### 4.3.2. Third Spectrometer

In this thesis it is also investigated how much TFToF spectroscopy would benefit from an additional spectrometer as a dedicated delay and acceleration line. The new TFToF section is inserted into the beamline between the main spectrometer and the detector section. This approach allows the main spectrometer to work in its nominal setting, thus keeping the standard energy resolution while gaining additional information through TFToF analysis. This addition may pose an option to go beyond the KATRIN sensitivity of 200 meV with less effort than designing and constructing a new experiment from scratch.

For the reason of simplicity, the third spectrometer is assumed equal to the main spectrometer here. While a smaller and therefore cheaper tank could prove to be sufficient for an increased sensitivity, a study for an optimized design of the third spectrometer goes beyond the scope of this thesis. It may also be possible to construct a light-weight version of the main spectrometer for a fraction of the cost, so that assuming a main-spectrometer-like TFToF section is not completely unrealistic. Technical challenges, like the additional Penning Trap between the spectrometers or funding and scheduling, will also not be addressed here.

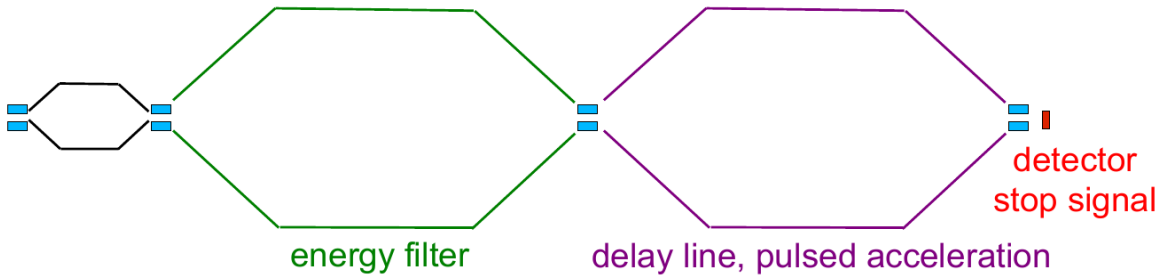


**Figure 4.6.** – **Principle of the third spectrometer:** Here, the main spectrometer remains responsible for energy filtering (green) and the subsequent new spectrometer is used as acceleration and delay line (violet) [Wei16].

# 5. Time-Focusing-Time-of-Flight Simulations with Kassiopeia

This thesis mainly deals with simulations of the methods described in section 4.3 and therefore a short introduction to the utilized software will be given, before the TFToF simulations are discussed.

## 5.1. Kassiopeia and Additions for Time-Dependent Potentials and Fields

A sophisticated particle tracking software named *Kassiopeia* has been developed inside the KATRIN collaboration and is now fully integrated into the *Kasper* framework together with many tools for KATRIN related simulations. A user generated input file, defining the geometry, is used by the electromagnetic field solver *KEMField*, which is also part of the Kasper framework. The resulting fields, together with the geometry, are then used in Kassiopeia to simulate tracks of charged particles by discretizing the flight paths into steps and solving the equations of motion for each individual step. After a finished simulation the result can be visualized with *ROOT*[1] (2D) or *VTK* (3D). More detailed descriptions of Kassiopeia can be found in [Gro15] and [Beh16].

Regardless of how well-engineered Kassiopeia was up to this thesis, it was not able to use dynamic electromagnetic fields to calculate particle tracks. For this reason Kassiopeia has been extended by the *KSFieldElectricRamped2Fields*[2] class to be able to handle time-varying electric potentials used in time-focusing-time-of-flight methods. It is based on the already existing *KSFieldElectricRamped* class used to modulate an electric field and potential by different periodic functions. In contrast to the existing code, the new KSFieldElectricRamped2Fields class is able to take two different electric

[1] ROOT is an object oriented framework for large scale data analysis. For further information see [ROOT].

[2] For the source code see section A.1.

potentials and fields as input and ramp between them with several functions, as shown in figure 5.1 for a sine and two input potentials.

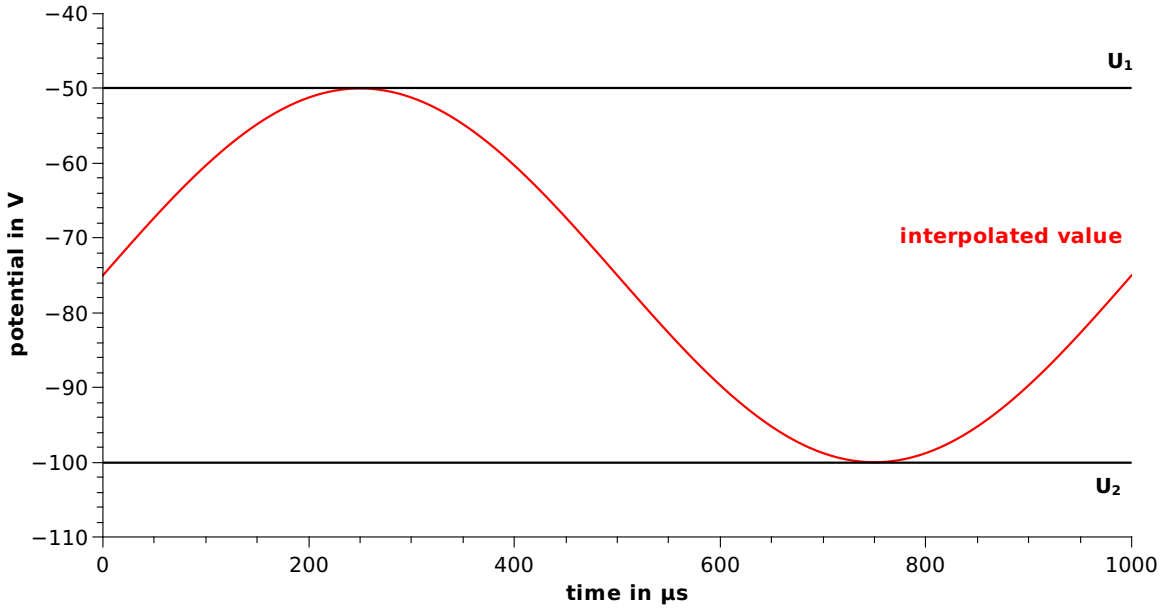


**Figure 5.1.** – **Principle of KSFieldElectricRamped2Fields:** The resulting time-dependent potential (red) is obtained through interpolation between two different pre-calculated potentials $U_1$ and $U_2$ (black). The used function is $U_2 \cdot (-0.5 + 0.5 \sin\left(\frac{2\pi}{1000\,\mu s} \cdot t\right)) - U_1 * (0.5 + 0.5 \sin\left(\frac{2\pi}{1000\,\mu s} \cdot t\right))$

In order to use the new class it is first necessary to pre-calculate the electric potentials. Two Kassiopeia configuration files are used, one with the lower voltage settings and one with the upper voltage settings. The geometry defined in these input files has to be the same as in the case of the desired time-dependent simulation. KEMField calculates the charge densities for each electrode of the static geometry as well as the magnetic fields of the setup and the results can be saved to hard disk. This enables Kassiopeia to reuse the calculated charge densities in case of starting a simulation with the same settings by calculating a hash for the geometry and applied voltages. These hashes are stored together with the calculated solutions and can be read out with Kasper's *InspectEMFile* program. Since there exists the possibility to explicitly tell Kassiopeia which hash it should use, two different electrostatic fields can be set up inside a configuration file. Additionally the ramped electric field is set up and given the two other fields as input. An example XML configuration file for the test setup shown in figure 5.2 on the next page can be found in section A.2.

To test the new class, two simple methods are used. First it is shown qualitatively that a time-depending field is achieved. Two ring electrodes on opposite potentials

are therefor ramped between $-1\,\mathrm{V}$ and $+1\,\mathrm{V}$. Electrons started in the middle with a negligible energy of $10^{-10}\,\mathrm{eV}$ are accelerated towards the positive electrode. Since the potential is modulated with a sine, it becomes negative after half a period $T/2 = 5\,\mu\mathrm{s}$ and the electron is repelled. This process is repeated and the particle oscillates between the two electrodes as shown in figure 5.2. In the following, the more negative potential will be called $U_2$ or lower potential and the less negative potential will be called $U_1$ or higher potential.

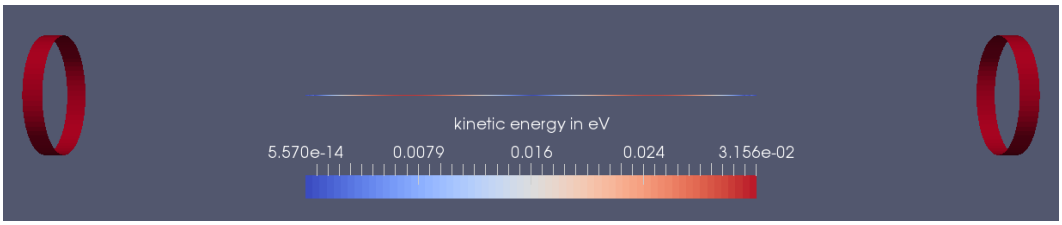


**Figure 5.2.** – **Oscillation between two ring electrodes (red):** The resulting trajectory (color coded with the electron's kinetic energy) is a qualitative proof of KSFieldElectricRamped2Fields' functionality.

Although a detailed analysis of the data collected from this simulation can give quantitative information about the ramping, it is easier to read out the field value with the *TestRampedField* tool provided by Kassiopeia.

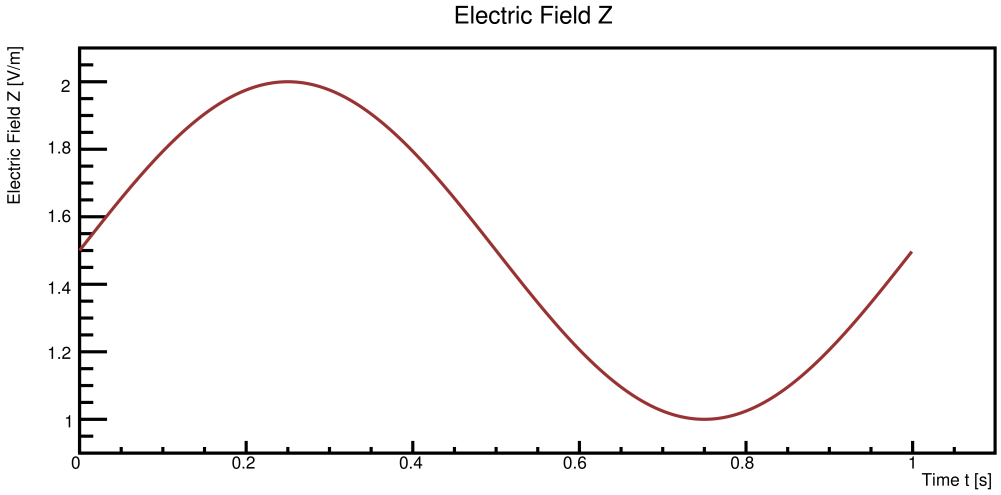


**Figure 5.3.** – **Quantitative test of field ramping:** Shown here is the output of Kassiopeia's TestRampedField program, modified to use KSFieldElectricRamped2Fields. Two different constant electric fields are provided as input and the resulting curve looks like the expected one illustrated in figure 5.1 on the facing page.

These tests show that the KSFieldElectricRamped2Fields class works as intended and thus can be used for simulations with time-dependent electric fields and potentials.

## 5.2. Split Main Spectrometer

In this section two main strategies are pursued. First, a simulation is used to recreate some results from the SDS Phase 2 measurements in order to validate that the simulations are reliable and do not neglect any relevant effects. Second, investigations on an optimized parameter set for neutrino mass measurements are carried out.

### 5.2.1. Simulating the SDS 2 Measurements

To be able to compare results from the simulation to the measured data[3], the axially symmetric geometry files from the SDS 2 setup are used and the electrode voltages and air-coil currents are set as in table 4.1 on page 34 and table 4.2 on page 35. In the simulation, electrons are started inside the magnet at the exit of pre-spectrometer (PS2 magnet), since a full simulation of the e-gun would slow down the simulations too much. The flight time from the backplate of the e-gun to the PS2 magnet is small, nearly equal for each electron due to the high kinetic energy they have in this section and thus can be neglected. Furthermore, electrons are started on the symmetry axis at $r = 0\,\mathrm{m}$ with small polar angles $\theta \leq 10^\circ$ and a small energy spread of $\pm 0.1\,\mathrm{eV}$, to replicate the real conditions specified by the e-gun as close as possible. In the experiment the e-gun pulser's frequency of 24 kHz leads to an electron burst every 41.7 µs, which can be simulated by using different start times in the configuration file and simulating 1000 electrons per start time. Using ten different phases with steps of 1.5° like in the setup described in section 4.3.1 results in a total number of 240000 simulated electrons for each of the 13 surplus energies ranging from 0 eV to 5 eV in 0.5 eV steps and also containing two additional values of ±0.1 eV. Because of the large amount of gathered data not every surplus energy will be discussed in detail, but certain values are chosen to be used as example.

Special care has to be taken in regard to the employed modulating function. While the Agilent 33220A pulser provides a square waveform, the utilized Kepco BOP 1000M amplifier has a $-3\,\mathrm{dB}$ high frequency cutoff at $f = 1.8\,\mathrm{kHz}$ [11] while an ideal square waveform has frequency components of up to infinity, which cannot be processed by the slow amplifier. Therefore, the output waveform is closer to a sinusoidal and has been measured at the amplifier output. The resulting signal is shown in figure 5.4 on the next page.

[3] The corresponding SDS 2 measurement run numbers are 23278 to 23287 and an overview over the measurements is given in [ELOG115].

Since in the experiment the voltage cannot be measured directly at the inner electrode system, there is another uncertainty about the real value and for the simulations a sine function with a frequency of 1 kHz is assumed, because the amplifier already delivers a sine-like waveform and further smearing is expected.

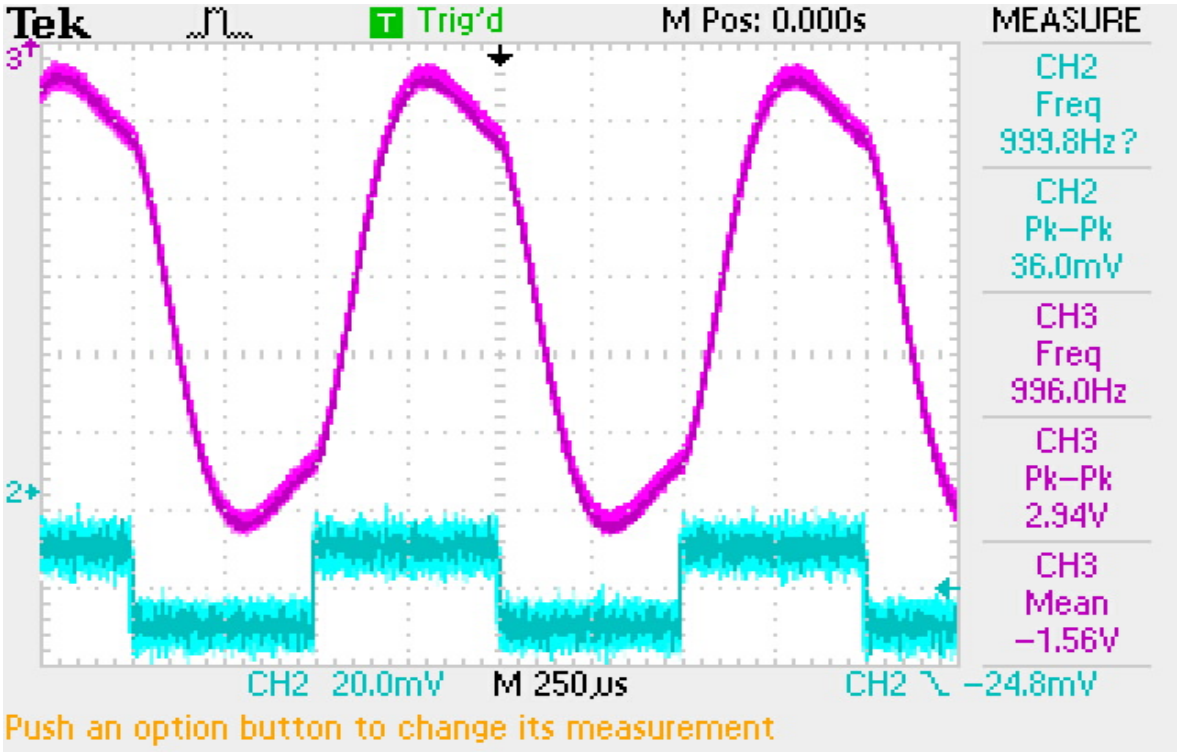


**Figure 5.4.** – **Waveform change due to the amplifier:** It is apparent that the output signal (magenta) does not strictly follow the input signal (cyan). The square waveform is smeared out and becomes similar to a sinusoidal.

In the following, the term *surplus energy* refers to the difference between the kinetic energy of an electron with a pitch angle of $\theta = 0°$ and the mean retarding potential in the analyzing plane

$$E_{\mathrm{surp,simulation}} = E_{\mathrm{kin,start}} - q \underbrace{\frac{U_{\mathrm{ana},1} + U_{\mathrm{ana},2}}{2}}_{U_{\mathrm{ana,mean}}} , \tag{5.1}$$

not taking into account the small energy spread of ±0.1 eV. This means that even electrons with small negative surplus energies $E_{\mathrm{surp}} < 0$ can be transmitted during the time where a positive accelerating voltage is applied to the downstream part of the spectrometer, because $U_{\mathrm{ana}}$ is modified by about ±0.103 V at the waveform's extrema. This further reduces the already decreased energy resolution because of the higher magnetic field. Here, the term *positive accelerating voltage* refers to a potential setting more positive than the mean, i.e. $U - \frac{U_1+U_2}{2} > 0$, although every point between $U_2$

and $U_1$ is an accelerating voltage compared to the standard setting where only $U_2$ is used.

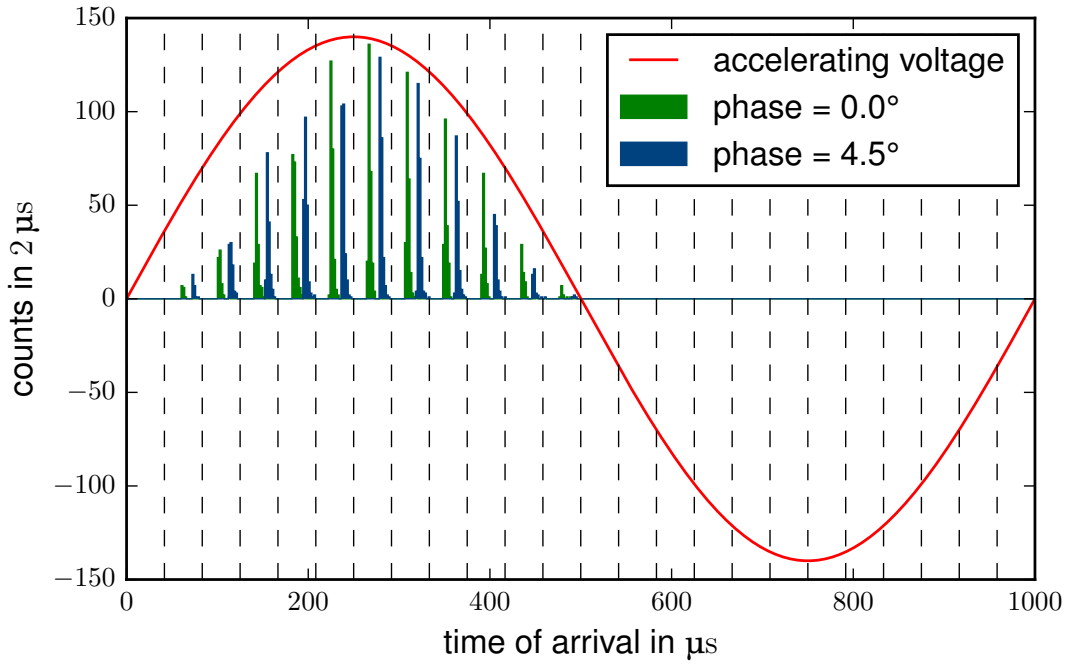


**Figure 5.5. – Split MS simulation for −0.1 eV surplus energy:** Shown here are the numbers of electrons reaching the detector for two different phases (green and blue). The vertical dashed lines represent the start times for electrons with a phase shift of 0° and the red curve illustrates the accelerating voltage in arbitrary units. The used bin width is 2.0 µs.

From figure 5.5 it can be seen that the simulations show the expected behavior. For higher values of the accelerating voltage, more electrons reach the detector and for lower potential settings than the mean no electrons are transmitted.

For higher surplus energies, the peaks are expected to get sharper and higher, since the velocity differences become smaller and more electrons are transmitted. Also the peaks should be closer to the start times, since more kinetic energy leads to shorter flight times. All of these predictions are matched by simulation results as shown in figure 5.6 on the next page.

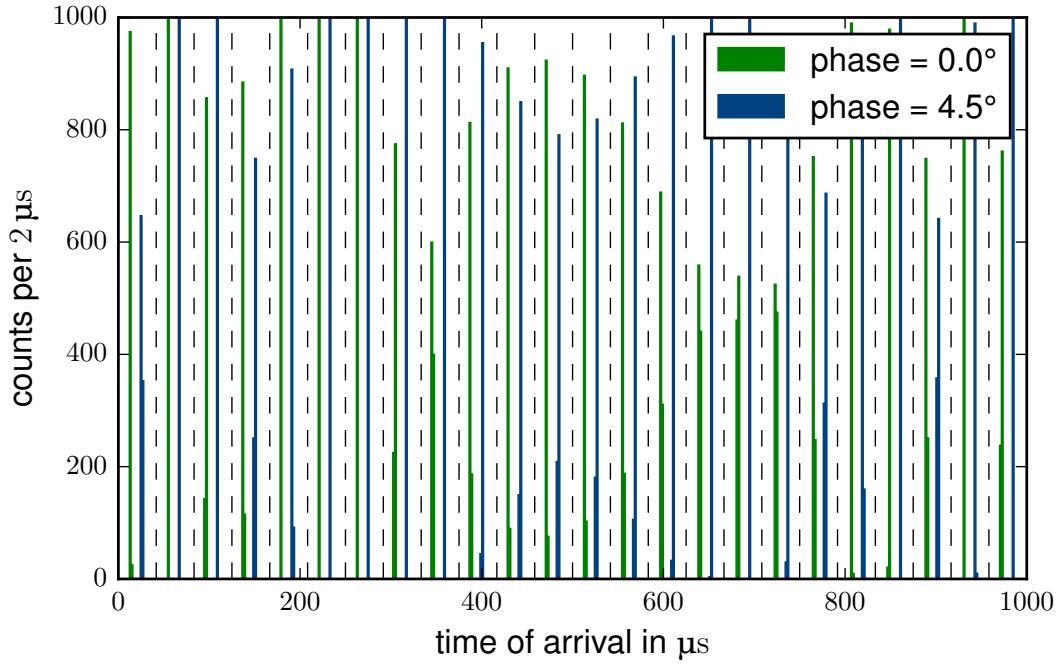


**Figure 5.6.** – **Split MS simulation for 0.5 eV surplus energy:** Here, the number of electrons reaching the detector is not time-dependent anymore. The peak area stays constant and the different heights are due to binning effects. The vertical dashed lines represent the start times for electrons with a phase shift of 0° and the used bin width is 2.0 µs.

Here the peak area is constant, regardless of the start time. The required surplus energy for electrons with the maximal used starting angle of $\theta_{\max} = 10°$ to be transmitted during all times can be calculated by rearranging equation (3.12) on page 24 and using the retarding voltage value for the lower potential:

$$E_{\text{surplus}} \geq \frac{\overbrace{18610.19\,\text{eV}}^{qU_2}}{1 - \sin^2(10°) \cdot \frac{6.5 \cdot 10^{-4}\,\text{T}}{4.5\,\text{T}}} - \underbrace{18610.09\,\text{eV}}_{qU_{\text{ana,mean}}} \approx 0.18\,\text{eV}\,. \tag{5.2}$$

For a transmission probability of 1, another 0.1 eV has to be added to the result from equation (5.2), since the electrons are started with an energy spread. Figure 5.6 confirms the calculation result.

For a surplus energy of 0.0 eV the time-dependence of the number of transmitted electrons can, in the first order, be described by a sine, as illustrated in figure 5.7 on the next page. While these plots show statistical effects, they are not suitable to read off changes in flight time, because of the large arrival time interval covered. However, with the start and stop time for each electron provided by Kassiopeia it is possible to create real time-of-flight plots like shown in figure 5.8 on page 45.

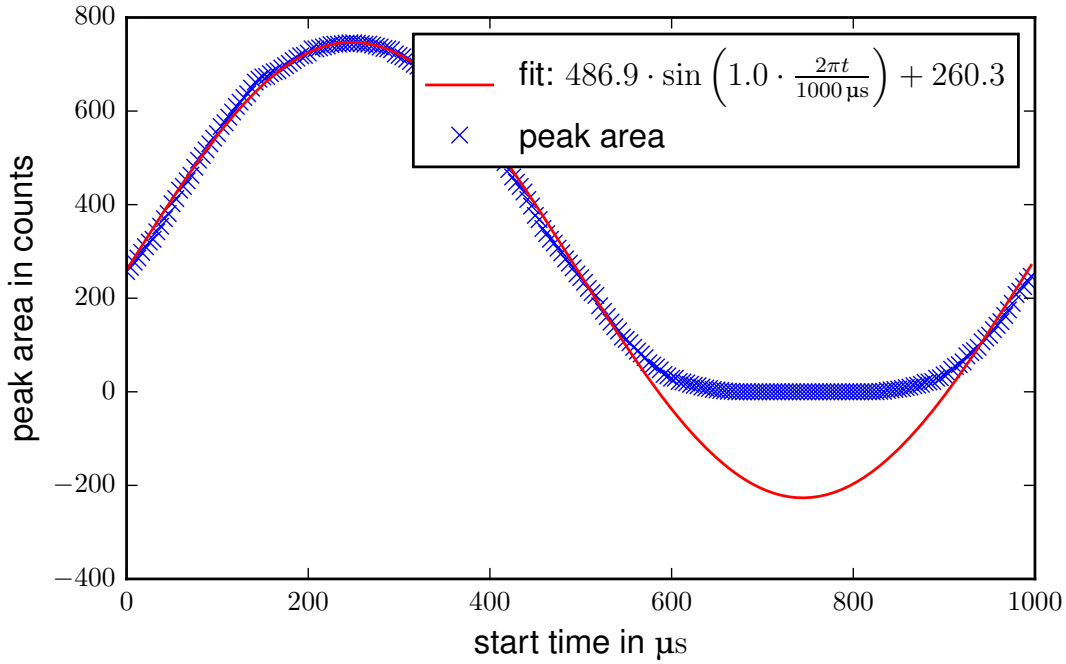


**Figure 5.7.** – **Peak area for 0.0 eV surplus energy:** The transmission clearly shows a sine-dependence on the starting time. For this plot all ten different phases, with 24 peaks each, are used. Only data points from 0 to 400 µs are used to fit the function $a \sin\left(b \cdot \frac{2\pi t}{1000}\right) + c$.

Electrons have a minimal ToF, depending on their kinetic energy, pitch angle and start time as can be seen from the plots. For very low surplus energies, where not every electron reaches the detector, there is no maximal flight time, since particles with an infinitesimally small longitudinal kinetic energy in the analyzing plane take an infinite time to reach the detector. This explains the tail in the upper plot in figure 5.8 on the next page. For surplus energies high enough for every electron to reach the detector, the maximal ToF is determined by electrons with the lowest energies, highest pitch angles and a start time where the acceleration voltage is at its minimum. For higher surplus energies the overall flight time is shorter as the electrons have higher velocities and a double-peak structure is created, because for positive accelerating voltages flight times are focused on the left peak, while at negative accelerating voltages flight times are focused in the right peak. This is illustrated in figure 5.9 on page 46 for 1.0 eV surplus energy and a phase shift of 0°.

These results show that applying a time-dependent potential to the downstream part of the MS leads to start-time-dependent flight times, which is the first step towards time-focusing-time-of-flight spectroscopy. However, for TFToF spectroscopy, the modulating frequency has to be of the same scale as the flight times, since electrons entering the spectrometer at a later time have to catch up with earlier ones. This is only possible if these have not reached the detector in the meantime.

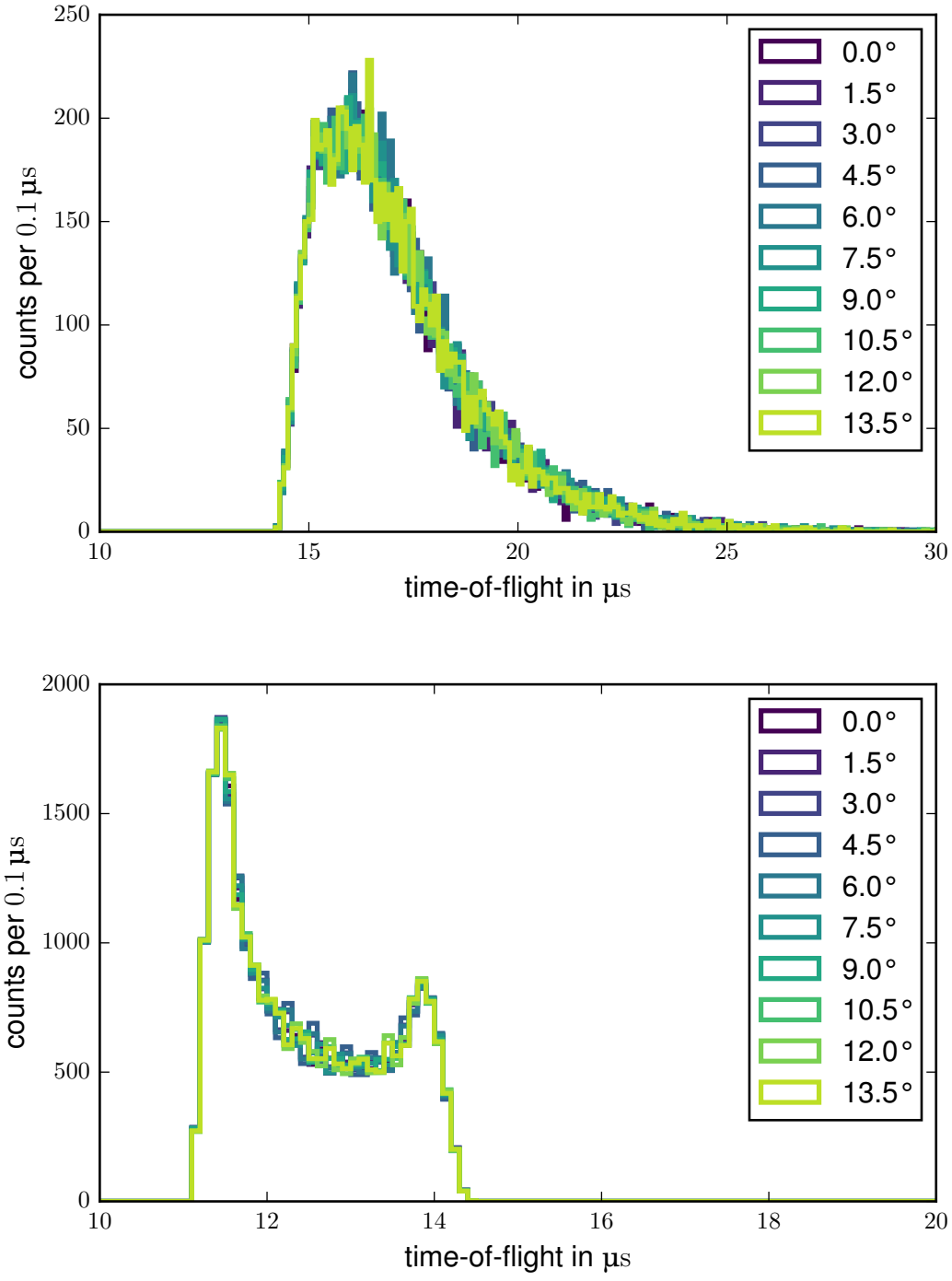


**Figure 5.8. – Time-of-flight histograms for 0.0 eV (top) and 1.0 eV (bottom) surplus energy:** For a low surplus energy electrons are blocked at lower potentials and the ToF spectrum has a single peak, while for higher surplus energies electrons get delayed at lower potentials and give rise to a two-peak structure. No significant difference can be seen between the various phases.

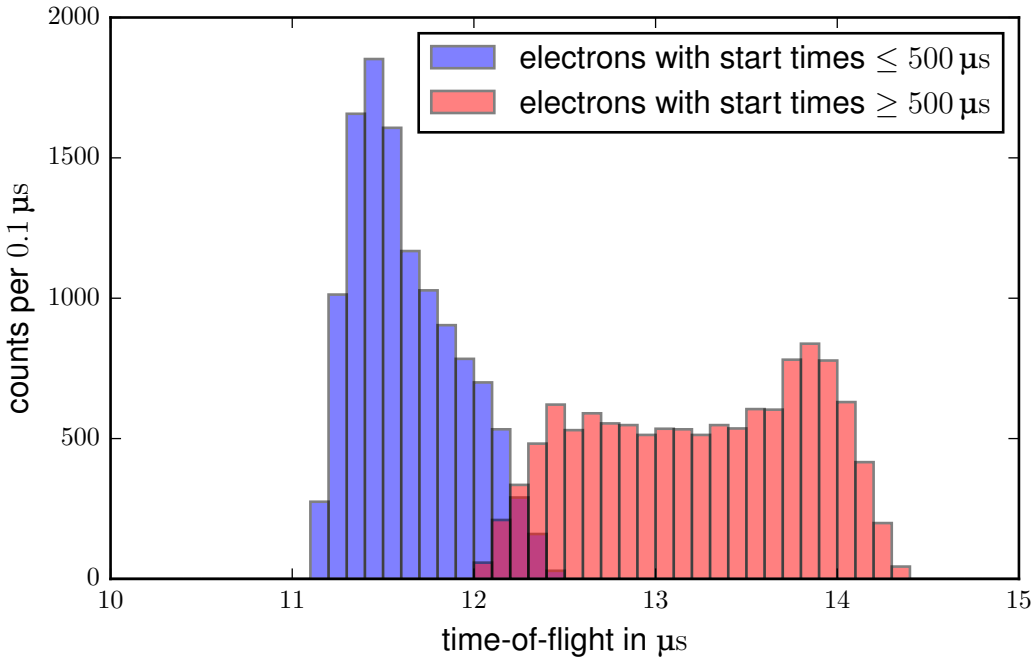


**Figure 5.9. – Double-peak structure for 1.0 eV surplus energy due to different start times:** Electrons started during a positive acceleration voltage (blue) have smaller flight times than electrons started at a time with negative acceleration voltage (red). Additionally the blue distribution is narrower than the red one due to higher kinetic energies in the AP resulting in a smaller velocity spread.

So far, it is not clear if frequencies in the 100 kHz region lead to additional effects, because with the low frequency of only 1 kHz used here, the potential is not changing much during an electron flight time. Thus, a particle is affected by a nearly constant potential, which is not true for high frequencies. Furthermore, supplementary investigations have to be carried out to see if the arrival times for different energies can be focused in such a way that energy information can be concluded from them. This is done in section 5.2.3.

### 5.2.2. SDS 2 Data Analysis

To validate the simulations of the split main spectrometer, the time-focusing-time-of-flight data taken in SDS 2 can be analyzed and compared to the results obtained above. The measurements are stored on the *KaLi* server[4] and can be accessed by *BEANS*, which is included in the Kasper framework. It comes with an example *sds-tof* program, which has been modified in order to account for the DAQ delay of 1270 ns determined

[4]The **Ka**trin data access **Li**brary (KaLi) is a C++ programming interface for data access and selection. For further information see [Kle14].

in [ELOG26] and to be able to count pile-up events correctly by using energy region cuts. The source code to the modified version can be found in section A.3, together with a *Python*[5] script to execute the program with the correct arguments. All results are stored in ROOT files for further processing.

For this purpose Kasper's *Peaberry*[6] is used to process the ROOT files with *IPython*[7]. The first cell contains the function *FindPeaks*, which can detect peaks in a spectrum, and the *Peak* class, which structures information about a peak in an object and allows for easy data access. The second cell reads data from the ROOT files to create **T**ime-**o**f-**A**rrival (ToA) spectra similar to the ones presented in the subsection about simulations. Additionally it utilizes the code written in the first cell to gather information about the peak area. It should be mentioned that all arrival times are shifted by half an interval, because it seems like either the Tektronix function generator used to drive the e-gun or the e-gun laser itself triggered on the wrong edge of the incoming square signal. This can be concluded, since without this shift the arrival times for electrons with 0° phase shift are positioned around the start times. For the time-of-flight this would result in $\tau = n \cdot 42\,\mu s$, where $n = 0$ is unphysical and values of $n \geq 1$ are too high, since even for very low surplus energies electrons should have flight times of under 25 µs, as can be seen in figure 5.8 on page 45. The most likely explanation is a wrong trigger, since delays of the data acquisition have already been taken into account and are only responsible for a very small shift of $\approx 1.3\,\mu s$ and half an interval shifts the flight times into the right region of around 20 µs. A similar issue was encountered during SDS 1 measurements, justifying the subsequent correction.

During the measurements the transmission edge has been determined experimentally and was used to calculate the surplus energy and it has not been noted whether the spectrometer was ramped during the transmission edge measurement. However, it is assumed here that this has been the case, introducing a possible $\pm 0.1\,eV$ shift on the surplus energy compared to the definition used in case of simulations. In the following, it will be distinguished between the surplus energy from the experiment and the surplus energy used in the simulations by explicitly referring to the one in question.

At first glance, the time-of-arrival spectrum for an experimental surplus energy of 0.0 eV shown in figure 5.10 on the following page looks similar to the simulated one. The difference in counts can be explained by the small number of electrons simulated

[5]Python is a high-level interpreted programming language, featuring object oriented programming and is designed for readability. See [Py] for more details.

[6]Peaberry has been developed in [Beh16] and is described there in detail.

[7]IPython provides a command shell for interactive computing and comes with a browser-based notebook which supports code and inline plots. For more information see [IPy]. The source code used for the analysis can be found in section A.4.

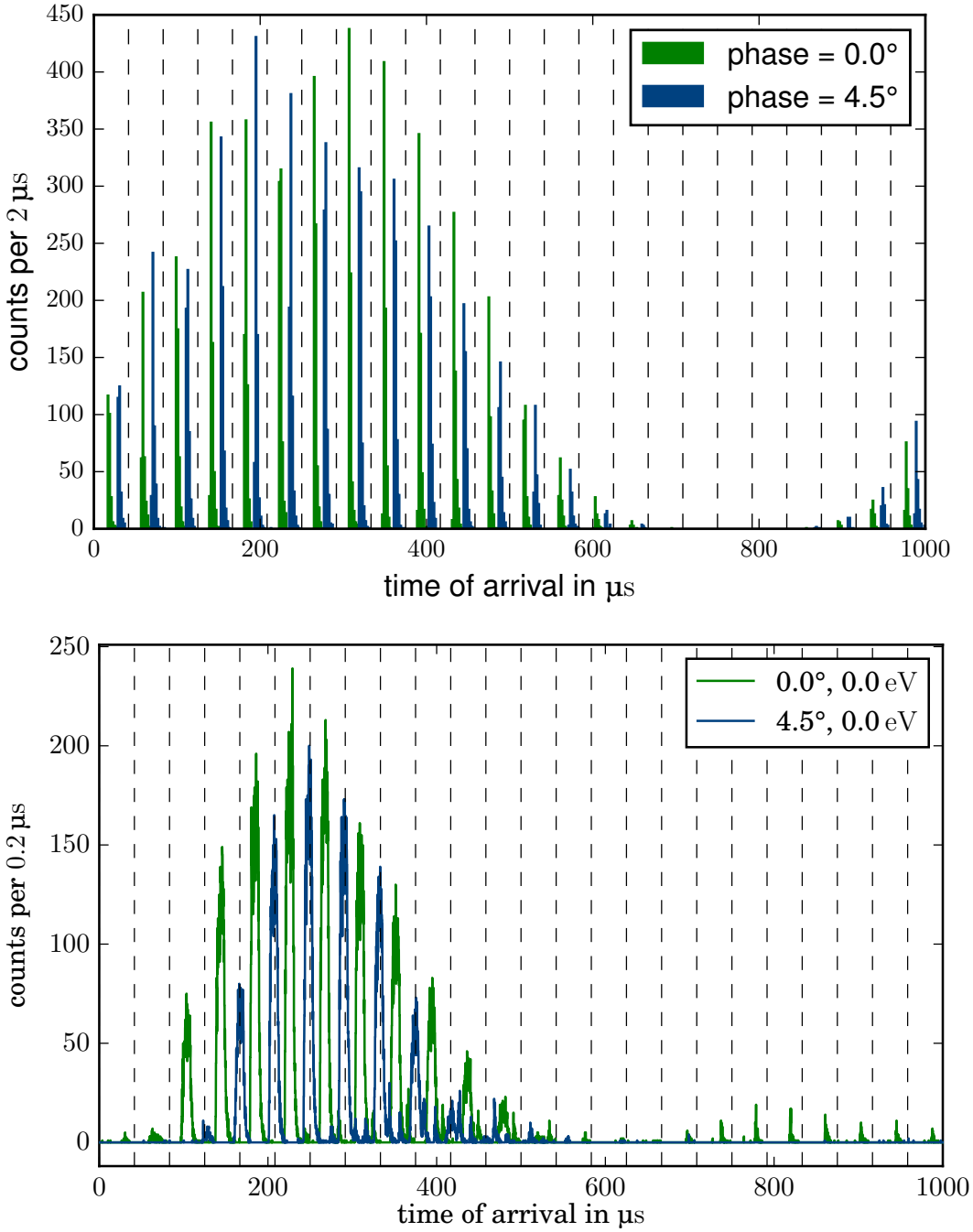


**Figure 5.10. – Comparison between simulated and measured time-of-arrival spectra for 0.0 eV surplus energy:** Both, the simulated time-of-arrival spectrum (top) and the measured one (bottom), share the same overall structure due to potential ramping. The dashed lines again indicate the start times for electrons with 0° phase shift.

per start time, while the broader time-interval in which electrons are transmitted is probably connected to the offset of the surplus energy. Figure 5.5 on page 42 shows a simulated spectrum with a similar transmission interval like for the measured one. The difference in surplus energy of 0.1 eV lies in the uncertainty region discussed above. Therefore, simulated data for $E_{\text{surp}}^{\text{simulation}} = -0.1\,\text{eV}$ will be compared to measured data for $E_{\text{surp}}^{\text{experiment}} = 0.0\,\text{eV}$ in the following.

While the general form of the measured time-of-arrival spectrum agrees with expectations and simulations, closer examination of the bottom plot in figure 5.10 on the facing page reveals a problem with the measured data. While there cannot be seen a large difference between the two neighboring peaks of different phases in the simulation, the experimental spectrum shows a huge discrepancy between the two plotted phases, especially for early arrival times. This behavior is present at each measured surplus energy and for each energy the spectrum for 0° deviates from all other phases.

A possible explanation for this observation is that a lower number of electrons is started in the e-gun for measurements with a phase shift $\Delta\phi > 0$. This is confirmed by analyzing the recorded run condition data, where a drop in the photo diode current after the first run is visible (see figure A.1 in the appendix). A lower current corresponds to a reduced light intensity, which decreases the number of released electrons in the e-gun. While such a drop is not expected from the setup, previous measurements with the e-gun also show an unexpected influence of the trigger signal width on the electron rate. Because the laser is set to trigger on the rising (or falling) flank, the width should not have an impact on the light output. Apparently a phase shift also changes the laser output and leads to the effect visible in figure 5.10 on the preceding page. Note that after the drop the current is stable, regardless of the phase shift value.

For further analysis quantitative information about the peaks are required, which can be obtained by the *FindPeaks* function from the Python code. It implements an algorithm which utilizes the rolling mean and is able to identify peaks by calculating the standard deviation of the current bin from the mean. The function returns a list filled with ones where the corresponding bin is part of a detected peak and zeros otherwise. Additional filtering excludes all bins below a certain threshold, peaks that are too narrow, i.e. a single bin, and peaks with an area below an adjustable fraction of the maximal peak area. All remaining peaks are stored in an array of *Peak* objects, containing information about their area as well as their position, once as mean between the left and the right edge and once as 50th percentile. Note that the peaks are not fitted and that the area extracted by the algorithm is simply the sum of the bin entries belonging to the peak. With the gained data it is possible to plot the number of

transmitted electrons versus the arrival time as done in figure 5.11. To account for the difference in started electrons, the peak areas are normalized in regard to the mean value of the photo diode current amplifier readout for each run.

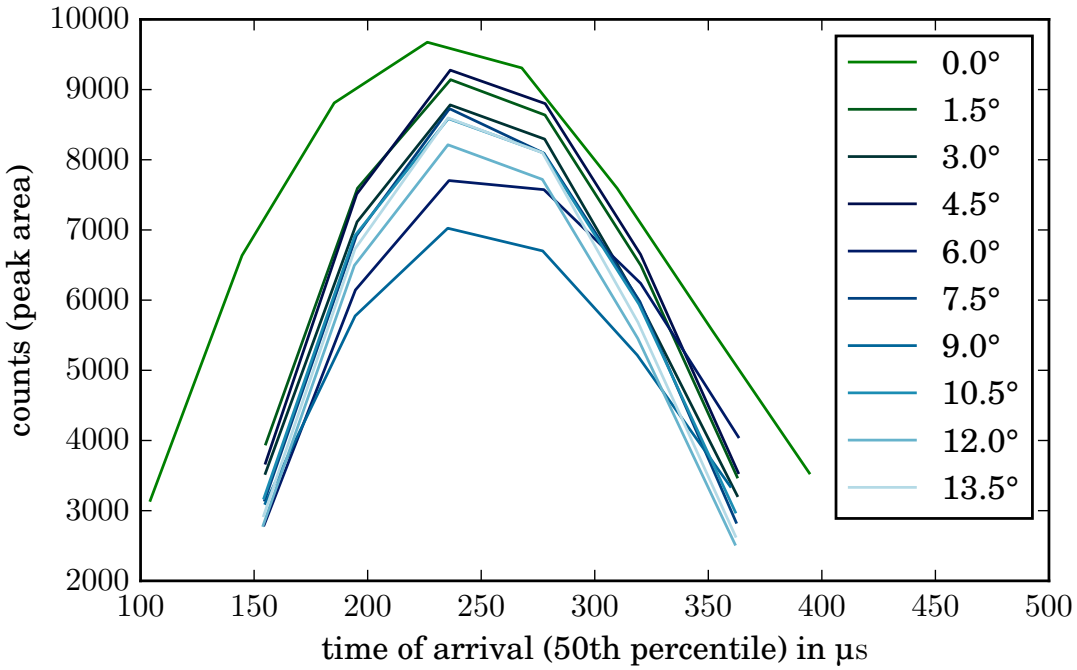


**Figure 5.11. – Peak area vs time-of-arrival for 0.0 eV surplus energy:** This plot shows the time-dependence of the number of electrons reaching the detector. An additional shift is introduced to each phase to correct the phase shift and achieve a common start time. An interpolation between the data points has been performed to increase perceptibility. Although the area is normalized to the photo diode current its phase-shift-dependence of the area is still unexpectedly large.

On the one hand the time-dependence for a single phase agrees with the expected one, showing a sinusoidal structure. Comparing different phases on the other hand shows that the absolute number of electrons varies between them. The most striking difference can be seen between 0° and all other phase shifts for early arrival times. The real waveform of the accelerating voltage at the inner electrode system could be responsible for this. A sine has a small slope near the maximum and therefore the number of transmitted electrons also only changes slightly near the maximum, as can be seen in figure 5.7 on page 44. If the waveform in the experiment is steeper near the maximum, differences between the phase shifts become more pronounced.

With the peaks 50th percentile positions available and the known start times from the e-gun pulsing, the time-of-flight can be calculated for each peak. Taking the mean from all detected peaks of a phase results in a loss of information about the start-time-dependence of the ToF, but allows for a quick comparison between the phases and the simulation in table 5.1 on the facing page.

**Table 5.1. – Measured and simulated time-of-flight for different phase shifts:** The measured ToF is based on the data for a surplus energy of 0.0 eV, while the simulated surplus energy is −0.1 eV.

| phase shift in ° | 0.0 | 1.5 | 3.0 | 4.5 | 6.0 | 7.5 | 9.0 | 10.5 | 12.0 | 13.5 |
|---|---|---|---|---|---|---|---|---|---|---|
| ToF in µs (meas.) | 19.0 | 29.0 | 28.8 | 29.0 | 28.6 | 28.5 | 27.6 | 28.0 | 27.8 | 27.9 |
| ToF in µs (sim.) | 18.3 | 18.3 | 18.3 | 18.3 | 18.2 | 18.2 | 18.2 | 18.3 | 18.3 | 18.3 |

Again, a discrepancy can be seen between the value for a phase shift of zero and all other phases for the measured data. Such a difference is not expected and not present in the simulated data. The flight times for all nonzero phase shifts are consistently to large by about 10 µs. The only flight time in accordance with the simulations is the one for 0.0°. It seems like introducing a phase shift results in an unwanted additional offset, which is independent of the shift value. This provides further evidence that the triggering of the e-gun laser behaves unexpected when $\Delta\phi > 0°$ is used.

Preserving the start time information gives rise to figure 5.12 on the next page. It shows that measurements and simulations yield comparable results for the 0° phase shifted time-of-flight. Near the minimum ToF the two datasets show nearly no deviation, while the measured flight time is larger than the simulated one far from the minimum. This issue is probably connected to the real form of the accelerating voltage reaching the electrode system as well. If the real acceleration voltage at a certain time is lower than it would be for a sine modulation, electrons have higher flight times. This is a further hint that near its maximum, the real waveform is steeper than a sine. At the minimal flight time $\tau_{\min}$ the difference between simulations and measurements is also minimal, because both waveforms reach the same maximum. Furthermore, small differences in the maximal accelerating voltage are suppressed because of the high kinetic energies and the corresponding small velocity spread at that times.

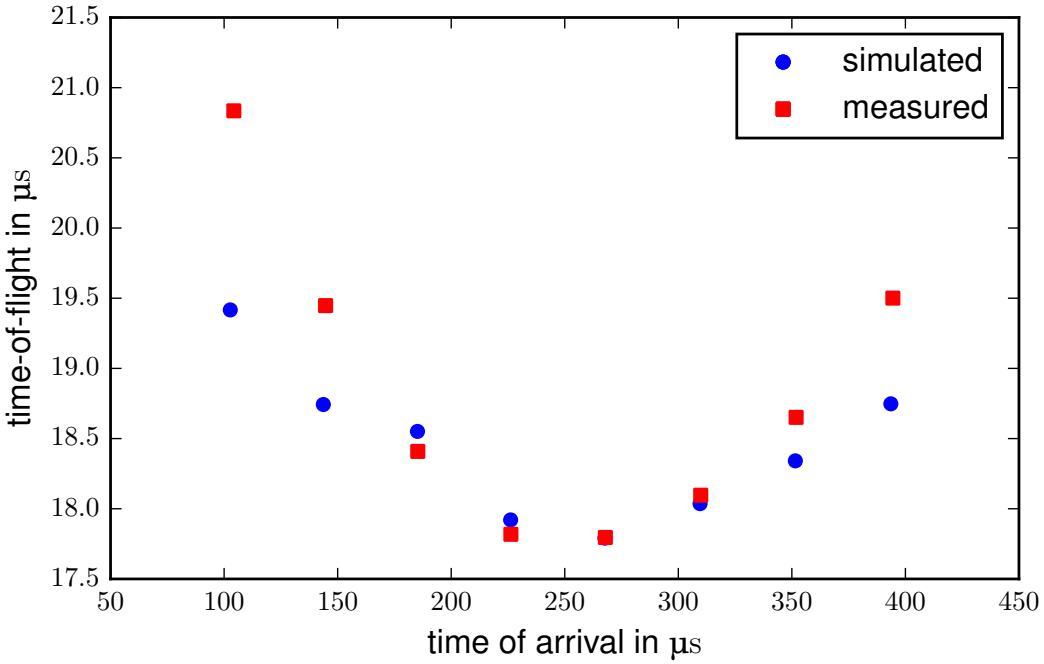


**Figure 5.12.** – **Measured and simulated mean time-of-flight vs arrival time:** This figure shows the flight-time-dependence on the arrival time. The simulated data (blue) belongs to a surplus energy of −0.1 eV, while the measured data belongs to 0.0 eV surplus energy and both datasets are based solely on the peaks for a phase shift of 0.0°.

In the last part of this subsection it is investigated if the surplus-dependence is in accordance with simulations and expectations. For the simulated spectra the peak area stays constant for $E_{\mathrm{surp}} \geq 0.5\,\mathrm{eV}$, which is expected because all electrons are transmitted as already calculated in equation (5.2) on page 43. However, in the experiment the number of electrons reaching the detector stays time-dependent. For high surplus energies of 5.0 eV this can be seen in figure 5.13 on the next page. The behavior of the nonzero phase shift measurements contradict the expectancy again. Contrary to the issues above, the e-gun laser triggering cannot be made responsible for the problem here. A reason for the unexpected behavior could be the small secondary peaks visible between the primary ones in figure 5.14 on the facing page. These small peaks are filtered out because their origin is unclear and they do not show up in the simulated data. They could represent electrons that are reflected by the retarding potential at times with a lower accelerating voltage. If these electrons are reflected again at the spectrometer entrance they may be able to pass the analyzing plane during a time with a higher accelerating voltage. No time information can be concluded from such electrons, because the time between reflection and transmission is unknown.

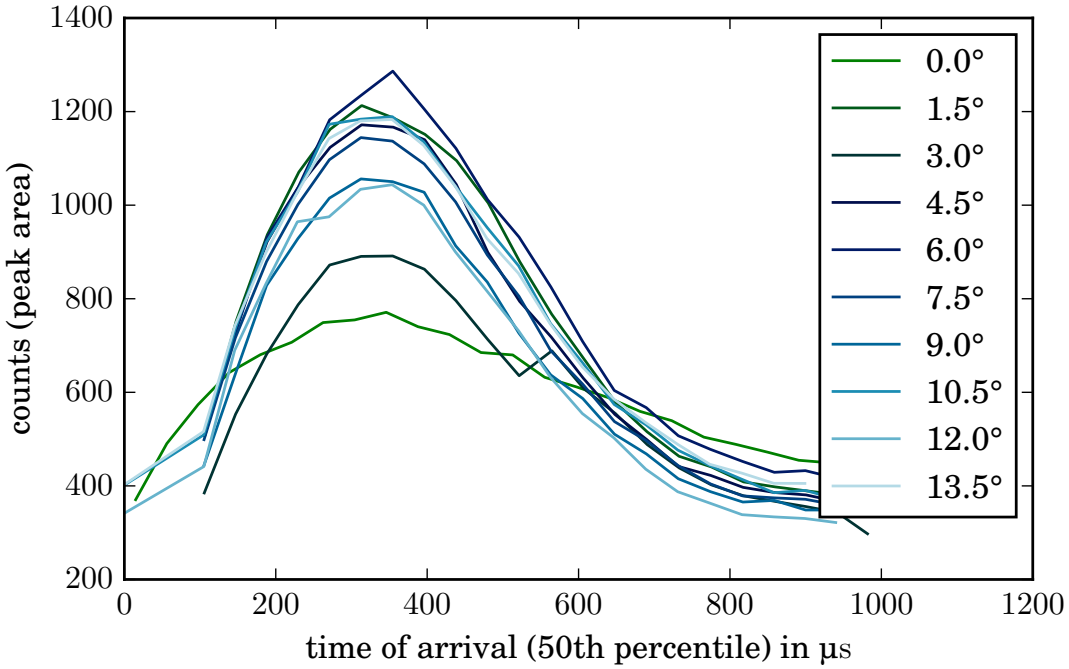


**Figure 5.13.** – **Peak area vs time-of-arrival for 5.0 eV surplus energy:** The curve for a phase shift of 0° is noticeably flatter than in the case of a low surplus energy, although a variation is still clearly visible. Other phases still show a distinct time-dependence.

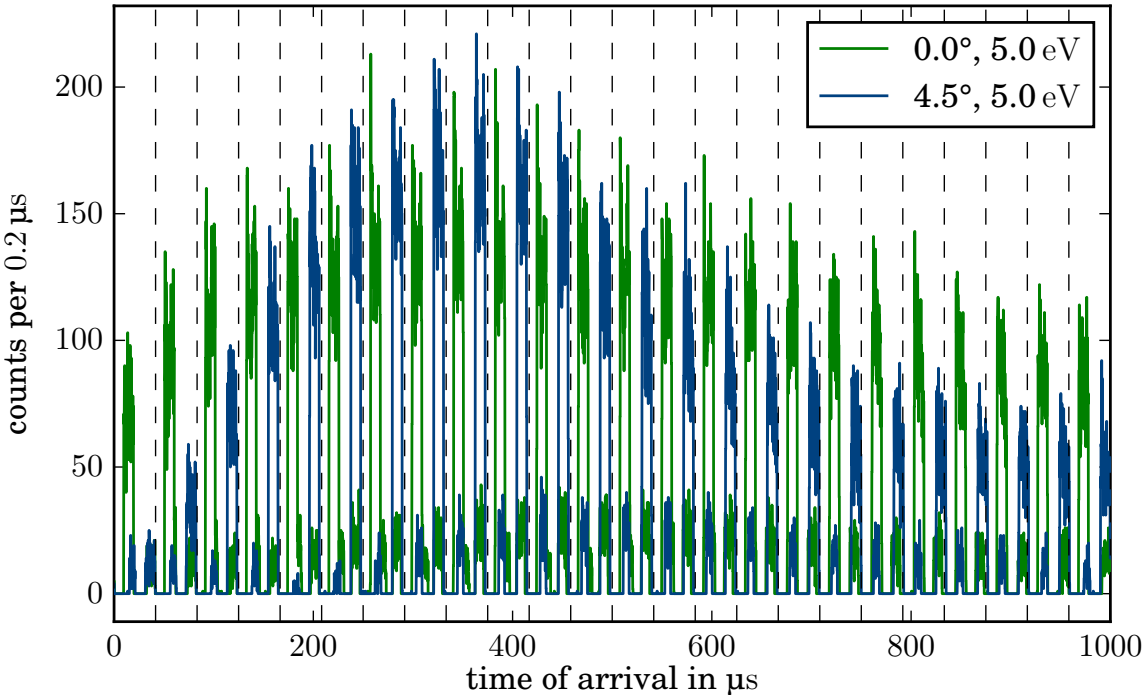


**Figure 5.14.** – **Measured time-of-arrival spectrum for a high surplus energy of 5.0 eV:** For high surplus energies the spectrum still shows a time-varying peak height, but electrons reach the detector regardless of their start time. The origin of the small peaks (below 50 counts per bin) between the large ones is unknown and they are filtered out by the peak detection algorithm.

In conclusion, the comparison between the simulated and measured data is conflicting. On the one hand the general structure of the measured spectra resembles the measured one and for the first measurement without phase shift, the obtained flight times are close to the simulated values. The small deviations for certain arrival times are probably due to the waveform of the accelerating voltage not being a perfect sine. On the other hand the detailed analysis revealed that for nonzero phase shifts the measured data does not conform with simulation results. The laser intensity drop is responsible for the lower count rates when a phase shift is introduced. In addition, a constant shift of around 10 µs is added to the start times, indicating further problems with the e-gun laser triggering. Because the measurements were done in SDS 2, nearly half a year before the start of this thesis, and cannot be repeated due to constructions and modifications at the KATRIN site, some of the encountered discrepancies could not be resolved completely. One major problem for the analysis is that the waveform of the accelerating voltage at the inner electrode system is unknown. As shown above, a sine cannot perfectly describe the measurements and a waveform closer to the one shown in figure 5.4 on page 41 may be able to reproduce the measured data more closely. However, for a time-focusing effect higher frequencies are necessary and these are technically easier to realize with a sine, which is therefore used in the next subsection.

The most important insight gained from the analysis is that the KATRIN main spectrometer can be used in a split setup in order to modify the electron time-of-flight depending on the phase of the potential-modulating waveform, as shown in figure 5.12 on page 52. If this can be done in such a way that the arrival times for certain energies are focused will be examined in the next subsection.

### 5.2.3. TFToF Parameter Optimization

In figure 5.12 on page 52 the flight time changes by about $\Delta\tau = 1.5\,\mu s$ during $\Delta t_0 = 150\,\mu s$ for the simulated electrons and about $\Delta\tau = 3.0\,\mu s$ for the measured particles. For an ideal time-of-arrival focusing effect, $\tau$ has to decrease linearly with the start time $t_0$, so that

$$t_0 + \tau(t_0) = t_{\text{arrival}} = constant \,\forall\, t_0\,. \tag{5.3}$$

When a sine function is used to modify the potential, it can only focus electrons during half its period, from the minimum of the accelerating voltage to the maximum and a maximal time-focusing would be present if electrons getting the maximal acceleration catch up with the ones accelerated the least. This means that the flight time difference introduced by the accelerating voltage should be around half the period of the modulating function. However, this does still not focus every electron with the same energy in this time interval onto a common arrival time, since the velocity is inversely proportional to the square root of the kinetic energy and not the sine. This consideration also neglects that an electron, moving through a time-varying potential with a period near the time-of-flight, will not only be influenced by a single value of the accelerating voltage. This is especially true in the case of the split main spectrometer in contrast to a dedicated spectrometer as explained in the next subsection.

Besides the frequency, the amplitude of the accelerating voltage presents another important parameter for TFToF methods, since it determines the maximal energy difference and therefore also $\Delta\tau_{\text{max}}$. In order to find suitable values for both parameters the split main spectrometer has been simulated with the five different frequencies and four different amplitudes of the accelerating voltage found in table 5.2. The hull voltage has been increased to $-18200\,V$ and the IE common voltage has been set to $-450\,V$ relative to the vessel. This allows for an applied offset of $-50\,V$ to $-450\,V$ for rings 12 to 16 and avoids a setting where the wire electrodes are on a more positive potential compared to the vessel hull. While in the simulations such a setup is possible, in the real experiment this would present a technical challenge and should be avoided.

**Table 5.2. – Simulated acceleration parameters for the split main spectrometer.**

| frequency $f$ in kHz | 100 | 200 | 400 | 800 | 1000 |
|---|---|---|---|---|---|
| peak-to-peak amplitude $U_{\text{pp}}$ in V | 50 | 100 | 200 | 400 | - |

For each parameter combination electrons with three different angles and ten different starting times have been simulated to scan the whole waveform. To perform time-focusing-time-of-flight spectroscopy, it is not only necessary to focus electrons with the

same energy on a common arrival time, but this arrival time also has to be different for other energies. In addition to the aforementioned electron properties, three different surplus energies have therefore been chosen for each frequency and amplitude setting. Again, the amount of gathered data is too large to be presented here and the results will be discussed by example.

For fixed parameters of the potential modulation, the electron surplus energy affects the obtainable flight time difference. For a higher electron surplus energy several effects are noticeable when comparing the curves for the different surplus energies in figure 5.15 on the next page. Besides the overall lower flight time in case of higher energies, the maximal ToF difference $\Delta\tau_{\max}$ between electrons with the same energy and pitch angle is also decreased. In contrast to the less pronounced divergence between the curves for different pitch angles, this is not desired and leads to a trade-off between the attainable ToF difference and angular focusing. If the flight times for electrons with the same energy and start time but different pitch angles vary too much, they can overlap with flight times from electrons with different energies and pitch angles and thus it becomes impossible to gain energy information from the arrival times.

The frequency used to ramp the potential also has a major impact upon the attainable $\Delta\tau$. While for a low frequency of 50 kHz the maximal difference in ToF is about $\Delta\tau_{\max} = 2\,\mu s$ (red curve in the upper plot of figure 5.15 on the facing page), for a very high frequency of 1000 kHz there is no noticeable start-time-dependence (lower plot of figure 5.15 on the next page). This is due to the very small period of only 1 µs compared to the flight times of $> 5.5\,\mu s$. At such high frequencies every electron is accelerated and decelerated multiple times during its flight through the main spectrometer, hence averaging out the influence of the accelerating voltage. On the one hand this means that once a certain frequency is reached it does not make sense to further increase it, while on the other hand a low frequency does not allow later electrons to catch up with earlier ones. The achieved $\Delta\tau_{\max} = 2\,\mu s$ in the case of $f = 50\,kHz$ (marked by the arrow in figure 5.15) is still small compared to the start time difference of $\Delta t_0 \approx 6.7\,\mu s$ and hence cannot result in time-focusing. Together this limits the range in which a time-focusing frequency can be found. The optimal frequency also depends on the amplitude, because together they determine the potential change during a given time.

Increasing the amplitude is expected to also increase the value for $\Delta\tau$, but the amplitude is limited by the fact that it influences the retarding potential in the analyzing plane, hence worsening the energy resolution. For $U_{pp} = 50\,V$ this variation was rather small with an impact of $\pm 0.1\,V$, but it rises to around $\pm 0.75\,V$ for a peak-to-peak

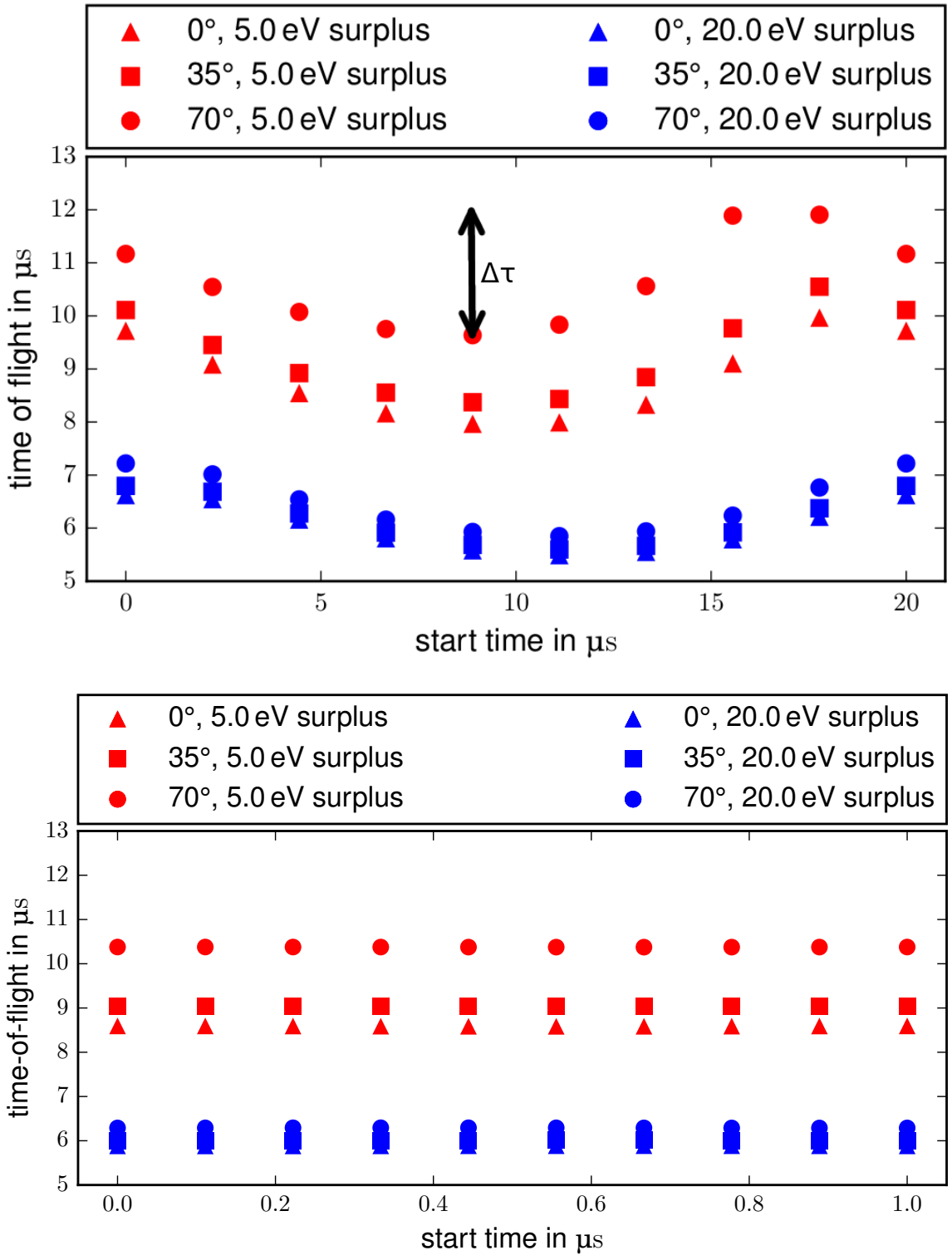


**Figure 5.15.** – **Impact of frequency and surplus energy on the time-of-flight:** Plotted here is the flight time versus the start time for a frequency of 50 kHz (top) and 1000 kHz (bottom). In both cases the peak-to-peak Voltage is 100 V and the different symbols indicate different starting pitch angles inside the PS2 magnet. The maximal pitch angle for this setup is $\approx 71.6°$, so the three chosen values cover nearly all allowed angles. Additionally the surplus energy is color coded (5.0 eV in red and 20.0 eV in blue).

amplitude of 400 V. This additional energy uncertainty of 1.5 eV further impairs the already declined energy resolution in this setup. Compared to the nominal value for the energy resolution of $\Delta E = 0.93\,\text{eV}$, a value of $\Delta E \approx 3.5\,\text{eV}$ is considered too much of a drawback. Since the idea behind time-of-flight methods is to gain additional information without an excessive loss in energy resolution, $U_{\text{pp}} = 400\,\text{V}$ is only used to demonstrate the impact of the amplitude.

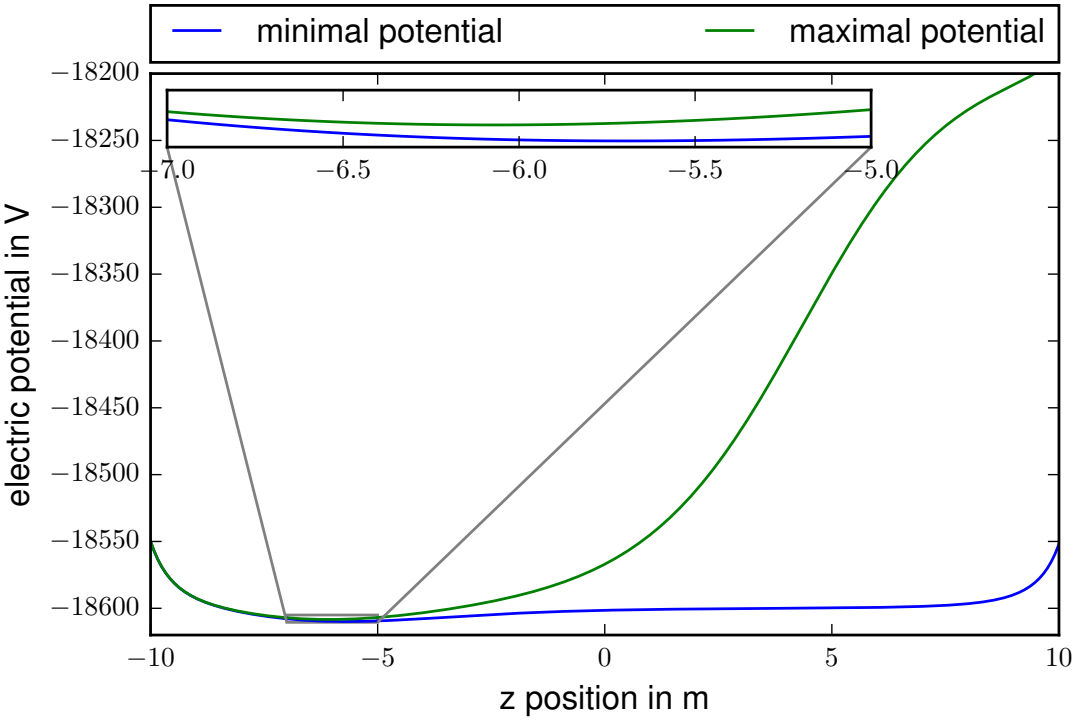


**Figure 5.16. – Electric potential inside the split main spectrometer for $U_{\text{pp}} = 400\,\text{V}$:** The blue line shows the potential where the accelerating voltage is at its minimal value, while the green curve represents the maximal accelerating voltage. The variation of the retarding potential in the analyzing plane shown in the inset is about 1.5 V and for the green curve a slight shift of the minimum to the left can be observed.

By changing the representation of the simulated data to show the arrival time instead of the flight time, it becomes easier to identify suitable parameters. Data with an optimal time-of-arrival-focusing should show a slope of 0, while any higher value means that electrons are not having the same arrival time. Figure 5.17 on the facing page shows one of the best results obtained from simulations.

Unfortunately, it seems like even with a very high accelerating voltage of up to 400 V and a frequency of 200 kHz it is not possible to focus electrons on a common arrival time. An explanation can be given by the form of the accelerating potential shown in figure 5.16. The difference between the minimal and maximal potential only rises rather slowly and the full impact of the accelerating voltage is reached just before the

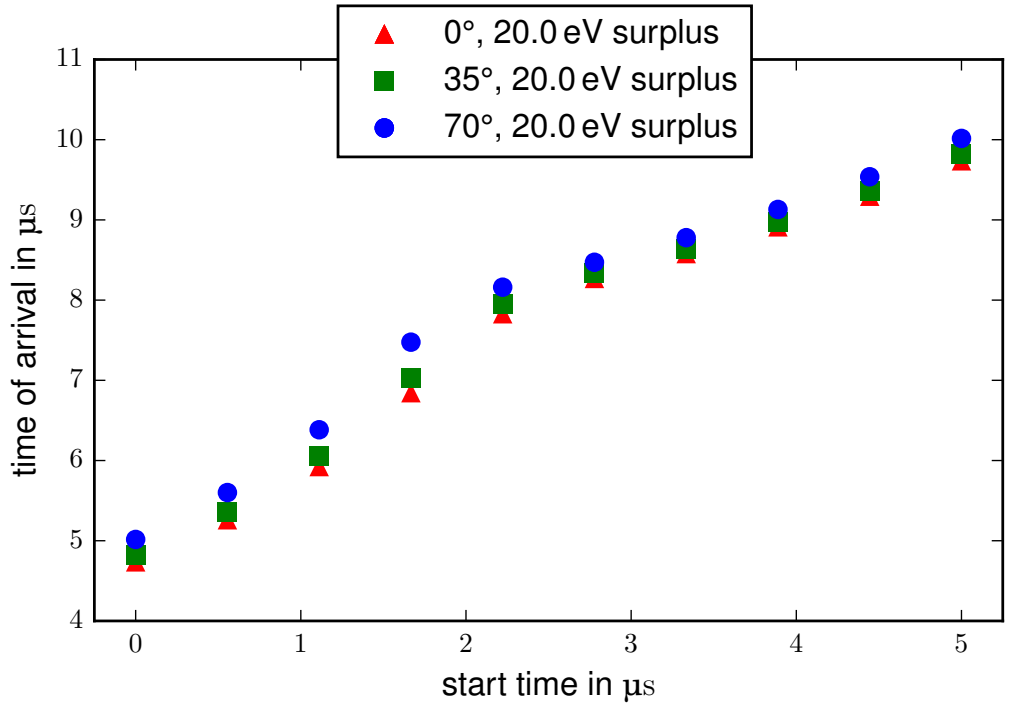


**Figure 5.17.** – **Best achieved time-focusing with the split main spectrometer:** The data for $U_{\mathrm{pp}} = 400\,\mathrm{V}$ and $f = 200\,\mathrm{kHz}$ shows a notable kink at a start time of around 2 µs after which the slope is decreased. The part with the decreased slope indicates the fraction of the waveform where electrons are focused. The time-focusing effect is still weak and the remaining slope still significantly differs from 0.

exit of the spectrometer. Apparently this setup results in delay line too short for the different electron velocities to have a major impact on the flight-time.

Additionally, electrons with 5 eV surplus energy are up to several microseconds in the ramped downstream part of the spectrometer, thus getting influenced by a large fraction of the whole accelerating waveform for high frequencies. Hence, they are accelerated and decelerated several times, averaging the acceleration effect.

In order to test if a steeper potential rise improves focusing, it is possible to start electrons farther away from the axis at $r = 3.5\,\mathrm{cm}$, so that they take trajectories closer to the electrodes of the spectrometer[8]. On such a trajectory, the potential follows the one from the electrode system more closely as can be seen when comparing figure 5.16 on the facing page with figure 5.18 on the next page. The electric field on both trajectories is plotted in figure 5.19 on the following page for the maximal accelerating voltage.

[8] A 2D visualization of the trajectory through the spectrometer can be found in figure A.3 in section A.6.

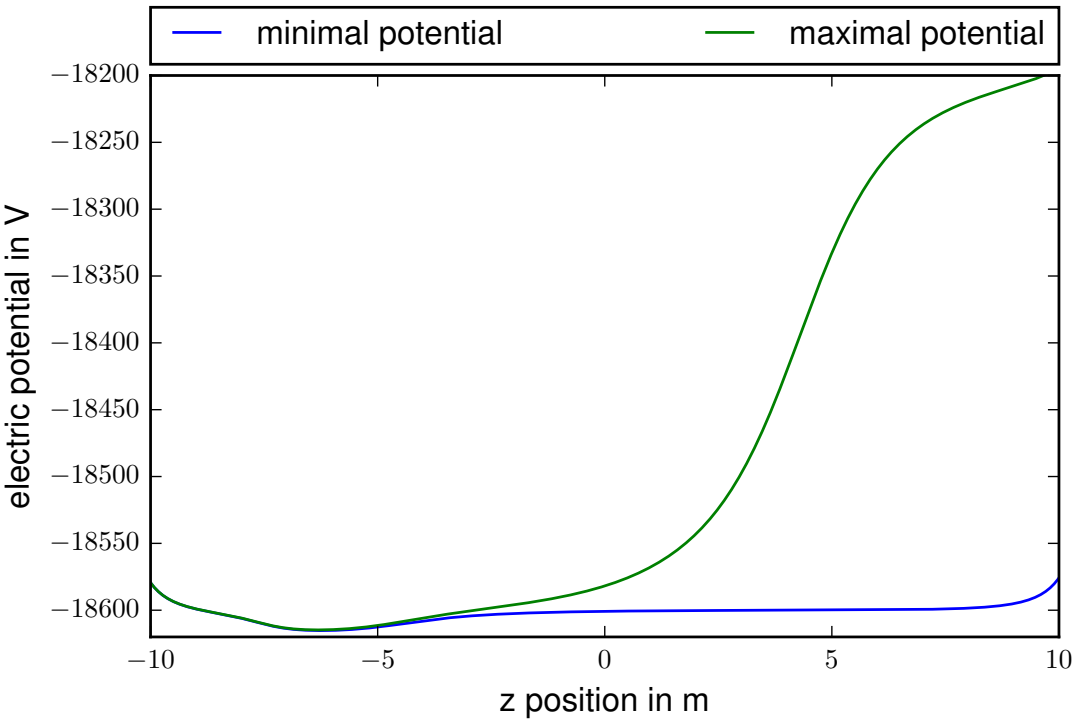


**Figure 5.18. – Electric potential inside the split main spectrometer for $U_{pp} = 400\,V$ on an outer trajectory:** The accelerating potential rises steeper than on the axes (compare figure 5.16 on page 58). Additionally, electrons on an outer trajectory reach the maximal potential difference sooner and thus have a slightly longer delay line available.

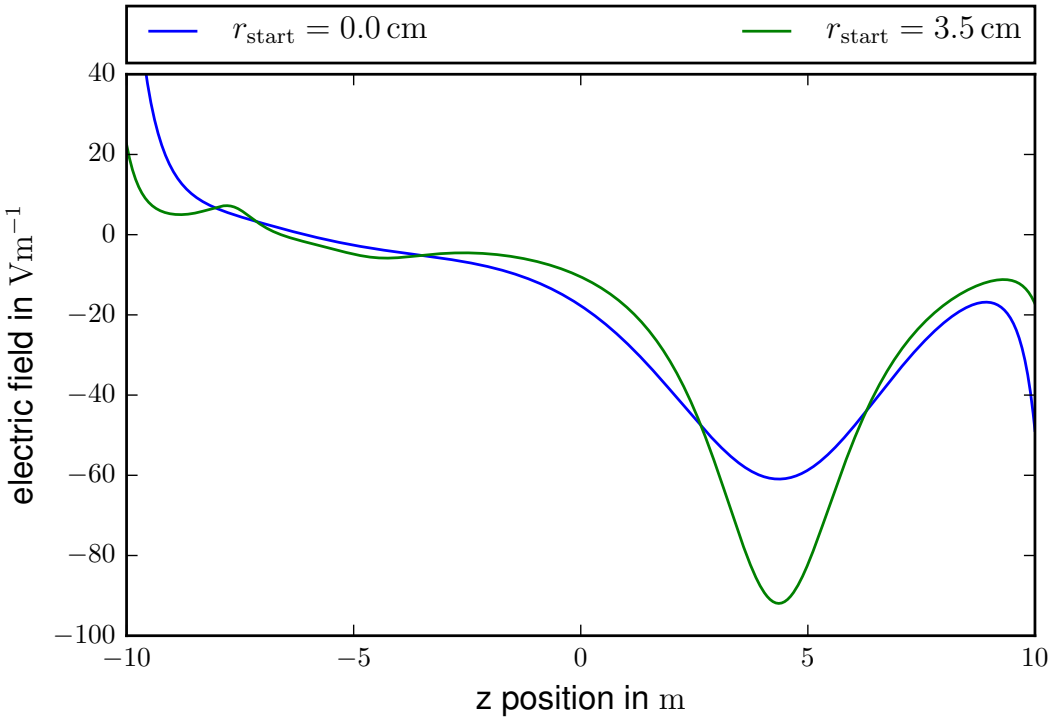


**Figure 5.19. – Electric field in z direction inside the split main spectrometer for $U_{pp} = 400\,V$:** The steeper potential rise leads to a stronger accelerating field for electrons started at $r = 3.5\,cm$ (green). Both curves show the electric field at the maximal accelerating voltage.

For the outer trajectory, the accelerating field is significantly stronger and figure 5.20 shows that a slightly better time-focusing can indeed be achieved.

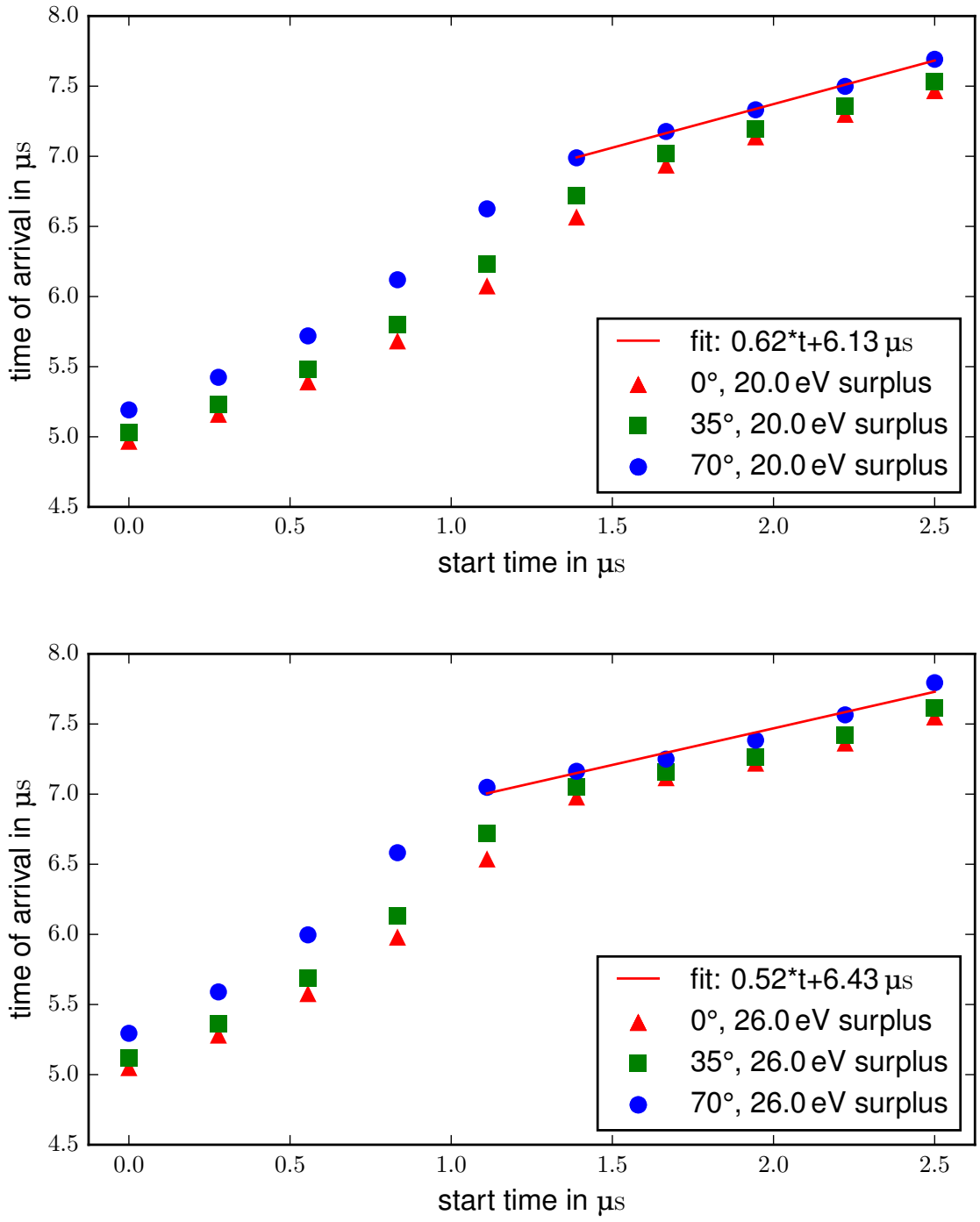


**Figure 5.20.** – **Impact of the starting radius on the time-focusing:** The upper plot shows time-of-arrival data for electrons started at $r = 0$ and the bottom one represents $r = 3.5\,\mathrm{cm}$ data. The ramping parameters for both datasets are $f = 400\,\mathrm{kHz}$ and $U_{\mathrm{pp}} = 400\,\mathrm{V}$ and a linear fit $a \cdot t + b$ has been calculated for the last 5 (6) electrons with pitch angles of 70 °.

In conclusion, the split main spectrometer setup can be used to alter the arrival times of electrons, but only up to a small extent not sufficient for time-focusing-time-of-flight spectroscopy. The simulations agree with the corresponding SDS 2 data under the assumption that for phase shifts other than 0° the measurements are yielding wrong results due to the unexpected trigger behavior of the e-gun laser. It has been shown that the amplitude of the applied ramped potential is limited due to interference with $U_{\mathrm{ana}}$. In theory, the variation of $U_{\mathrm{ana}}$ can be reduced by also modulating the voltage applied to the upstream part with a 180° phase shifted waveform. The destructive interference of both waveforms can stabilize the retarding potential, but the technical realization of this workaround is really challenging and it is unclear if $U_{\mathrm{ana}}$ can be held constant for every radius $r$. Furthermore, the frequency is limited due to the flight time of particles in the ramped part of the spectrometer. Within these limits no time-focusing parameters could be found, because the setup does not seem suitable for that task. The short delay line and weak electric field at the axis represent inherent problems of the split main spectrometer and are responsible for the insufficient time-focusing. This has been confirmed by using electrons on outer trajectories where the accelerating field is stronger and the delay line is slightly extended.

## 5.3. Third Spectrometer

The problems discussed in the previous subsection can be solved by using a dedicated spectrometer in an additional TFToF section between the main spectrometer and the focal-plane detector section. A third spectrometer can provide a longer delay line for the different velocities to take effect. Additionally, the amplitude limitation of the split main spectrometer is overcome, since the retarding potential is no longer influenced by the accelerating voltage. Although it is doubtful that a third spectrometer similar to the MS will be added to KATRIN in the near future, it could present a possible option for a later upgrade. Currently it is planned to use a higher magnetic field inside the MS to reduce the extent of the flux tube in order to improve background shielding [Har15]. With a smaller flux tube, a new spectrometer could be considerably smaller and therefore cheaper. Furthermore, by avoiding a long exposure to air, the new section would probably generate a significantly lower background. Because the low energetic isochronous background from the MS would be time-focused as well, a third spectrometer could be used for background discrimination. This section focuses on a more qualitative analysis of the time-focusing capabilities, while the next chapter discusses sensitivity limits for time-focusing-time-of-flight spectroscopy.

For the main spectrometer, the biggest changes in the electric potential are located at the entrance, where it drops from ground potential down to $\approx -18.5\,\mathrm{kV}$ on a very small spatial scale, or vice versa at the exit. Once electrons have passed the area with the strong electric field at the entrance, the spectrometer tank acts as a Faraday cage and the interior is nearly field-free. This results in electrons entering the spectrometer being affected by the accelerating voltage only during a short time. They then move through the vessel with a nearly constant velocity, depending on the time of entrance. The time-dependent field at the exit only has a negligible effect on the flight-time, because of the high kinetic energies $E_{\mathrm{kin}} > 18500\,\mathrm{eV}$ after leaving the spectrometer.

In order to find appropriate settings for the ramping function, a parameter scan is carried out, using five different frequencies and four different amplitudes. The retarding potential of the main spectrometer is set to $U_{0,\mathrm{main}} = 18555\,\mathrm{V}$ to analyze the last 20 eV below the endpoint. This is also the value of the retarding potential in the third spectrometer at the minimal accelerating voltage $U_{0,\mathrm{third}}$. Two more potential settings are used for the third spectrometer, where $U_{0,\mathrm{third}} = U_{0,\mathrm{main}} + 5{,}\mathrm{V}$ is used as the minimum. The used amplitudes and frequencies are listed in table 5.3 on the following page. For each combination 100000 electrons with an energy distribution following the one from the $^3$H $\beta$-decay, a uniformly distributed random start time and a random pitch angle up to the maximal value of 60°, are simulated.

**Table 5.3. – Frequency and amplitude values used for the third spectrometer simulations.**

| frequency $f$ in kHz | 50 | 100 | 150 | 200 | 400 | - |
|---|---|---|---|---|---|---|
| peak-to-peak amplitude $U_{pp}$ in V | 25 | 50 | 100 | 150 | 25+5 V offset | 50+5 V offset |

To get a quick overview, the simulation results can be illustrated in a two-dimensional histogram with the arrival time on the x-axis and the surplus energy on the y-axis. Because the time-of-arrival can only be measured modulo the period of the voltage waveform in the experiment, it makes sense to also plot arrival times from the simulation modulo the used frequency. Of course, in the experiment, only the arrival time bins (horizontal axis) can be measured, but the surplus energy axis is useful when it comes to understanding the simulated data.

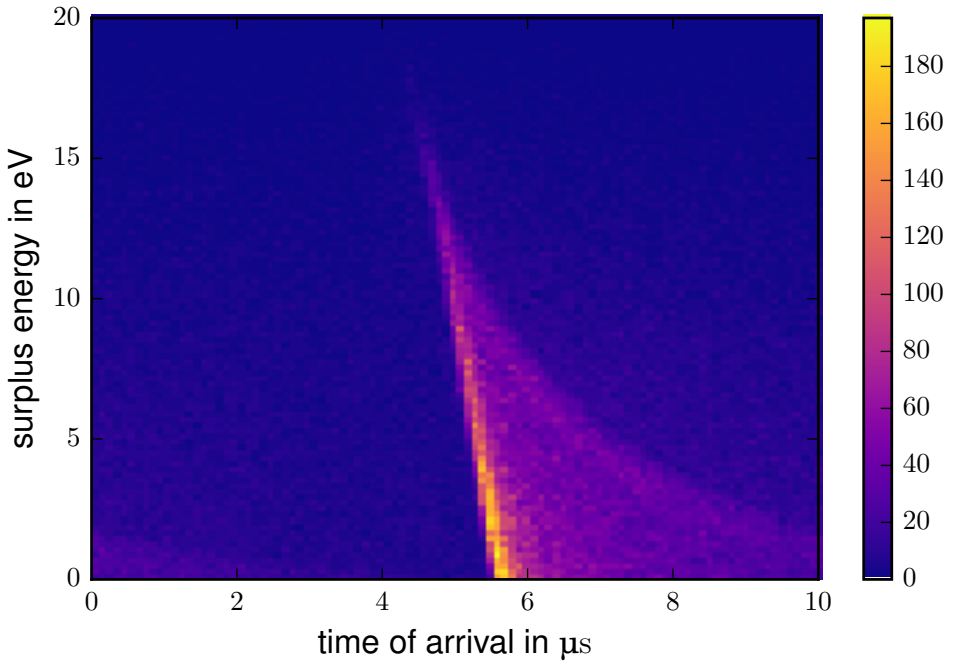


**Figure 5.21. – Surplus energy vs arrival time 2D histogram for f = 100 kHz and $U_{pp}$ = 50 V:** This graph shows how a 2D histogram can give a quick impression if the chosen parameters are suitable for time-of-arrival-focusing.

From figure 5.21 it can be seen that electrons with high surplus energies are focused on a narrow band of arrival times, which gets broader for lower energies. The highest populated region is at the left edge of the band and the broadening for low surplus energies can be explained by the fact that for electrons with smaller energies the angle has a huge impact on the flight time. Electrons with energies just slightly above the retarding voltage can have very long flight times, if they enter the spectrometer at its

lowest potential, and when the arrival time is taken modulo the period all arrival times are populated in the histogram.

An ideal time-of-arrival focusing would result in a single, narrow and straight line going from the top left to the bottom right of the histogram, since this would enable an energy reconstruction from the measured flight times. Such an ideal outcome is not expected, but it is possible to tune the parameters of the simulation in a way to obtain the best possible result. While a higher amplitude generally increases the time-focusing it also steepens the focused arrival time band. Because the detector system has a limited time resolution, an excessive amplitude leads to loss of information. Comparably a higher frequency can lead to better time-focusing, because of the larger difference in potential during a certain time. Increasing the frequency also reduces the available arrival times due to the smaller period, so that a flatter arrival time band will result in electrons with different energies having the same arrival time. The broadening for low energetic electrons seen in figure 5.21 on the facing page can be reduced by increasing the minimal applied potential above the one from the main spectrometer. This is the reason for the two additional simulated settings mentioned above and the effect can be seen when comparing figure 5.21 on the preceding page with figure 5.22.

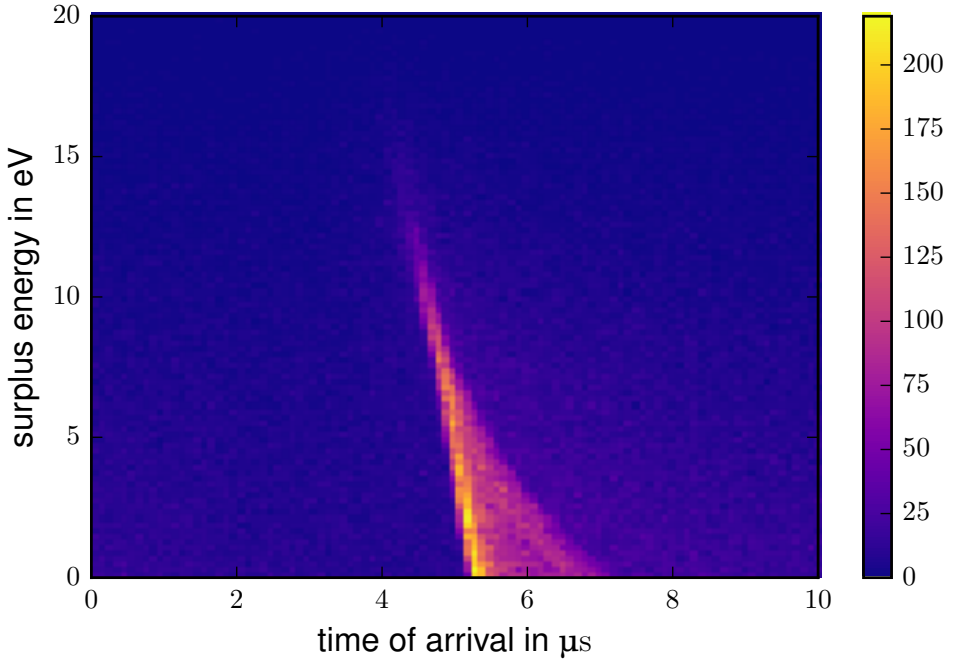


**Figure 5.22. – Surplus energy vs arrival time 2D histogram for f = 100 kHz and $U_{pp}$ = 50 V with an additional shift of +5 V:** By introducing an additional positive offset to the applied potential, the broadening at low electron energies becomes less pronounced. On the downside, electrons with large surplus energies are focused less due to the overall higher velocities.

Besides the 2D histograms, the simulation results can also be presented in 1D time-of-arrival histograms like they are obtained in a real experiment, but using different colors for different surplus energy intervals to preserve the additional information. By choosing four different 5 eV intervals, the following plots in figure 5.23 on the next page can be obtained. The top plot in figure 5.23 on the facing page shows that the used parameters are not suitable for neutrino mass measurements with TFToF spectroscopy. This is due to the fact that electrons with high surplus energies do not get focused and the resulting histogram is rather flat. For lower surplus energies the peaks appear at different positions and hence have a distinct influence on the summed spectrum. Because the neutrino mass impact is highest near the endpoint, such a setting is not usable to extract neutrino mass information. In the bottom plot on the other hand there is a recognizable peak for $15 - 20\,\mathrm{eV}$ surplus energy electrons. While the height of the peak is smaller than the other ones due to lower statistics, it is located in a region of a low total count rate. For lower surplus energies the peaks are positioned at later arrival times and the tail towards higher time-of-flights drops down to low counts at the position of the high-energy peak. For the summed spectrum measured with the detector this means that the high-energy electrons have a noticeable impact upon the structure of the histogram. The contribution of the high surplus energy electrons is about 25% at the peak location. Apart from the parameters used for the bottom plot in figure 5.23 on the next page good results are obtained for $f = 150\,\mathrm{kHz}$ and $U_{\mathrm{pp}} = 50\,\mathrm{V}$ with the additional $+5\,\mathrm{V}$ offset, as well as for $f = 100\,\mathrm{kHz}$ and $U_{\mathrm{pp}} = 100\,\mathrm{V}$. The corresponding histograms can be found in section A.7.

In order to compare the third spectrometer option to the split main spectrometer, the waveform is scanned for different start times and pitch angles like in section 5.2, resulting in a plot with a completely flat region. Comparing figure 5.24 on page 68 to figure 5.20 on page 61 shows that the third spectrometer yields much better results, since such time-focusing could not be achieved with the split spectrometer.

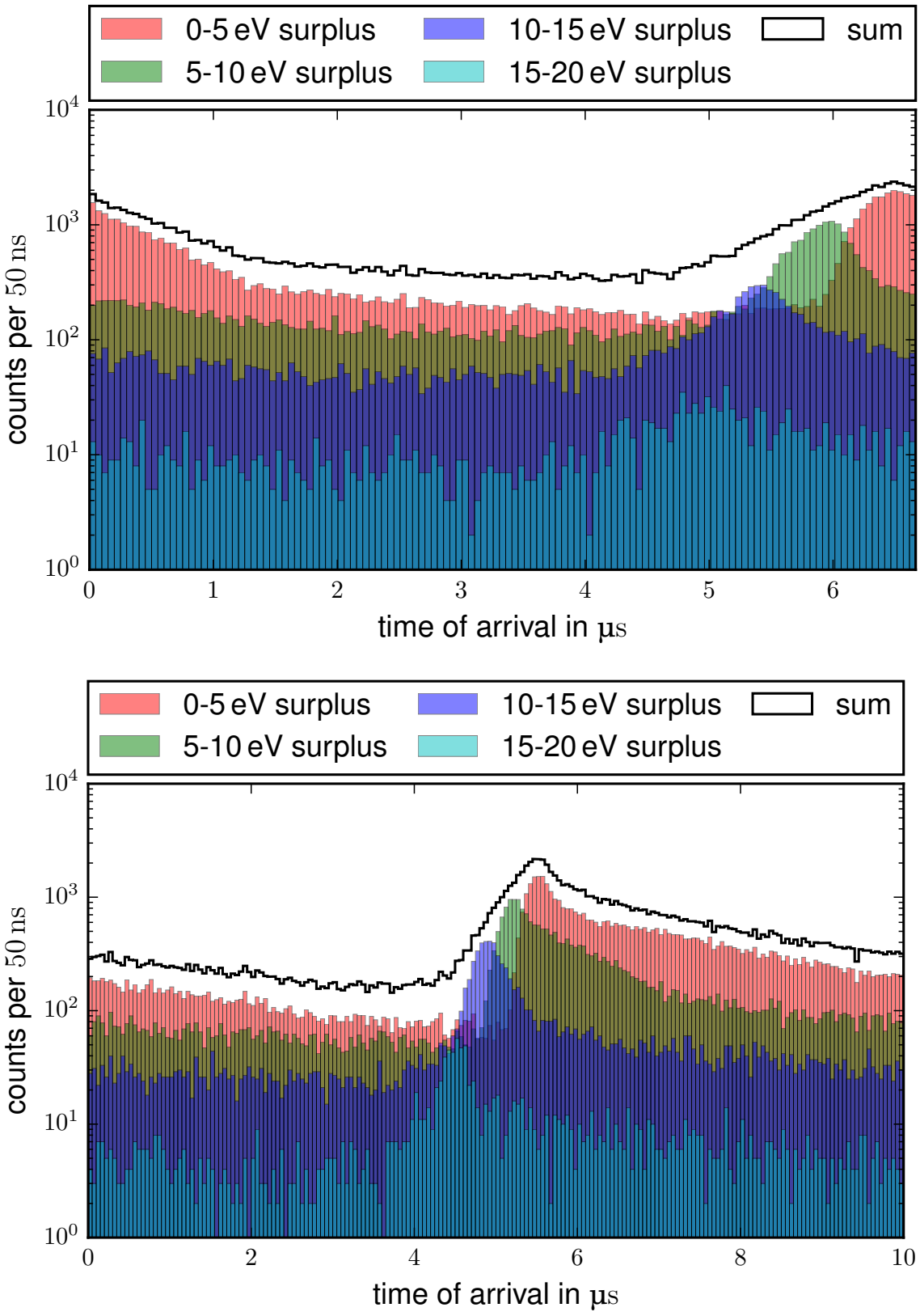


**Figure 5.23.** – **Arrival time histograms with color coded surplus energy for different parameters:** While for $f = 150\,\mathrm{kHz}$ and $U_{\mathrm{pp}} = 25\,\mathrm{V}$ (top) electrons with the highest surplus energies are not significantly focused, the bottom plot shows that for $f = 100\,\mathrm{kHz}$ and $U_{\mathrm{pp}} = 50\,\mathrm{V}$ a focusing occurs. The bin size is 50 ns for both histograms.

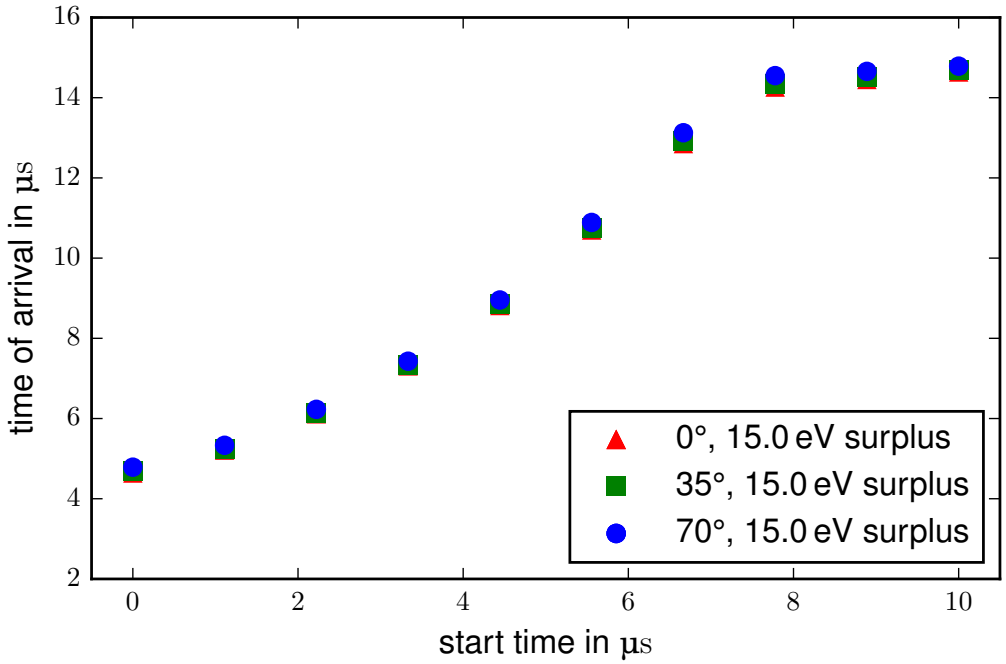


**Figure 5.24. – Arrival time depending on the start time for a dedicated TFToF spectrometer:** Shown here is the time-focusing achieved with the third spectrometer and the parameters $f = 100\,\mathrm{kHz}$ and $U_{\mathrm{pp}} = 50\,\mathrm{V}$. There is no big variation between the different angles due to the high surplus energy of 15 eV and it can be seen that the last three data points are nearly on a straight flat line.

In summary, it can be stated that a third spectrometer indeed represents an option to achieve time-of-arrival focusing, but choosing the right parameters for the potential modulating waveform is crucial to the success. It has been discussed that there exists an upper limit for both frequency and amplitude and in the limited parameter space different combinations have been found to result in good time-of-arrival focusing. However, the analysis done here is solely qualitative and a finer parameter scan near the discovered suitable values should be carried out to further improve the time-focusing effect. Furthermore, it is not clear, if it is feasible to analyze the last 20 eV at once, or if it is better to chose a retarding voltage closer to the endpoint in order to improve the time-focusing capability in the important region of a few eV below the endpoint. A method to gain quantitative information about the neutrino mass sensitivity achievable with TFToF spectroscopy is developed and presented in the next chapter.

# 6. Sensitivity Analysis of the Third Spectrometer

In order to be able to set a limit on the neutrino mass, its influence on the resulting time-of-arrival spectrum has to be extracted. In the case of static potentials the electron time-of-flight can be expressed as a function of the kinetic energy $E$ and the pitch angle $\theta$. The ToF spectrum can then be calculated by taking into account the energy and angular distribution as well as the energy loss inside the tritium source [Ste+13]. Since the energy distribution depends on $m^2(\nu_e)$, the resulting spectrum is also neutrino-mass-dependent. In the case of dynamic potentials these calculations cannot be carried out easily, because the field values are time-dependent. Therefore, simulations are used to obtain a model that can be fitted to measured data.

The waveform parameters are chosen to be $f = 100\,\mathrm{kHz}$ and $U_{\mathrm{pp}} = 50\,\mathrm{V}$, since these have been determined as the most promising in section 5.3. Discretization of the initial energy, the initial pitch angle and the starting time enables the creation of a matrix, where for every entry the simulated flight time is stored. Kassiopeia is used to simulate electrons with energies from $E_{\mathrm{kin}} = qU_{0,\mathrm{main}} = 18555.0\,\mathrm{eV}$ up to $E_{\mathrm{kin}} = 18577.0\,\mathrm{eV}$ in $0.2\,\mathrm{eV}$ steps with angles from $\theta = 0.0°$ to $\theta = 60°$ in $0.6°$ steps and 359 different start times from $t_0 = 0\,\mu\mathrm{s}$ to $t_0 = 9.97215\,\mu\mathrm{s}$ in $27.85\,\mathrm{ns}$ steps for each energy and angle. This way, the waveform of the accelerating voltage is scanned in 1° steps. Afterwards, a normalized time-of-arrival histogram with 50 ns bin width is created for each energy and angle setting, containing 359 arrival time values for the individual start times. For every histogram the content of each bin is stored in an output file for further processing with the *Kronos* framework.

Kronos has been developed to simulate time-of-flight methods for KATRIN and provides useful C++ classes to create and parametrize ToF spectra, interpolate between different spectra to obtain a model that can be fitted to data and contains an interface to ROOT's *MINUIT* [MINUIT] fitter. It has been successfully developed for [Ste+13] to obtain the neutrino mass sensitivity of KATRIN in ToF mode. A new application

called *tftof-precalc*[1] has been written to generate time-of-arrival spectra for different neutrino masses and endpoints[2] to serve as grid points for a *Interpolator2D* object from Kronos. This object provides the model used for fitting by interpolating between the grid points via cubic splines. The **T**ime-**o**f-**A**rrival (ToA) spectra are created by randomly generating electron pitch angles according to an isotropic source and energies from a beta spectrum with angle-dependent energy losses and also taking into account final-state distributions. For the resulting values a transmission check is done to ensure that an electron with such an energy and angle passes the main spectrometer. After that, a simple two-dimensional linear interpolation is used to superimpose the spectra for the nearest energies and angles provided by the matrix created from the Kassiopeia simulations. The resulting spectrum is added to the total spectrum and the process is repeated for $N = 10^6$ events, before saving the result to a file. To decrease the required computation time, the program has been run on the **M**ünster **A**nalysis **F**acility (MAF) cluster and utilizes *OpenMP*[3] to calculate the spectra for 29 different endpoint energies in parallel. Further splitting the neutrino mass calculations into two parallel threads leads to a total acceleration factor of 58. The remaining time required to calculate all 841 endpoint-mass combinations amounts to approximately two weeks.

The pre-calculated spectra are read in by another program called *tftof-spectrum*, which normalizes them to the expected count rate per second and adds an isochronous background of $b = 10\,\mathrm{mHz}$. The resulting spectra are then added to an instance of an Interpolator2D object. The application uses a self-consistent approach by first utilizing the *DataSpectrumPoissonScaled* class to generate a data spectrum from the model and a set measuring time. This spectrum is then fitted by the *MinuitFitter* using the interpolator as model. For the standard KATRIN measuring time of three years the fit result can be found in figure 6.1 on the facing page. The shown $1\sigma$ uncertainties are results of a *MINOS* error analysis, which usually is very exact and takes into account both parameter correlations and non-linearities [MINUIT]. The errors returned by MINOS are indicating the values at which the minimal $\chi^2$ is increased by one ($\chi_0^2 + 1$).

Although all parameters used for the data generation are in the uncertainty intervals returned from the fit routine and $\chi^2$/d.o.f. is close to one, the neutrino mass and endpoint energy uncertainties given by the fit are too small to be realistic. The standard KATRIN uncertainty on $m^2(\nu_\mathrm{e})$ is $\sigma_\mathrm{stat,standard} = 0.020\,\mathrm{eV}^2$ [Kat04] and therefore three orders of magnitude larger than the one produced by the fit. A plot of $\chi^2$ versus $m^2(\nu_\mathrm{e})$ for a different fit with the same parameters can be found in section A.9.

[1] For the source code of the newly written programs see [Kronos-git].
[2] The used values can be found in table A.1 in section A.8
[3] OpenMP is an API that supports multiprocessing by using compiler directives. For more information see [OpenMP].

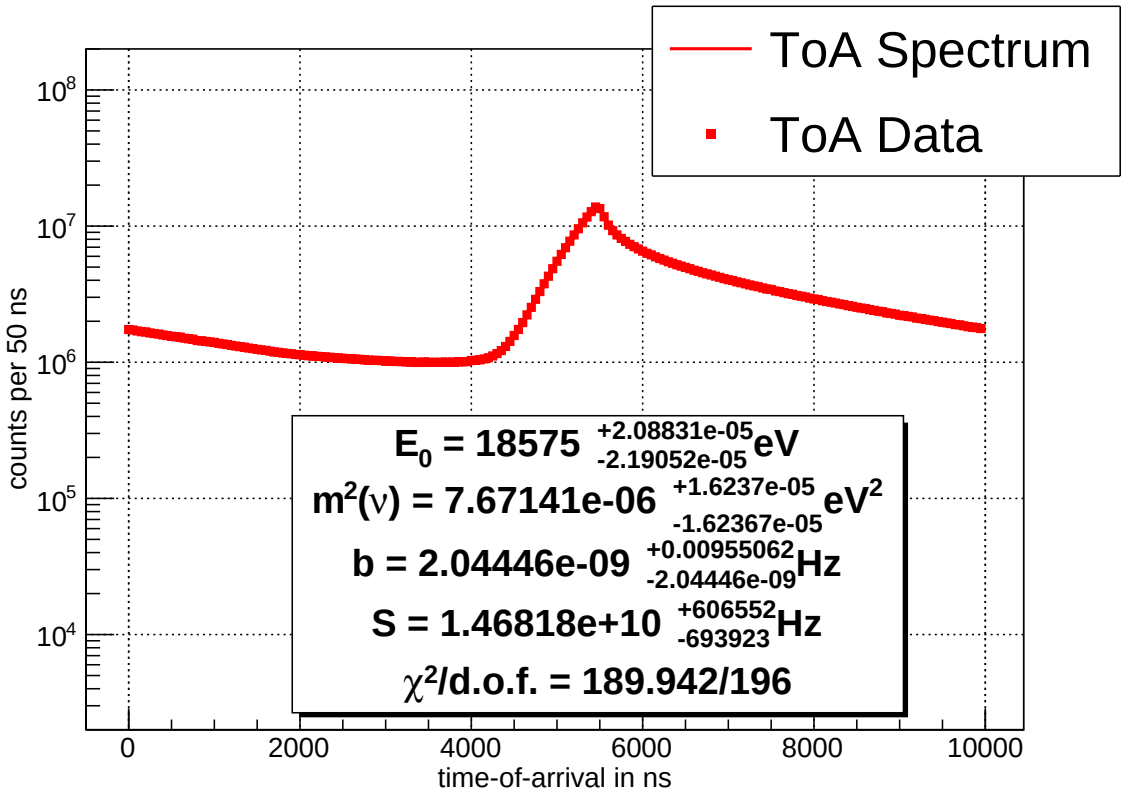


**Figure 6.1. – Time-of-arrive spectrum fit for three years of measuring time:** For the data generation a neutrino mass of $m(\nu_e) = 0\,\text{eV}$ and an endpoint energy of $E_0 = 18575.0\,\text{eV}$ have been assumed and both values are correctly found by the fit, but with an extremely low uncertainty. Besides the already mentioned parameters $E_0$ and $m^2(\nu_e)$, the background rate $b$ and the signal rate $S$ are fitted. The signal rate represents the number of electrons per second getting detected if the retarding potential is zero. The background rate shows very asymmetric errors, because the parameter has been limited to the interval $[0\,\text{Hz}, 1\,\text{Hz}]$.

At first glance the obtained data spectrum resembles the one produced by the Kassiopeia simulation shown at the bottom of figure 5.23 on page 67. Taking a closer look at two pre-calculated spectra at neighboring interpolation grid points (see figure 6.2 on the following page) reveals that in the region with the lowest count rate the model shows strong variations from bin to bin. This indicates insufficient statistics during the calculation done with Kassiopeia, since the variation is the same for different neutrino masses. A finer discretization of the electron energy, the pitch angle and especially the start time should smoothen the obtained model. Because the Kassiopeia simulations have to be done before the time-consuming pre-calculations with Kronos, they could not be repeated for this thesis. The problem may also be related to the random number generation used during pre-calculation with Kronos in combination with parallelization. Using the same random numbers for pre-calculation of different grid points would also result in the effect seen in figure 6.2. Although a quick test did not reveal issues of ROOT's *TRandom3* under multi-thread conditions, an extended testing has

not been carried out.

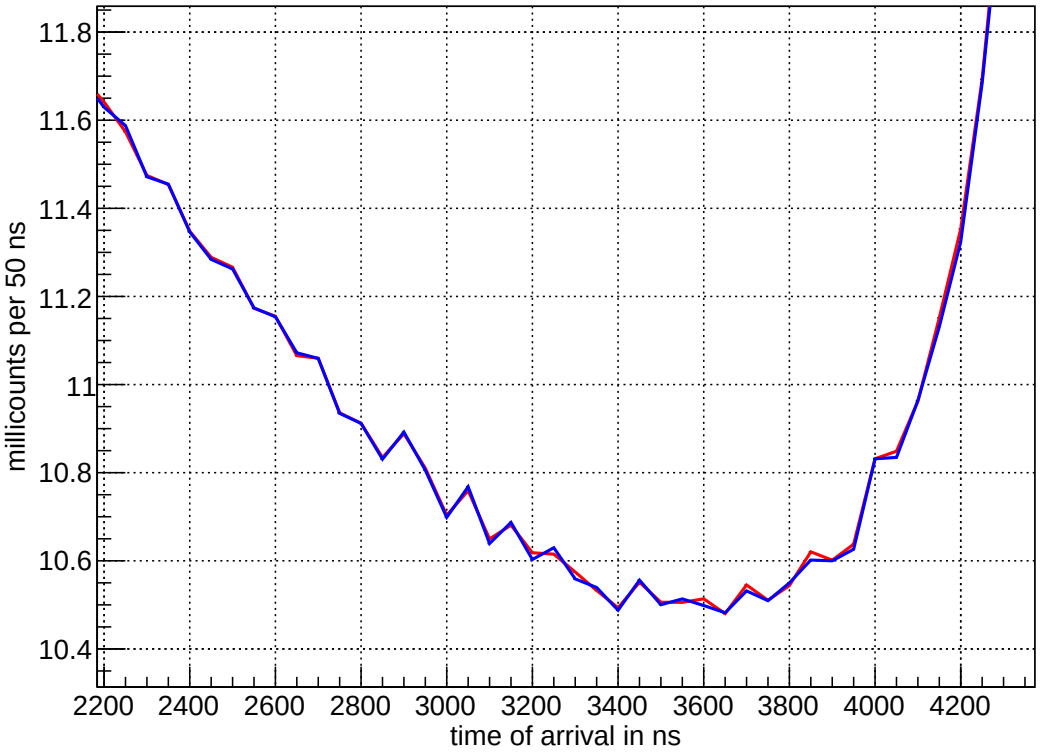


**Figure 6.2. – Low count rate region of the pre-calculated spectra for $E_0 = 18575\,\mathrm{eV}$ with $m^2(\nu_e) = 0\,\mathrm{eV}^2$ (red) and $m^2(\nu_e) = 0.25\,\mathrm{eV}^2$ (blue):** Both spectra show the same strong variation from bin to bin. In this region, the difference between the spectra is not very pronounced.

Since all spectra show the same consistent behavior in this region, it does not explain the small uncertainties in the fit. However, plotting the difference between the two pre-calculated spectra for $E_0 = 18575.0, m^2(\nu_e) = 0.0$ and $E_0 = 18575.0, m^2(\nu_e) = 0.0005$ also gives a very coarse graph, as shown in figure 6.3 on the next page. It is expected that the biggest difference can be seen at arrival times around 4 µs to 5 µs, because this is the region where most of the high energetic electrons arrive, as can be seen in the bottom plot of figure 5.23 on page 67.

While this expectation is confirmed by the plot, the difference still shows large random or pseudo-random variations in this region. The fluctuations caused by low statistics dominate the difference between two spectra for most of the bins. Because the data spectrum is generated from the model for a certain neutrino mass, it inherits the random structure. Fitting of the data spectrum then yields very low uncertainties, because the fit is sensitive to these random variations, which are only accurately matched by the spectrum used to generate the data.

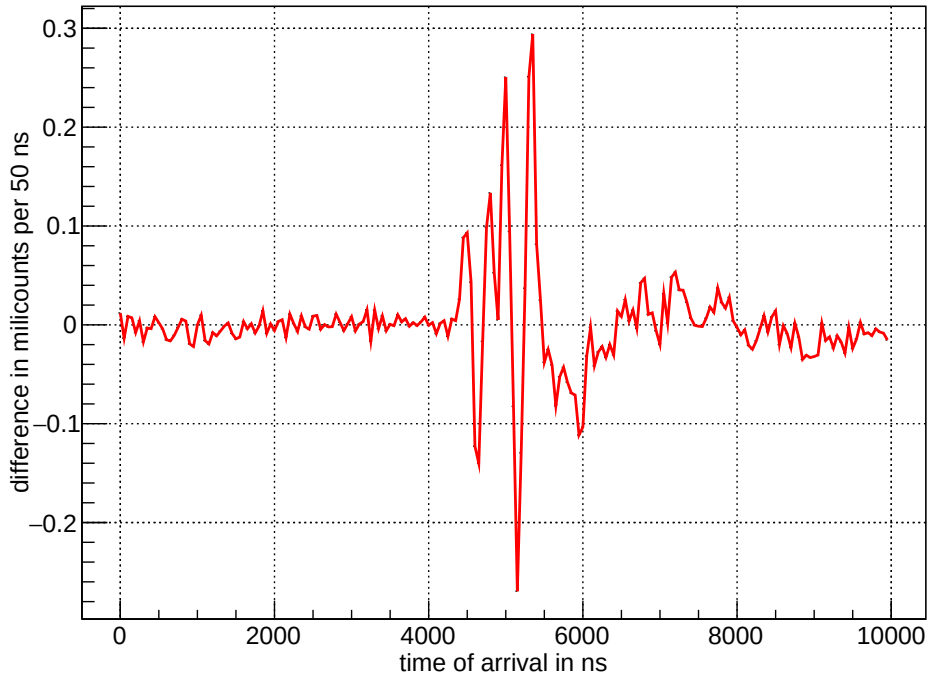


**Figure 6.3. – Difference between the spectra for $E_0 = 18575\,\mathrm{eV}$ with $m^2(\nu_e) = 0\,\mathrm{eV}^2$ and $m^2(\nu_e) = 0.0005\,\mathrm{eV}^2$:** For most arrival times the difference is dominated by low statistics noise.

A tighter spacing between the neutrino mass values used for pre-calculation amplifies this problem. The model used for fitting is obtained by an interpolator and it changes faster with neutrino mass the smaller the mass difference between two adjacent spectra is. If the statistics of the model spectra are sufficient, the difference between two spectra also decreases with the distance between those spectra. This is not true if the difference is dominated by random effects. A larger distance between the neutrino mass grid points should reduce the sensitivity to random variations. Using only the values $m^2(\nu_e) = -0.25\,\mathrm{eV}^2$, $m^2(\nu_e) = 0.0\,\mathrm{eV}^2$ and $m^2(\nu_e) = +0.25\,\mathrm{eV}^2$ indeed increases the uncertainty significantly, as shown in figure 6.4 on the next page.

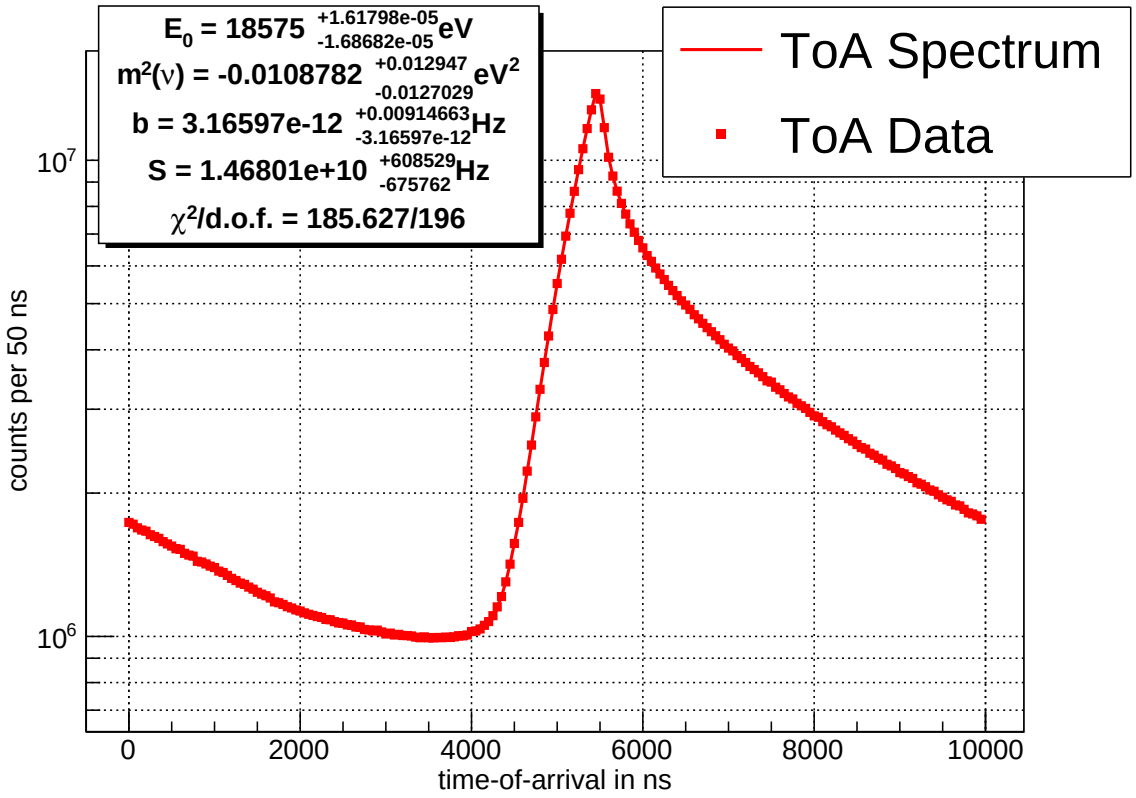


**Figure 6.4. – Time-of-arrival spectrum fit for three years of measuring time and only three neutrino mass grid points:** The obtained uncertainty on the neutrino mass is three orders of magnitude larger than in figure 6.1 on page 71. The endpoint uncertainty is still on the same scale, because their spacing has not been modified.

This confirms that the insufficient statistics combined with the tight spacing of the masses used for pre-calculation is responsible for the unrealistic small uncertainty estimated by the fit. The obtainable sensitivity cannot be concluded from figure 6.4, because using only three wide apart input spectra for the cubic spline interpolation does not result in the correct $m^2(\nu_e)$ dependency of the model. Although diminished, the low statistics still have an impact on the estimated uncertainty.

A further reason of the low uncertainties estimated by the fits above is the high number of events in the data spectrum of around $N = 5.8 \cdot 10^8$ compared to only $10^6$ events used during pre-calculation. Because of this, the fit is overly sensitive to random fluctuations of the underlying model. However, even reducing the number of events in the data spectrum down to $N = 10^5$ only increases the obtained uncertainties by an order of magnitude, as can be seen in figure 6.5 on the next page.

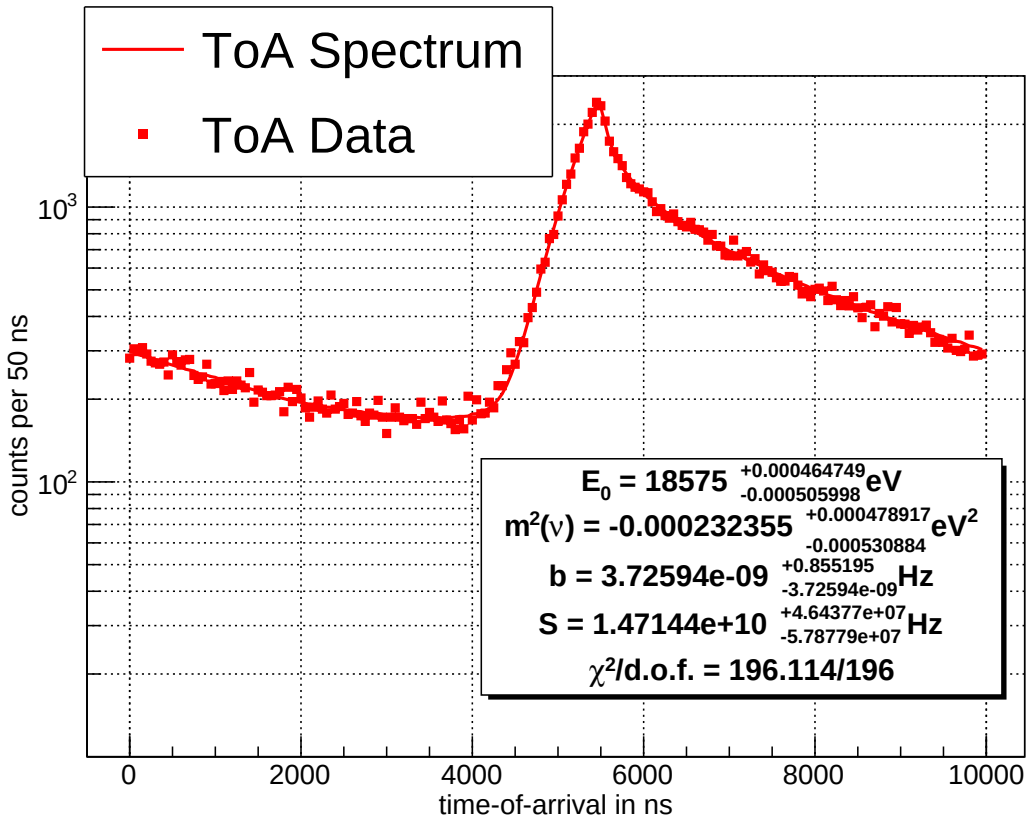


**Figure 6.5. – Time-of-arrival spectrum fit for $10^5$ events:** The obtained uncertainty on the neutrino mass is still unrealistically low, indicating that the fit is still overly sensitive to (pseudo-)random variations in the model.

To estimate the achievable sensitivity, the fluctuations[4] of $\chi^2$ between the spectra of two grid values $m^2(\nu_e)$ due to the influence of randomness have to be decreased down to $\Delta\chi^2_{\text{fluct}} \ll 1$. This is necessary to be able to make out an increase of one in $\chi^2$, which indicates the $1\sigma$ uncertainties. Decreasing the number of events in the data spectrum to $N_{\text{reduced}}$ also decreases the aforementioned fluctuations. A value for the reachable uncertainty after the full measurement time can then be estimated by scaling the uncertainty $\sigma_{\text{stat,reduced}}$ for the reduced number of events $N_{\text{reduced}}$, assuming a square root dependence on the event number:

$$\sigma_{\text{stat,full}} \approx \sigma_{\text{stat,reduced}} \cdot \sqrt{\frac{N_{\text{reduced}}}{N_{\text{full}}}} \,. \tag{6.1}$$

With the available pre-calculated data, the number of events in the data spectrum has to be cut down to $N_{\text{reduced}} \leq 2.5 \cdot 10^4$ in order to ensure $\Delta\chi^2_{\text{fluct}} < 1$, as shown in figure 6.6 on the next page.

[4] A plot showing these fluctuation for $N = 10^6$ can be found in figure A.6 on page A26.

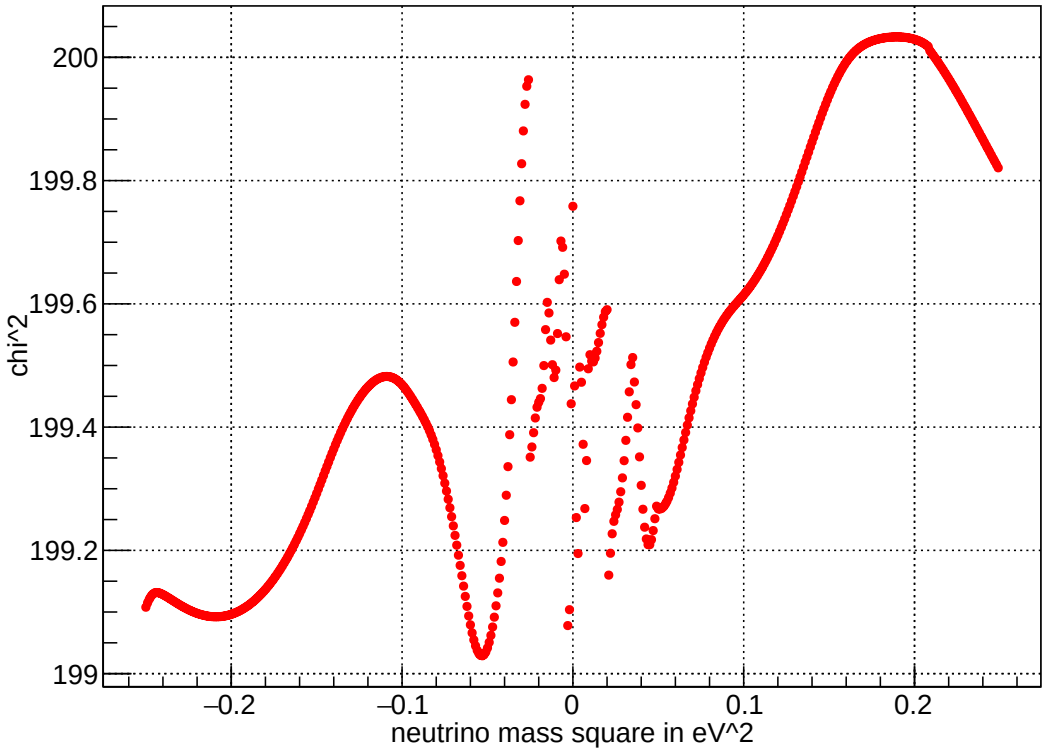


**Figure 6.6.** – $\chi^2$ **behavior over the simulated** $\mathbf{m^2(\nu_e)}$ **region for** $\mathbf{N = 2.5 \cdot 10^4}$ **events:** The fluctuations visible around $m^2(\nu_e) = 0$ do not exceed a peak-to-peak value of one.

Together with the expected signal rate of $S = 6.176\,\mathrm{Hz}$ for the last 20 eV below the endpoint, this value of $N_{\mathrm{reduced}}$ corresponds to a measurement time of only

$$t_{\mathrm{meas}} = \frac{N_{\mathrm{reduced}}}{S} = 4048\,\mathrm{s} \approx 1.12\,\mathrm{h}\,, \tag{6.2}$$

for which the standard KATRIN sensitivity amounts to

$$\sigma^{\mathrm{standard}}_{\mathrm{stat,reduced}} = \sigma^{\mathrm{standard}}_{\mathrm{stat,full}}\,\mathrm{eV}^2 \cdot \sqrt{\frac{24 \cdot 365 \cdot 3\,\mathrm{h}}{1.12\,\mathrm{h}}} \approx 3.06\,\mathrm{eV}^2 \tag{6.3}$$

Under the realistic assumption that a TFToF section can improve the sensitivity on $m^2(\nu_e)$ by a factor of 4, the $\chi^2$ curve should be increased by one at

$$\Delta m^2(\nu_e) = \frac{3.06\,\mathrm{eV}^2}{4} = 0.765\,\mathrm{eV}^2\,. \tag{6.4}$$

However, because the maximal available difference in $\Delta m^2(\nu_e)$ for the pre-calculated spectra only amounts to $0.5\,\mathrm{eV}^2$, it cannot be tested if this expectancy is confirmed. Additionally, the fluctuations in figure 6.6 are still rather large and may conceal a possible increase in $\chi^2$.

The above analysis leads to the conclusion that the impact of an additional TFToF section on the neutrino mass sensitivity of KATRIN cannot be obtained with the statistics available in this thesis. Computing grid points for a larger $m^2(\nu_e)$ region can be used to investigate the achievable sensitivity with the calculations presented here. However, since they rely on estimations and assumptions, they are only able to predict the scale of $\sigma^{\mathrm{tftof}}_{\mathrm{stat,full}}$. Rerunning the pre-calculations with a significant increase in statistics seems unavoidable to obtain the real sensitivity improvement of the TFToF section. An optimization of spacing between neutrino masses used as grid points could help to reduce the necessary computation time. Alternatively, a different strategy, like importance sampling for example, has to be used to improve the sensitivity estimation. It is advisable to use Kassiopeia for a finer parameter scan on $f$ and $U_{pp}$ of the accelerating voltage, prior to the Kronos pre-calculation, to avoid repetition of the time consuming pre-calculations as much as possible.

For the investigations above, an isochronous background has been assumed, which is not entirely correct. While the background is indeed isochronously distributed at the end of the main spectrometer, background electrons are also affected by the accelerating voltage in the TFToF section. Hence, they are time-focused as well. This may help to discriminate background if it does not follow a uniform energy distribution. Simulation of these background electrons should be added to the pre-calculation program in the future to get a better estimate on the achievable neutrino mass sensitivity.

# 7. Summary

In its standard operation mode KATRIN aims to reach a sensitivity on the neutrino mass of 0.2 eV at 90% C.L. by analyzing the endpoint region of the tritium $\beta$-decay, thus improving the currently best model-independent upper limit by an order of magnitude. From the source to the detector, the KATRIN experiment consists of several subsystems, each playing an important part in contributing to the final sensitivity.

The main spectrometer represents the major tool for the energy analysis of $\beta$-electrons and is based on the MAC-E filter technique. While in the standard mode the voltages applied to the electrode system are constant, there also exists the possibility to use a time-dependent electric potential in order to accelerate electrons depending on the time they enter the main spectrometer. This allows for a start signal to be obtained for time-of-flight analysis, providing energy information about detected electrons. The main goal of (TF)ToF methods is to use the additional energy information of the electrons to effectively measure the differential $\beta$-spectrum instead of the integrated spectrum in the standard mode.

During part of the SDS 2 measurement phase the main spectrometer has been configured in a split mode, where the analyzing plane is shifted towards the source and the downstream part is used as acceleration and delay line. The e-gun has been used to perform tests of the time-focusing capabilities of such a setup. Although the measurements took place over a year before this thesis, Kassiopeia was not capable of carrying out the simulations necessary to understand the data. Therefore an additional class has been written and tested during this thesis, which implements ramping between different potential settings with several functions in Kassiopeia.

The conducted analysis of the SDS 2 data exposed inconsistencies between the first measurement run and others, where the start times of the electrons were phase shifted. The trigger of the e-gun laser seems responsible for an unwanted additional start time offset and a decreased number of produced electrons. For the first measurement the results essentially agree with the simulations and show that a start-time-dependence of the time-of-flight is achievable with the split main spectrometer. However, further

investigations on the frequency and amplitude influence on the time-of-arrival focusing led to the conclusion that there are no parameters suitable for neutrino mass measurements. The short delay line and the weak electric field in the spectrometer have been identified as the main problems by comparing electrons traveling on the central axis with ones closer to the electrode system of the spectrometer. Together with the amplitude and frequency limitations, the simulations prove the split spectrometer setup unfit for neutrino mass measurements with TFToF spectroscopy.

To overcome these problems, the option of a third spectrometer as a dedicated TFToF section has been examined. Although it is unlikely that such a spectrometer will be implemented at KATRIN in the near future, it has been shown that an energy-dependent time-of-arrival focusing can be realized with this setup. The required frequencies and amplitudes are on a scale that allow a technical realization.

In order to estimate how much KATRIN's neutrino mass sensitivity would benefit from the additional TFToF section, the Kronos framework has been utilized. Unfortunately, the available computation time restricted these investigations to a single frequency and amplitude setting with low statistics. The impact on the neutrino mass sensitivity could not be recovered precisely. Nevertheless, the programs written for the sensitivity analysis are functional in principle. With additional computation time and optimized strategies it should be possible to obtain a result in the near future.

While in this thesis the tools for time-focusing-time-of-flight methods have been developed and tested, a conclusive analysis requires more time and effort. From geometry optimizations for the additional spectrometer to a finer parameter scan, various possibilities exist to improve the possible beneficial effects of a TFToF section. The third spectrometer may represent an interesting future upgrade to KATRIN.

# A. Appendix

## A.1. Implementation of Time-Dependent Fields

Here, only the source code of the main file is shown. For the complete code including headers and bindings can be found at [Kasper-git]

Kassiopeia/Fields/Source/KSFieldElectricRamped2Fields.cxx

```
#include "KSFieldElectricRamped2Fields.h"
#include "KSToolbox.h"
#include "KSFieldElectromagnet.h"
#include "KThreeVector.hh"
using KGeoBag::KThreeVector;
namespace Kassiopeia
{
    KSFieldElectricRamped2Fields::KSFieldElectricRamped2Fields() :
        fRootElectricField1( NULL ),
        fRootElectricField2( NULL ),
        fRootElectricFieldName1( "" ),
        fRootElectricFieldName2( "" ),
        fRampingType( rtExponential ),
        fNumCycles( 1 ),
        fRampUpDelay( 0. ),
        fRampDownDelay( 0. ),
        fRampUpTime( 0. ),
        fRampDownTime( 0. ),
        fTimeConstant( 0. ),
        fTimeScalingFactor( 1. )
    {
    }
    KSFieldElectricRamped2Fields::KSFieldElectricRamped2Fields( const
       KSFieldElectricRamped2Fields& aCopy ) :
        Kassiopeia::KSComponent(),
        fRootElectricField1( aCopy.fRootElectricField1 ),
        fRootElectricField2( aCopy.fRootElectricField2 ),
        fRootElectricFieldName1( aCopy.fRootElectricFieldName1 ),
        fRootElectricFieldName2( aCopy.fRootElectricFieldName2 ),
```

```
29          fRampingType( aCopy.fRampingType ),
30          fNumCycles( aCopy.fNumCycles ),
31          fRampUpDelay( aCopy.fRampUpDelay ),
32          fRampDownDelay( aCopy.fRampDownDelay ),
33          fRampUpTime( aCopy.fRampUpTime ),
34          fRampDownTime( aCopy.fRampDownTime ),
35          fTimeConstant( aCopy.fTimeConstant ),
36          fTimeScalingFactor( aCopy.fTimeScalingFactor )
37      {
38      }
39      KSFieldElectricRamped2Fields* KSFieldElectricRamped2Fields::Clone
            () const
40      {
41          return new KSFieldElectricRamped2Fields( *this );
42      }
43      KSFieldElectricRamped2Fields::~KSFieldElectricRamped2Fields()
44      {
45      }
46      void KSFieldElectricRamped2Fields::CalculatePotential( const
            KThreeVector &aSamplePoint, const double &aSampleTime, double
            &aTarget )
47      {
48          fRootElectricField1->CalculatePotential( aSamplePoint,
                aSampleTime, aTarget );
49          double tempTarget = aTarget;
50          fRootElectricField2->CalculatePotential( aSamplePoint,
                aSampleTime, aTarget );
51
52          double Modulation = GetModulationFactor( aSampleTime );
53          aTarget = (1 - Modulation) * tempTarget + Modulation * aTarget
                ;
54          fieldmsg_debug( "Ramped electric field <" << GetName() << ">
                returns U=" << aTarget << " at t=" << aSampleTime << eom )
                ;
55      }
56      void KSFieldElectricRamped2Fields::CalculateField( const
            KThreeVector &aSamplePoint, const double &aSampleTime,
            KThreeVector &aTarget )
57      {
58          fRootElectricField1->CalculateField( aSamplePoint, aSampleTime
                , aTarget );
59          KThreeVector tempTarget = aTarget;
60          fRootElectricField2->CalculateField( aSamplePoint, aSampleTime
                , aTarget );
61
62          double Modulation = GetModulationFactor( aSampleTime );
```

```
63          aTarget = (1 - Modulation) * tempTarget + Modulation * aTarget
                ;
64          fieldmsg_debug( "Ramped electric field <" << GetName() << ">
                returns E=" << aTarget << " at t=" << aSampleTime << eom )
                ;
65      }
66      double KSFieldElectricRamped2Fields::GetModulationFactor( const
            double &aTime )
67      {
68          double tLength = fRampUpDelay + fRampUpTime + fRampDownDelay +
                fRampDownTime;
69
70          double tTime = aTime;
71          int tCycle = (int)floor( tTime / tLength );
72          if ( tCycle < fNumCycles )
73              tTime -= tCycle * tLength;
74          tTime *= fTimeScalingFactor;
75
76          double tUp    =          fRampUpDelay    * fTimeScalingFactor;
77          double tHigh = tUp    + fRampUpTime     * fTimeScalingFactor;
78          double tDown = tHigh + fRampDownDelay * fTimeScalingFactor;
79          double tLow  = tDown + fRampDownTime  * fTimeScalingFactor;
80          double tOmega = 2.*M_PI/tLength;
81
82          double Field = 0.;
83          switch( fRampingType )
84          {
85              case rtLinear :
86                  if (tTime >= tLow)
87                      Field = 0.;
88                  else if (tTime >= tDown)
89                      Field = (1. - ((tTime - tDown) / fRampDownTime));
90                  else if (tTime >= tHigh)
91                      Field = 1.;
92                  else if (tTime >= tUp)
93                      Field = ((tTime - tUp) / fRampUpTime);
94                  break;
95
96              case rtExponential :
97                  if (tTime >= tLow)
98                      Field = 0.;
99                  else if (tTime >= tDown)
100                 {
101                     Field = exp( -(tTime - tDown) / fTimeConstant );
102                 }
103                 else if (tTime >= tHigh)
104                     Field = 1.;
```

```
105                 else if (tTime >= tUp)
106                     Field = 1. - exp( -(tTime - tUp) / fTimeConstant )
                            ;
107                 break;
108
109             case rtSinus :
110                 if (tTime >= tUp)
111                     Field = 0.5 + 0.5 * sin(tTime * tOmega);
112                 break;
113
114             case rtSquare :
115                 if (tTime >= tDown)
116                     Field = 0.;
117                 else if (tTime >= tUp)
118                     Field = 1.;
119                 break;
120
121             default :
122                 fieldmsg( eError ) << "Specified ramping type is not
                        implemented" << eom;
123                 break;
124         }
125         fieldmsg_debug( "Ramped electric field <" << GetName() << ">
                uses modulation factor " << Field << " at t=" << tTime <<
                eom );
126         return Field;
127     }
128     void KSFieldElectricRamped2Fields::InitializeComponent()
129     {
130         fieldmsg_debug( "Initializing first root electric field <" <<
                fRootElectricFieldName1 << "> from ramped electric field <
                " << GetName() << ">" << eom );
131         fieldmsg_debug( "Initializing second root electric field <" <<
                 fRootElectricFieldName2 << "> from ramped electric field
                <" << GetName() << ">" << eom );
132         fRootElectricField1 = KSToolbox::GetInstance()->GetObjectAs<
                KSElectricField >( fRootElectricFieldName1 );
133         fRootElectricField2 = KSToolbox::GetInstance()->GetObjectAs<
                KSElectricField >( fRootElectricFieldName2 );
134         if (! fRootElectricField1)
135         {
136             fieldmsg( eError ) << "Ramped electric field <" << GetName
                    () << "> can't find root electric field <" <<
                    fRootElectricFieldName1 << ">!" << eom;
137         }
138         if (! fRootElectricField2)
139         {
```

```
140             fieldmsg( eError ) << "Ramped electric field <" << GetName
                    () << "> can't find root electric field <" <<
                    fRootElectricFieldName2 << ">!" << eom;
141         }
142
143         fieldmsg_assert( fNumCycles, > 0 )
144         fieldmsg_assert( fTimeScalingFactor, > 0. )
145         fieldmsg_assert( fRampUpTime, >= 0. )
146         fieldmsg_assert( fRampUpDelay, >= 0. )
147         fieldmsg_assert( fRampDownTime, >= 0. )
148         fieldmsg_assert( fRampDownDelay, >= 0. )
149         if ( fRampingType == rtExponential )
150         {
151             fieldmsg_assert( fTimeConstant, > 0. )
152         }
153
154         fRootElectricField1->Initialize();
155         fRootElectricField2->Initialize();
156     }
157     void KSFieldElectricRamped2Fields::DeinitializeComponent()
158     {
159         fRootElectricField1->Deinitialize();
160         fRootElectricField1->Deinitialize();
161     }
162 }
```

## A.2. Example Kassiopeia XML File for Time-Varying Fields

oscillating-2fields.xml (partial)

```
<!-- XML simple test config for the ramped electric field -->
<!-- Authors: A. Fulst -->

<external_define name="start_time" value="5.e-6"/>
<external_define name="period" value="10.e-6"/>
<external_define name="type" value="sinus"/>
<external_define name="timeconstant" value="1."/>
<external_define name="cycles" value="1"/>

<kassiopeia>
    <!-- electric fields -->
    <ksfield_electrostatic
        name="field_electrostatic_one"
        file="oscillating_one.kbd"
        system="world/dipole_trap"
        surfaces="world/dipole_trap/@electrode_tag"
        symmetry="axial"
    >
        <cached_bem_solver
            hash="e998fa94a2c72acb11cf490f46f15d00"
        />
        <zonal_harmonic_field_solver
            number_of_bifurcations="-1"
            convergence_ratio=".99"
            convergence_parameter="1.e-15"
            proximity_to_sourcepoint="1.e-12"
            number_of_central_coefficients="500"
            use_fractional_central_sourcepoint_spacing="false"
            central_sourcepoint_spacing="1.e-3"
            number_of_remote_coefficients="200"
        />
    </ksfield_electrostatic>

    <ksfield_electrostatic
        name="field_electrostatic_two"
        file="oscillating_two.kbd"
        system="world/dipole_trap"
        surfaces="world/dipole_trap/@electrode_tag"
        symmetry="axial"
    >
        <cached_bem_solver
```

```
            hash="cc9fdf1721580ea67a58528ebdfde426"
        />
        <zonal_harmonic_field_solver
            number_of_bifurcations="-1"
            convergence_ratio=".99"
            convergence_parameter="1.e-15"
            proximity_to_sourcepoint="1.e-12"
            number_of_central_coefficients="500"
            use_fractional_central_sourcepoint_spacing="false"
            central_sourcepoint_spacing="1.e-3"
            number_of_remote_coefficients="200"
        />
    </ksfield_electrostatic>

    <ksfield_electric_ramped_2fields
        name="field_ramped"
        root_field_1="field_electrostatic_one"
        root_field_2="field_electrostatic_two"
        ramping_type="[type]"
        num_cycles="[cycles]"
        ramp_up_time="{[period]/2}"
        ramp_down_time="{[period]/2}"
        time_constant="[timeconstant]"
    />
</kassiopeia>
```

## A.3. SDS-ToF BEANS Program

The source code for the modified *BEANS* program can be found below:

sds-tof.cxx

```
// sds-tof.cxx //

#include <TSpectrum.h>
#include <KDBeans.h>

using namespace std;
using namespace katrin;

// E-Gun pulse interval: can be changed later by program arguments //
static Double_t pulseInterval = 1e-3;
static Double_t latency = 1270e-9;

// Method 1: First-Peak + Cycle-Correction method //
// This Tof() returns the first peak times,
// which are later corrected by CycleCorrection() below.
pair<Double_t, Double_t> Tof1(TH1* h)
{
    TSpectrum spectrum;
    spectrum.Search(h, 2, "", 0.5);
    Int_t n = spectrum.GetNPeaks();
    Float_t* x = spectrum.GetPositionX();

    Double_t peakPosition = 3 * pulseInterval;
    for (Int_t i = 0; i < n; i++) {
        if ((x[i] > pulseInterval/2) && (x[i] < peakPosition)) {
            peakPosition = x[i];
        }
    }
    if (peakPosition > 2*pulseInterval) {
        return make_pair(-1, -1);
    }
    Double_t fitRangeLeft = peakPosition - 0.4*pulseInterval;
    Double_t fitRangeRight = peakPosition + 0.4*pulseInterval;

    h->Fit("gaus", "Q", "", fitRangeLeft, fitRangeRight);
    TF1* fitFunction = h->GetFunction("gaus");
    if (! fitFunction) {
        return make_pair(-1, -1);
    }

    Double_t peak = fitFunction->GetParameter(1);
```

```
42      Double_t peakError = fitFunction->GetParError(1);
43      //Double_t width = fitFunction->GetParameter(2);
44      //Double_t widthError = fitFunction->GetParError(2);
45      fitFunction->SetLineColor(kRed);
46
47      return make_pair(peak, peakError);
48  }
49
50  pair<Double_t, Double_t> CycleCorrection1(TGraph* graph)
51  {
52      TGraphErrors* g = dynamic_cast<TGraphErrors*>(graph);
53      if (! g) {
54          return make_pair(-1, -1);
55      }
56
57      g->Sort();
58      Int_t n = g->GetN();
59      Double_t* x0 = g->GetX();
60      Double_t* y0 = g->GetY();
61      Double_t* x0err = g->GetEX();
62      Double_t* y0err = g->GetEY();
63
64      Int_t cycle = 0;
65      vector<Double_t> x(n, 0), y(n, 0), xerr(n, 0), yerr(n, 0);
66      for (Int_t i = n-1; i >= 0; i--) {
67          x[i] = x0[i]; y[i] = y0[i];
68          xerr[i] = x0err[i]; yerr[i] = y0err[i];
69          if (y0err[i] > pulseInterval/2) {
70              continue;
71          }
72          if (i == n-1) {
73              if (y0[i] > pulseInterval/2) {
74                  // assume the first point is at the "closest to zero"
                        cycle.
75                  cycle = - ((Int_t) ((y0[i] + pulseInterval/2) /
                        pulseInterval));
76              }
77          }
78          else if (fabs(y0[i] + pulseInterval - y0[i+1]) < pulseInterval
                /5) {
79              cycle++;
80          }
81          y[i] += cycle * pulseInterval;
82      }
83
84      for (Int_t i = 0; i < n; i++) {
85          g->SetPoint(i, x[i], y[i]);
```

```
86          g->SetPointError(i, xerr[i], yerr[i]);
87      }
88
89      return make_pair(cycle, 0);
90  }
91
92  // Method 2: Auto-Follower method //
93  // Fitting range is determined from previous peak fitting result.
94  // This method works only for "transmission to no-transmission" scan
95  pair<Double_t, Double_t> Tof2(TH1* h)
96  {
97      // Fit range for this sub-run is detemined by previous subrun fit
            result.
98      // In this way it should follow the correct peak position.
99      static Double_t fitRangeLeft = 0;
100     static Double_t fitRangeRight = pulseInterval;
101
102     h->Fit("gaus", "Q", "", fitRangeLeft, fitRangeRight);
103     TF1* fitFunction = h->GetFunction("gaus");
104     if (! fitFunction) {
105         return make_pair(-1, -1);
106     }
107
108     Double_t peak = fitFunction->GetParameter(1);
109     Double_t peakError = fitFunction->GetParError(1);
110     //Double_t width = fitFunction->GetParameter(2);
111     //Double_t widthError = fitFunction->GetParError(2);
112     fitFunction->SetLineColor(kRed);
113
114     // fit range for next sub-run
115     fitRangeLeft = peak - pulseInterval/2;
116     fitRangeRight = peak + pulseInterval/2;
117
118     return make_pair(peak, peakError);
119 }
120
121 pair<Double_t, Double_t> CycleCorrection2(TGraph* g)
122 {
123     // cycle correction is not necessary for the auto-follower method
            //
124     return make_pair<Double_t, Double_t>(0, 0);
125 }
126
127 int main(int argc, char** argv)
128 {
129     KArgumentList args(argc, argv);
130     pulseInterval = args["--pulse-interval"].Or(pulseInterval);
```

```
131
132     // energy selection //
133     Double_t low=0;
134     Double_t high=10e5;
135
136     if (not args["--normal"].IsVoid() ) {
137         low = 15e3;
138         high = 35e3;
139     }
140     else if (not args["--pile-1"].IsVoid()) {
141         low = 45e3;
142         high = 60e3;
143     }
144     else if (not args["--pile-2"].IsVoid()) {
145         low = 65e3;
146         high = 90e3;
147     }
148     else if (not args["--pile-3"].IsVoid()) {
149         low = 95e3;
150         high = 120e3;
151     }
152
153     // method selection //
154     pair<Double_t, Double_t> (*Tof)(TH1*);
155     pair<Double_t, Double_t> (*CycleCorrection)(TGraph*);
156     Int_t maxNumberOfPulseCycles;
157     if (args["--auto-follow"].IsVoid()) {
158         Tof = Tof1;
159         CycleCorrection = CycleCorrection1;
160         maxNumberOfPulseCycles = 1;
161     }
162     else {
163         Tof = Tof2;
164         CycleCorrection = CycleCorrection2;
165         maxNumberOfPulseCycles = 1;
166     }
167
168   stringstream ss;
169   ss << "TimeOfFlight-" << args[0] << ".png";
170   string s = ss.str();
171     KDBeans beans;
172     (beans
173         .Append(new KDEnergyEventReadout())
174         .Append(new KDSubRunLengthTrimming())
175
176         // ROI cut
177         .Append(new KDFpdEnergyCalibration())
```

```
178         .AppendFor<beans::FpdCh>((new KDEnergyRangeSelection())
179             ->SetRange(low, high)
180         )
181 
182         // Tag the reference channel events as "Start" of flight //
183         .Append((new KDChannelGroupTagging())
184             ->SetTagName("Start")
185             ->AddChannelGroup(KDChannel::kRef)
186         )
187 
188         // time since start, taking modulo of 10 us, with cycle
                duplication //
189         .Append((new KDIntervalHistogram())
190             ->SetStartEventTag("Start")
191             ->SetStartLatency(latency)  // correction for DAQ delay
192             ->SetStartRepetition(pulseInterval, maxNumberOfPulseCycles
                    )
193             ->SetBin(
194                 /* nbins */ maxNumberOfPulseCycles * pulseInterval /
                        200e-9,
195                 /* min */ 0,
196                 /* max */ maxNumberOfPulseCycles * pulseInterval
197             )
198             ->SplitBySubRun()
199         )
200         .Append(StatFunction("Tof", Tof))
201         .Append((new KDIndividualSegmentDraw())
202             ->SetImageFileName(s)
203         )
204         .Append(new KDDraw())
205 
206         // retrieve HV Values //
207         // for exact details, see Beans/Analysis/KDEGunRunCondition.
                cxx
208         .Append(new KDEGunRunCondition())
209 
210         // TOF as a function of surplus energy //
211         .Append((new KDRunSegmentGraph())
212             ->SetXValue("Condition/EGun/StartVoltage")
213             ->SetYValue("Tof")
214             ->SetYAxisRange(-7e-6, 30e-6)
215             ->SetTitle("Time Of Flight")
216             ->SetXAxisTitle("U_{IE} - U_{egun} (V)")
217             ->SetYAxisTitle("Time (s)")
218             ->AddYAxisCursor(0)
219         )
220         .Append(StatFunction("CycleCorrection", CycleCorrection))
```

```
221         .Append((new KDDraw())
222             ->SetImageFileName("TimeOfFlightScan.png")
223         )
224     );
225 
226     beans.Build(argc, argv).Start();
227     return 0;
228 }
```

The following python script is used to execute the program with the correct parameters:

tof-scan-square.py

```
1  import os
2  from collections import OrderedDict
3  
4  CONFIGPATH = os.environ["MYCONFIG"]+"/tof"
5  FILES    = OrderedDict([
6      ('23278', u"phase = 0.0°"),
7      ('23279', u"phase = 1.5°"),
8      ('23280', u"phase = 3.0°"),
9      ('23281', u"phase = 4.5°"),
10     ('23282', u"phase = 6.0°"),
11     ('23283', u"phase = 7.5°"),
12     ('23284', u"phase = 9.0°"),
13     ('23285', u"phase = 10.5°"),
14     ('23286', u"phase = 12.0°"),
15     ('23287', u"phase = 13.5°"),
16     ('23288', u"ramp"),
17     ('23289', u"exp-rise"),
18 ])
19 
20 for run_id in FILES.keys():
21     for pile in ["normal","pile-1","pile-2","pile-3"]:
22         command=CONFIGPATH+"/sds-tof --offline --{0} --output=/data/
               a_fuls01/katrin/tof/scan-square/{1}_{0}.root {1}".format(
               pile,run_id)
23         os.system(command)
```

# A.4. IPython Code for SDS 2 Data Analysis

SDS 2 Time-of-Flight IPython Cell 1

```
#import os
import numpy as np
import Peaberry as pb
from collections import OrderedDict
import pandas as pd
from matplotlib import rcParams
import matplotlib.pyplot as plt
from scipy.optimize import curve_fit
%matplotlib inline
INTERVAL = 1e6 / 24010.  # 24.01 kHz to microseconds
def FindPeaks( y, lag, diff, influence):
    p = y;
    outputmean = pd.rolling_mean(y,lag) # calculate moving mean
    outputstdev = pd.rolling_std(y,lag) # calculate moving stdev

    newMean = np.zeros(len(outputmean)) # new arrays
    newStdev = np.zeros(len(outputmean))
    signals = np.zeros(len(outputmean))
    newMean[lag-1] = outputmean[lag] # mean and stdev from moving
    newStdev[lag-1] = outputstdev[lag]

    for i in xrange(lag,len(outputmean)): # go through data
        if (p[i] > newMean[i-1]+diff*newStdev[i-1]): # if yvalue
           differs more than a certain stdev from previous point
            newMean[i] = (newMean[i-1]  + influence*p[i])/(1+influence
               ) # influencing by peak?
            newStdev[i] = (newStdev[i-1] + influence*np.sqrt((p[i]-
               newMean[i-1])*(p[i]-newMean[i-1])))/(1+influence)
            signals[i] = 1 # we have a signal (peak)
        else:
            newMean[i] = (newMean[i-1]+p[i])/2 # else update mean and
               stdev
            newStdev[i] = (newStdev[i-1] + np.sqrt((p[i]-newMean[i-1])
               *(p[i]-newMean[i-1])))/2
            signals[i] = 0 # no signal
    return signals


class Peak:
    def __init__(self, l, r, x, y):
        self.xdata = x
        self.ydata = y
        self.l = l
```

```
        self.r = r
        self.left = x[0]
        self.right = x[r-l]
        self.width = self.right - self.left
        self.center = (self.left + self.right)/2
        self.area = self.get_area()
        self.wcenter = self.get_wcenter()
        self.ymax = self.get_ymax()
        self.xmax = self.get_xmax()
        self.tof = self.get_tof()

    def get_area(self): #determine peak area
        a = 0.
        for i in xrange(self.r-self.l):
            a = a + self.ydata[i]
        return a

    def get_wcenter(self): #determine weighted center
        k = 0
        t = 0.
        while (t < self.area/2):
            t = t + self.ydata[k]
            k = k + 1
        return self.xdata[k]
    def get_tof(self):
        sum = 0
        tofsum = 0
        for i in xrange(self.r-self.l):
            sum = sum + self.ydata[i]
            tofsum = tofsum + self.ydata[i]*self.xdata[i]
        return tofsum/sum
    def get_ymax(self): #get max yvalue
        return max(self.ydata)

    def get_xmax(self): #get xvalue of max
        return self.xdata[np.argmax(self.ydata)]
```

SDS 2 Time-of-Flight IPython Cell 2

```
pb.Main.SILENT = 4 #switching off messages from peaberry

fig_width_pt = 426.79135
fig_width = fig_width_pt/72.27
fig_height = fig_width*(np.sqrt(5)-1.)/2.
rcParams['pgf.rcfonts'] = False
rcParams['figure.figsize'] = (fig_width, fig_height)
rcParams['text.usetex'] = True
rcParams['mathtext.default'] = "regular"
```

```
rcParams['font.size'] = 12
rcParams['axes.labelsize'] = 12
rcParams['legend.fontsize'] = 12
rcParams['xtick.labelsize'] = 10
rcParams['ytick.labelsize'] = 10
rcParams['backend'] = "pdf"
rcParams['text.latex.preamble'] = [
    r'\usepackage{siunitx}',
    r'\usepackage{textcomp}'
]

colormap = plt.cm.ocean

PREVIEW = True
TITLE   = r""
BASEDIR = '/data/a_fuls01/katrin/tof/scan-square/'
FILES   = OrderedDict([
    ('23278', u"phase = 0.0°"),
    ('23279', u"phase = 1.5°"),
    ('23280', u"phase = 3.0°"),
    ('23281', u"phase = 4.5°"),
    ('23282', u"phase = 6.0°"),
    ('23283', u"phase = 7.5°"),
    ('23284', u"phase = 9.0°"),
    ('23285', u"phase = 10.5°"),
    ('23286', u"phase = 12.0°"),
    ('23287', u"phase = 13.5°"),
])

SURPLUS = {
    #~ 0:  -2.0,
    #~ 1:  -1.5,
    #~ 2:  -1.0,
    #~ 3:  -0.5,
    4:  0.0,
    5:  0.5,
    6:  1.0,
    7:  1.5,
    8:  2.0,
    9:  2.5,
    10: 3.0,
    11: 3.5,
    12: 4.0,
    13: 4.5,
    14: 5.0,
}
#SELECTED_SURPLUS = {4: 0.0,}
```

```
57 SELECTED_SURPLUS = SURPLUS
58 PHASES = {
59     '23278':    0.0,
60     '23279':    1.5,
61     '23280':    3.0,
62     '23281':    4.5,
63     '23282':    6.0,
64     '23283':    7.5,
65     '23284':    9.0,
66     '23285':    10.5,
67     '23286':    12.0,
68     '23287':    13.5,
69     '23288':    0.0,
70     '23289':    0.0,
71     '23290':    0.0,
72     '23291':    0.0,
73 }
74 THRESHOLD = 0. # minimum count value to be accepted as peak
75 AREA_MIN = 0.3 # minimal fraction of the peak with the largest area a
       peak must have to be accepted (0 to deactivate)
76 AREA_MAX = 1. # maximal fraction of the peak with the largest area a
       peak must have to be accepted (1 to deactivate)
77
78 TOFgraphs = {}
79 Peaks = {}
80 Tof = {}
81 #for index,surplus in SURPLUS.items():
82 for index,surplus in SELECTED_SURPLUS.items(): #first surplus energy
       only
83     print "##########################"
84     print "# Surplus : {}V        #".format(surplus)
85     print "##########################"
86     Test = pb.Main.Plot(TITLE)
87     Test.plot["colors"]="ocean"
88     for name,label in FILES.items():
89     #for name,label in OrderedDict([('23278', u"phase = 0.0°"),]).
           items(): #0° only
90         phase = PHASES[name]
91         #if phase != 0.0 and phase != 4.5:
92         #    continue
93         plot = u"Segment%02d/Interval00/Interval00" % index
94         label = r"{0}".format(phase)+"$\si{\degree}$, "+"{0}".format(
               surplus)+"$\,\si{eV}$"
95
96
97         #normal peak
98         hist = pb.Beans.Hist(name,label,plot = Test, fit = None,
```

```
            segmented=True)
99          hist.fromBeans(filename = BASEDIR+name+"_normal.root",
            plotname = plot,yerrors = False)
100         k = 2
101         for pile in ["pile-1","pile-2","pile-3"]: #double, triple,
            quadruple event peaks
102             hist_pile = pb.Beans.Hist(name,label,plot = None, fit =
                None, segmented=True)
103             hist_pile.fromBeans(filename = BASEDIR+name+"_"+pile+".
                root", plotname = plot,yerrors = False)
104             hist_pile.yvalues = k*hist_pile.yvalues #pile-up -> multi
                counting
105             k = k+1
106             #combining histograms
107             hist.stack(hist_pile)
108
109         hist.xvalues = 1e6 * hist.xvalues - INTERVAL/2 #convert to
            microseconds and shift (egun triggering on wrong edge?)
110         while (hist.xvalues[0] < 0.): #move points before t=0s to the
            end of the spectrum
111             hist.addPoint(1000.+hist.xvalues[0], hist.yvalues[0])
112             hist.removePointIndex(0)
113
114         #peakfinding
115         signals = FindPeaks(hist.yvalues,10,3.5,0)
116
117         #optional threshold for peaks
118         for i in xrange(len(signals)):
119             if((signals[i]==1) and hist.yvalues[i]<THRESHOLD):
120                 signals[i]=0
121
122         if not surplus in TOFgraphs:
123             TOFgraphs[surplus] = []
124             Peaks[surplus] = {}
125             Tof[surplus] = {}
126         TOFgraphs[surplus].append(hist)
127
128         if not phase in Peaks[surplus]:
129             Peaks[surplus][phase] = []
130
131         #get data for peaks found above
132         l,r = 0,0
133         a,t = 0.,0.
134         for i in xrange(len(signals)-1):
135             if r > i:
136                 continue
137             if(signals[i] == 1):
```

```
138                 l = i
139                 for j in xrange(i,len(signals)-1):
140                     if(signals[j+1] == 0):
141                         r = j
142                         if (r>l): #optional filtering single bin
                                events
143                             Peaks[surplus][phase].append(Peak(l,r,hist
                                    .xvalues[l:r+1],hist.yvalues[l:r+1]))
144                         break
145
146     Test.xlabel  = u"time of arrival in $\si{\micro s}$"
147     Test.ylabel  = u"electron count"
148     Test.xlimits = [0,1000]
149
150     for i in np.linspace(0.,24010.,num=25,endpoint=True)/1000.:
151         Test.addIndicator(i*INTERVAL,None)
152
153     Test.generate(u"tfToF-spectrum", "phases_%+.1fV"%surplus, preview=
            PREVIEW, filetype='pdf')
154
155
156 for index,surplus in SELECTED_SURPLUS.items():
157     plt.gca().set_color_cycle([colormap(k) for k in np.linspace(0.,
            1., 11)])
158     print "#########################################################"
159     print "#                surplus energy: {} eV                  #".
            format(surplus)
160     print "#########################################################"
161     for name,label in FILES.items():
162         phase=PHASES[name]
163         #if phase != 0.0 and phase != 4.5:
164         #    continue
165         print "#####################################################"
166         print "#                  phase: {} deg                    #".
                format(phase)
167         print "#####################################################"
168         #formating for plots
169         npeaks = len(Peaks[surplus][phase])
170         areas = np.zeros(npeaks)
171         centers = np.zeros(npeaks)
172         weighted_centers = np.zeros(npeaks)
173         tof = np.zeros(npeaks)
174         widths = np.zeros(npeaks)
175         for i in xrange((npeaks)):
176             areas[i] = Peaks[surplus][phase][i].area
177             centers[i] = Peaks[surplus][phase][i].center
178             weighted_centers[i] = Peaks[surplus][phase][i].wcenter
```

```
179             widths[i] = Peaks[surplus][phase][i].width
180             tof[i] = Peaks[surplus][phase][i].tof
181
182         #area filtering
183         marea = areas.max()
184         mask = np.ones(npeaks, dtype=bool)
185         for i in xrange((npeaks)):
186             if(areas[i] < AREA_MIN * marea or areas[i] > AREA_MAX *
                    marea):
187                 mask[i] = 0
188         areas = areas[mask]
189         centers = centers[mask]
190         weighted_centers = weighted_centers[mask]
191         widths = widths[mask]
192         tof = tof[mask]
193
194         #ploting filtered data
195         def fitFunc(x, a, b, c):
196             return a*np.sin(2*np.pi*b/1000.*x)+c
197         plt.plot(weighted_centers-INTERVAL*phase/15.,areas,label=u"{}"
                .format(phase)+"$\si{\degree}$")
198         #tof for peaks
199         print tof
200         Tof[surplus][phase] = tof
201     plt.legend(loc='upper right', numpoints=1)
202     plt.xlabel(u"time of arrival in $\si{\micro s}$ (weighted center)"
            )
203     plt.ylabel(u"counts (peak area)")
204     #plt.title(u"peak area vs time for {}".format(surplus)+"$\,\si{eV}
            $ surplus energy")
205     plt.xlim(0.,1200.)
206     plt.savefig("output/tfToF-peakarea_{:+.1f}V.pdf".format(surplus))
207     plt.show()
208
209 print Tof
210
211 for index,surplus in SELECTED_SURPLUS.items():
212     for name,label in FILES.items():
213         phase = PHASES[name]
214         m = 0.
215         print "simple mean ToF for {} eV surplus and {}° phase shift:"
                .format(surplus,phase)
216         for i in xrange(len(Tof[surplus][phase])):
217             m = m + Tof[surplus][phase][i]
218         m = m/len(Tof[surplus][phase])
219         print "{} us".format(m)
```

## A.5. Run Condition Data for the Split Main Spectrometer

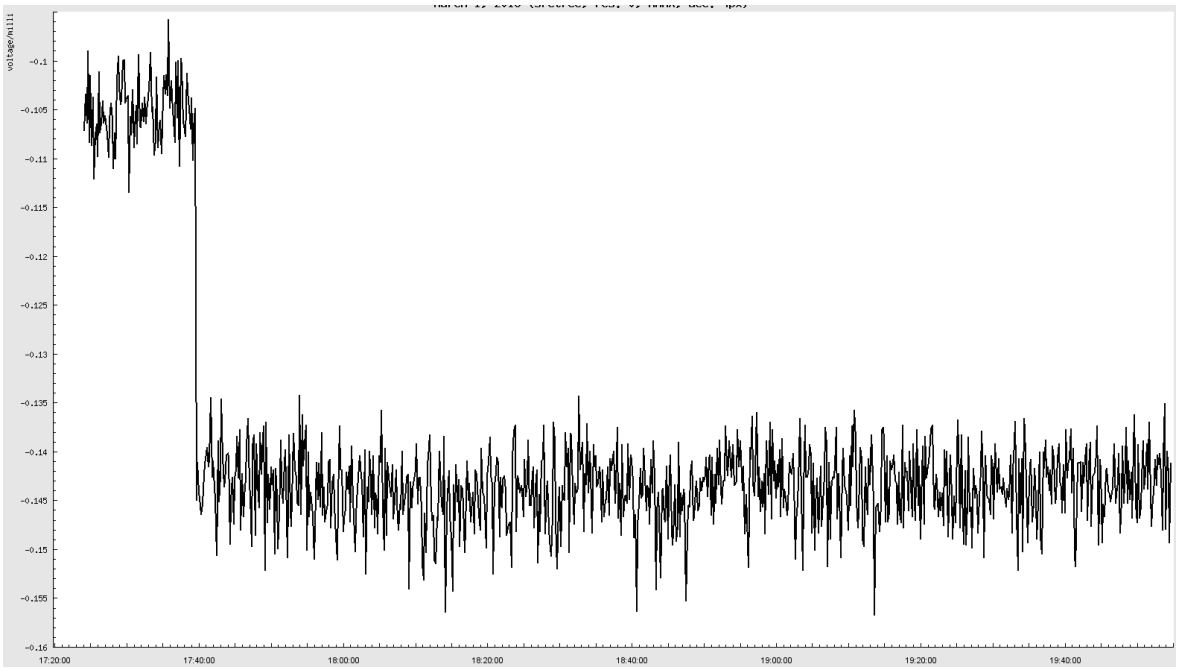


**Figure A.1.** – **Readout of the current amplifier:** A higher light intensity increases the current in the photo diode and corresponds to a larger number of produced electrons. A significant drop can be made out after the first run for $\Delta\phi = 0°$.

# A.6. Split Main Spectrometer Electric Field and Trajectory

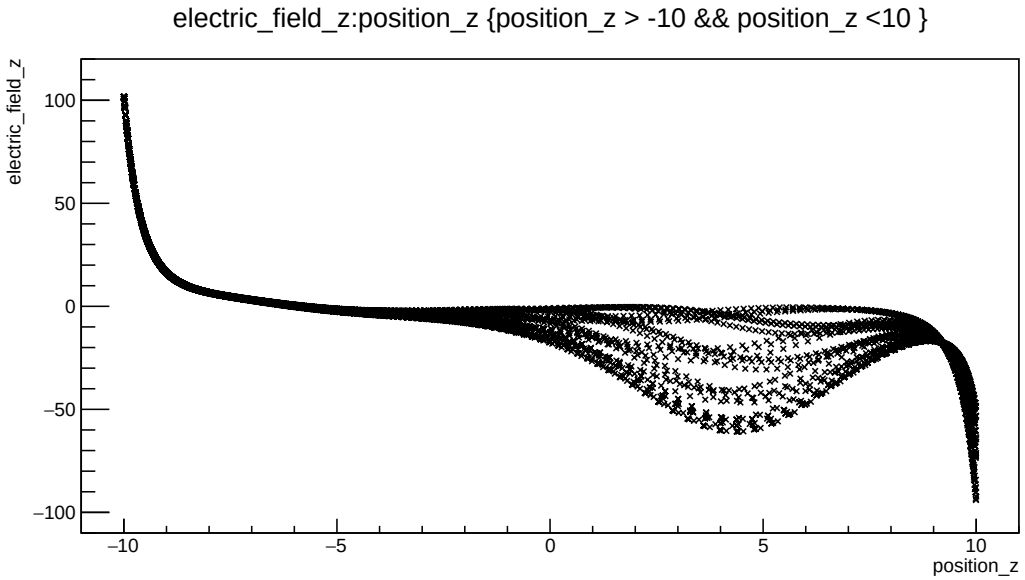


**Figure A.2.** – **Electric field on the axis inside the main spectrometer:** The influence of the accelerating voltage leads to a time-dependent field, plotted here for trajectories of electrons started at different times. The envelope of the plotted curves show the accelerating field at the maximal and minimal potential setting, respectively.

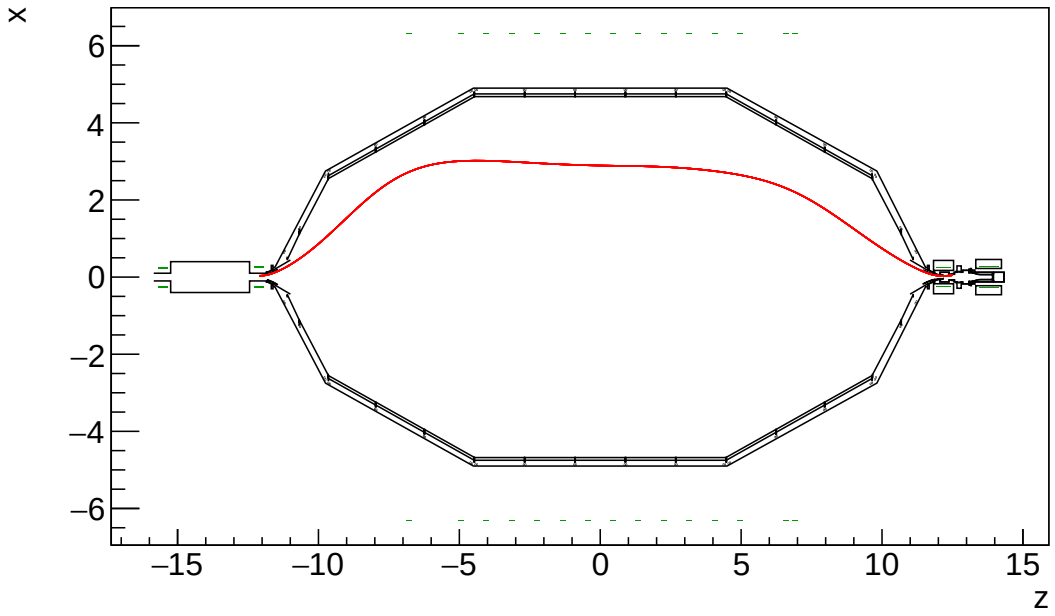


**Figure A.3.** – **Outer trajectory through the split main spectrometer:** Shown here is 2D projection of an example trajectory for an electron, started at $r = 3.5\,\mathrm{cm}$ inside the PS2 magnet, together with the geometry.

## A.7. Third Spectrometer ToA Histograms for TFToF Suitable Parameters

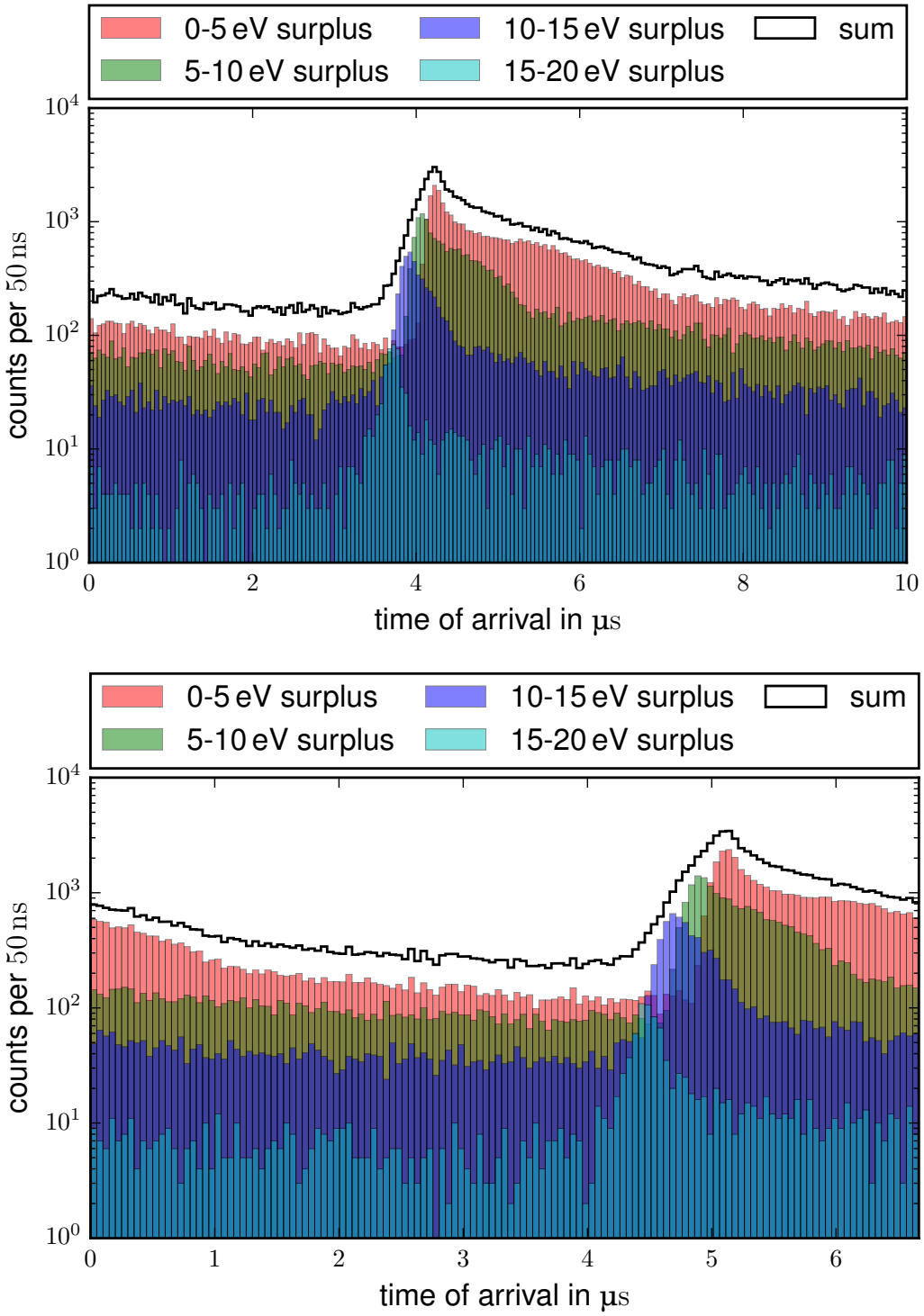


**Figure A.4.** – **Arrival time histograms for TFToF suitable parameters:** For $f = 100\,\mathrm{kHz}$ and $U_{\mathrm{pp}} = 100\,\mathrm{V}$ (top) as well as for $f = 150\,\mathrm{kHz}$ and $U_{\mathrm{pp}} = 50\,\mathrm{V}$ with an additional $+5\,\mathrm{V}$ offset (bottom), electrons with the highest surplus energies are focused at an arrival time where lower energies only give a small contribution to the overall count rate.

# A.8. Endpoint and Neutrino Mass Values for the Pre-Calculation

**Table A.1. – Endpoint and neutrino mass values used in the Kronos sensitivity analysis:** By using every possible combination 841 spectra are obtained, providing the grid points for the Kronos interpolator.

| Endpoint energy $E_0$ in eV | Neutrino mass square $m^2(\nu_e)$ in $eV^2$ |
|---|---|
| 18574.7500 | -0.2500 |
| 18574.8500 | -0.1500 |
| 18574.9000 | -0.1000 |
| 18574.9350 | -0.0650 |
| 18574.9600 | -0.0400 |
| 18574.9750 | -0.0250 |
| 18574.9850 | -0.0150 |
| 18574.9900 | -0.0100 |
| 18574.9935 | -0.0065 |
| 18574.9960 | -0.0040 |
| 18574.9975 | -0.0025 |
| 18574.9985 | -0.0015 |
| 18574.9990 | -0.0010 |
| 18574.9995 | -0.0005 |
| 18575.0000 | +0.0000 |
| 18575.0005 | +0.0005 |
| 18575.0010 | +0.0010 |
| 18575.0015 | +0.0015 |
| 18575.0025 | +0.0025 |
| 18575.0040 | +0.0040 |
| 18575.0065 | +0.0065 |
| 18575.0100 | +0.0100 |
| 18575.0150 | +0.0150 |
| 18575.0250 | +0.0250 |
| 18575.0400 | +0.0400 |
| 18575.0650 | +0.0650 |
| 18575.1000 | +0.1000 |
| 18575.1500 | +0.1500 |
| 18575.2500 | +0.2500 |

## A.9. $\chi^2$ Plots for the Third Spectrometer

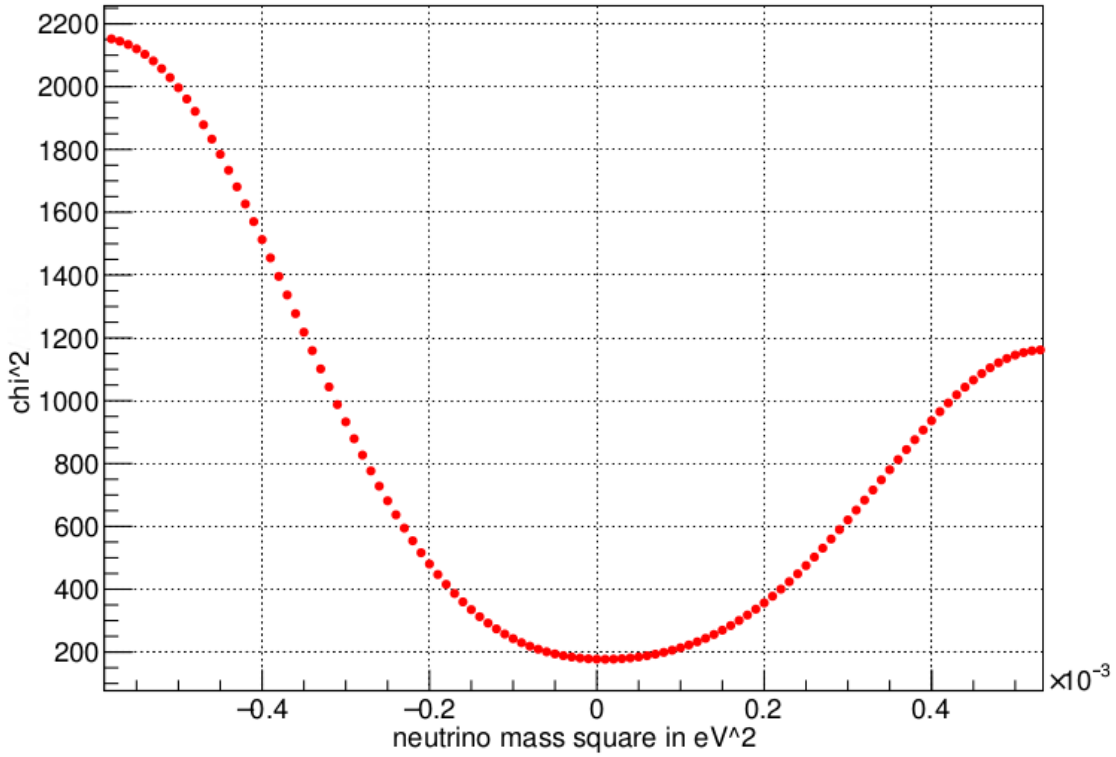


**Figure A.5. – $\chi^2$ behavior in the vicinity of the minimum for three years of measuring time in TFToF mode:** The parabolic increase of $\chi^2$ is very smooth over nearly a complete order of magnitude. Note that $m^2(\nu_e)$ only changes about $5 \cdot 10^{-4}\,\mathrm{eV}^2$ and the large $\chi^2$ difference is due to the random difference between two adjacent spectra.

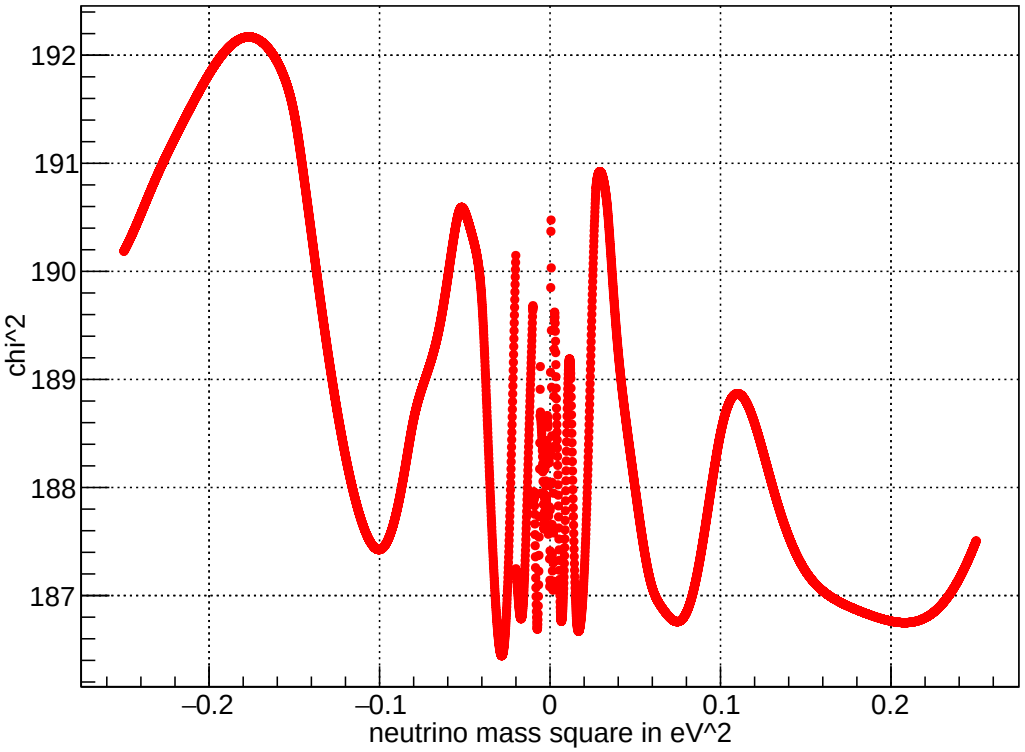


**Figure A.6.** – $\chi^2$ **behavior over the simulated** $\mathbf{m^2}(\nu_e)$ **region for** $\mathbf{N = 10^6}$ **events:** Large random fluctuations make it impossible to obtain a $m^2(\nu_e)$ sensitivity from this plot.

# List of Figures

# List of Tables

# Bibliography


[11] *Operator's Manual, High Voltage Bipolar Power Supply*, Model BOP 500M, BOP 500DM, BOP 1000M, BOP 1000DM Power Supply, 2011, URL: http://www.kepcopower.com/support/2281733-b.pdf (cit. on p. 40).

[Ago+13] M. Agostini et al., *Results on neutrinoless double beta decay of 76Ge from GERDA Phase I*, Phys. Rev. Lett. **111**.122503 (2013), DOI: 10.1103/PhysRevLett.111.122503, arXiv: 1307.4720 [nucl-ex] (cit. on p. 11).

[Ams+15] J. F. Amsbaugh et al., *Focal-plane detector system for the KATRIN experiment*, Nucl. Inst. Meth. A **778** (04/2015), DOI: 10.1016/j.nima.2014.12.116, arXiv: 1404.2925v3 [physics.ins-det] (cit. on pp. 15, 20).

[Ase+11] V. N. Aseev et al., *An upper limit on electron antineutrino mass from Troitsk experiment*, Phys. Rev. D **84**.112003 (2011), DOI: 10.1103/PhysRevD.84.112003, arXiv: 1108.5034 [hep-ex] (cit. on p. 14).

[Beh12] J. D. Behrens, *Simulations of stored electrons in the Penning trap between the KATRIN spectrometers*, Diploma thesis, Münster: Institut für Kernphysik der Westfälischen Wilhelms-Universität, 07/2012 (cit. on pp. 13, 19).

[Beh16] J. D. Behrens, *Design and commissioning of a mono-energetic photoelectron source and active background reduction by magnetic pulse at the KATRIN experiment*, Münster, 2016, in preparation (cit. on pp. 37, 47).

[Bon+99] J. Bonn, L. Bornschein, B. Degen, E. W. Otten, and C. Weinheimer, *A high resolution electrostatic time-of-flight spectrometer with adiabatic magnetic collimation*, Nucl. Instr. Meth. Phys. Res. A **421**.1–2 (1999), pp. 256–265, DOI: 10.1016/S0168-9002(98)01263-7 (cit. on p. 30).

[BPT80] G. Beamson, H. Q. Porter, and D. W. Turner, *The collimating and magnifying properties of a superconducting field photoelectron spectrometer*, J. Phys. E **13**.1 (1980), URL: http://stacks.iop.org/0022-3735/13/i=1/a=018 (cit. on p. 22).

[Cap+14] F. Capozzi, G. L. Fogli, E. Lisi, A. Marrone, D. Montanino, and A. Palazzo, *Status of three-neutrino oscillation parameters*, Phys. Rev. D **89**.093018 (2014), DOI: 10.1103/PhysRevD.89.093018 (cit. on p. 10).

[DON01] The DONUT Collaboration, *Observation of Tau Neutrino Interactions*, Phys. Lett. B **504** (3 04/2001), pp. 218–244, DOI: 10.1016/S0370-2693(01)00307-0, arXiv: hep-ex/0012035v1 (cit. on p. 5).

[Dre+13] G. Drexlin, V. Hannen, S. Mertens, and C. Weinheimer, *Current Direct Neutrino Mass Experiments*, Adv. High Energy Phys. (2013), DOI: 10.1155/2013/293986, arXiv: 1307.0101v1 [physics.ins-det] (cit. on p. 14).

[Eli+15] S. Eliseev et al., *Direct Measurement of the Mass Difference of* $^{163}$Ho *and* $^{163}$Dy *Solves the Q-Value Puzzle for the Neutrino Mass Determination*, Phys. Rev. Lett. **115**.6 (08/2015), p. 062501, DOI: 10.1103/PhysRevLett.115.062501, URL: http://pdg.lbl.gov/2015/reviews/rpp2015-rev-neutrino-mixing.pdf (cit. on p. 12).

[ELOG115] O. Rest, J. Behrens, M. Erhard, S. Dyba, M. Slezak, and C. Weinheimer, *electronic logbook: Time focusing TOF*, 2015, URL: https://neutrino.ikp.kit.edu:8080/SDS-Measurements+Phase+2/115 (cit. on pp. 32, 33, 40).

[ELOG26] J. Behrens and S. Enomoto, *electronic logbook: e-gun pulser latency*, 2014, URL: https://neutrino.ikp.kit.edu:8080/SDS-Measurements+Phase+2/26 (cit. on p. 47).

[G+14] L. Gastaldo, K. Blaum, A. Doerr, et al., *The Electron Capture* $^{163}$*Ho Experiment ECHo*, J. Low Temp. Phys. **176**.876 (2014), DOI: 10.1007/s10909-014-1187-4 (cit. on p. 14).

[Gal+00] M. Galeazzi, F. Fontanelli, F. Gatti, and S. Vitale, *End-point energy and half-life of the 187 Re $\beta$ decay*, Phys. Rev. C **63**.014302 (12/2000), DOI: 10.1103/PhysRevC.63.014302 (cit. on p. 12).

[Gro+11] S. Grohmann, T. Bode, H. Schön, and M. Süßer, *Precise temperature measurement at 30 K in the KATRIN source cryostat*, Cryogenics **51**.8 (2011), DOI: 10.1016/j.cryogenics.2011.05.001, URL: http://www.sciencedirect.com/science/article/pii/S0011227511001135 (cit. on p. 16).

[Gro15] S. Groh, *Modelling of the response function and measurement of transmission properties of the KATRIN experiment*, Ph.D. thesis, Karlsruhe: Institut für Experimentelle Kernphysik - Karlsruher Institut für Technologie, 2015 (cit. on pp. 25, 29, 37).

[Hac15] M. T. Hackenjos, *Die differentielle Pumpstrecke des KATRIN-Experiments, Inbetriebnahme und Charakterisierung des supraleitenden Magnetsystems*, Master's thesis, Karlsruhe: Institut für Experimentelle Kernphysik - Karlsruher Institut für Technologie, 04/2015 (cit. on p. 17).

[Har15] F. T. Harms, *Characterization and Minimization of Background Processes in the KATRIN Main Spectrometer*, Ph.D. thesis, Karlsruhe: Institut für Experimentelle Kernphysik - Karlsruher Institut für Technologie, 2015 (cit. on p. 63).

[Hil11] B. Hillen, *Untersuchung von Methoden zur Unterdrückung des Spektrometeruntergrunds beim KATRIN-Experiment*, Ph.D. thesis, Münster: Fachbereich Physik der Mathematisch-Naturwissenschaftlichen Fakultät der Westfälischen Wilhelms-Universität, 2011 (cit. on p. 19).

[Hug08] K. A. Hugenberg, *Design of the electrode system for the KATRIN main spectrometer*, Diploma thesis, Münster: Institut für Kernphysik - WWU Münster, 01/2008 (cit. on p. 23).

[IPy] *IPython, browser based command shell for interactive computing*, URL: https://ipython.org/ (cit. on p. 47).

[Kasper-git] *Kasper source code*, URL: https://nuserv.uni-muenster.de:8443/katrin-git/kasper (cit. on p. A1).

[Kat04] The Katrin Collaboration, *KATRIN Design Report 2004*, 2005, URL: http://primo.bibliothek.kit.edu/primo_library/libweb/action/dlDisplay.do?vid=KIT&docId=KITSRCE0270060419&tab=kit_evastar&srt=date (cit. on pp. 15, 16, 18, 70).

[KAT06] KAT Komitee für Astroteilchenphysik, *Kosmische Spurensuche: Astroteilchenphysik in Deutschland, Ein Forschungsgebiet im Aufbruch*, Forschungszentrum Karlsruhe in der Helmholtz-Gemeinschaft, 2006 (cit. on p. 7).

[Kat16] *KATRIN homepage*, URL: `http://www.katrin.kit.edu` (visited on 07/16/2016) (cit. on pp. 17, 18).

[Kle14] M. Kleesiek, *A Data-Analysis and Sensitivity-Optimization Framework for the KATRIN Experiment*, Ph.D. thesis, Karlsruhe: Institut für Experimentelle Kernphysik - Karlsruher Institut für Technologie, 2014 (cit. on p. 46).

[Kra+05] C. Kraus et al., *Final Results from phase II of the Mainz Neutrino Mass Search in Tritium $\beta$ Decay*, Eur. Phys. J. C **40** (2005), pp. 447–468, DOI: `10.1140/epjc/s2005-02139-7`, arXiv: `hep-ex/0412056` (cit. on p. 14).

[Kronos-git] *Kronos source code*, the additional TFToF code is available in the afulst_tftof branch, URL: `https://nuserv.uni-muenster.de:8443/katrin-git/kronos` (cit. on p. 70).

[LeB10] F. LeBlanc, *An Introduction to Stellar Astrophysics*, WILEY, 04/2010 (cit. on p. 5).

[MINUIT] F. James, *MINUIT, Function Minimization and Error Analysis*, Reference Manual, version 94.1, CERN Geneva, Switzerland, URL: `https://root.cern.ch/sites/d35c7d8c.web.cern.ch/files/minuit.pdf` (cit. on pp. 69, 70).

[Oli+14] K. A. Olive et al., *Review of Particle Physics*, Chin. Phys. C **38**.090001 (2014), DOI: `10.1088/1674-1137/38/9/090001`, URL: `http://pdg.lbl.gov/2015/reviews/rpp2015-rev-neutrino-mixing.pdf` (cit. on p. 10).

[OpenMP] ***Open Multi-Processing**, specification for a set of compiler directives, library routines, and environment variables that can be used to specify high-level parallelism in C++ programs*, URL: `http://openmp.org/wp/` (cit. on p. 70).

[OW08] E. W. Otten and C. Weinheimer, *Neutrino mass limit from tritium $\beta$-decay*, Rep. Prog. Phys. **71**.8 (07/2008), DOI: `10.1088/0034-4885/71/8/086201`, arXiv: `0909.2104v1 [hep-ex]` (cit. on pp. 6, 12).

[Pau30] W. Pauli, *Offener Brief an die Gruppe der Radioaktiven bei der Gauvereins-Tagung zu Tübingen*, 12/04/1930 (cit. on p. 5).

[Py] *Python, programming language*, URL: `https://www.python.org/` (cit. on p. 47).

[RC59] F. Reines and C. L. Cowan, *Free Antineutrino Absorption Cross Section. I. Measurement of the Free Antineutrino Absorption Cross Section by Protons*, Phys. Rev. **113**.273 (01/1959), DOI: `10.1103/PhysRev.113.273` (cit. on p. 3).

[RC97] F. Reines and C. L. Cowan, *The Reines-Cowan experiments: Detecting the Poltergeist*, Los Alamos Sci. 25 (1997) (cit. on p. 4).

[Res15] O. Rest, *private communication*, 2015 (cit. on p. 34).

[ROOT] *ROOT - An Object-Oriented Data Analysis Framework*, URL: `https://root.cern.ch/` (cit. on p. 37).

[Sør+12] S. Riemer-Sørensen et al., *WiggleZ Dark Energy Survey, Cosmological neutrino mass constraint from blue high-redshift galaxies*, Phys. Rev. D **85**.081101 (2012), DOI: `10.1103/PhysRevD.85.081101`, arXiv: `1112.4940 [astro-ph.CO]`, URL: `http://pdg.lbl.gov/2015/reviews/rpp2015-rev-neutrino-mixing.pdf` (cit. on p. 11).

[SK12] The Super-Kamiokande collaboration, *Neutrin 2010 Results from Super-Kamiokande*, Nucl. Phys. B (Proc. Suppl.) **229** (2012), DOI: `10.1016/j.nuclphysbps.2012.09.013`, arXiv: `1112.3425v1 [hep-ex]` (cit. on p. 8).

[SK98] The Super-Kamiokande Collaboration, *Evidence for Oscillation of Atmospheric Neutrinos*, Phys. Rev. Lett. **81** (8 1998), DOI: `10.1103/PhysRevLett.81.1562` (cit. on pp. 1, 8).

[SNO01] The SNO collaboration, *Measurement of the rate of* $\nu_e + d \rightarrow p + p + e^-$ *interactions produced by* $^8B$ *solar neutrinos at the Sudbury Neutrino Observatory*, Phys. Rev. Lett **87**.071301 (2001), DOI: `10.1103/PhysRevLett.87.071301`, arXiv: `nucl-ex/0106015` (cit. on p. 1).

[SNO13] The SNO collaboration, *Combined Analysis of all Three Phases of Solar Neutrino Data from Sudbury Neutrino Observatory*, Phys. Rev. C

**88**.025501 (2013), DOI: 10.1103/PhysRevC.88.025501, arXiv: 1109.0763 [nucl-ex] (cit. on p. 9).

[Ste+13] N. Steinbrink, V. Hannen, E. L. Martin, R. G. H. Robertson, M. Zacher, and C. Weinheimer, *Neutrino mass sensitivity by MAC-E-Filter based time-of-flight spectroscopy with the example of KATRIN*, New J. Phys. **15**.11 (2013), DOI: 10.1088/1367-2630/15/11/113020 (cit. on pp. 27, 28, 30, 69).

[Val14] K. Valerius, *Status of the Karlsruhe Tritium Neutrino Experiment KATRIN*, in: *DESY-PROC-2014-04*, Hamburg, 2014, DOI: 10.3204/DESY-PROC-2014-04/80, URL: http://www-library.desy.de/preparch/desy/proc/proc14-04.html (cit. on p. 18).

[Wei16] C. Weinheimer, *Time-of-flight spectroscopy at KATRIN with a DC tagger, talk held at the 30th KATRIN Collaboration Meeting*, 03/2016 (cit. on pp. 33, 36).

[Wes15] J. Wessels, *Skript zur Vorlesung: Kern- und Teilchenphysik I - WS14/15*, 2015, URL: http://qgp.uni-muenster.de/~weinheim/lehre/ss15/lowE/ (cit. on p. 8).

[Win14] D. Winzen, *Development of an angular selective electron gun for the KATRIN main spectrometer*, Diploma thesis, Münster: Institut für Kernphysik der Westfälischen Wilhelms-Universität, 03/2014 (cit. on p. 32).

[Zac09] M. Zacher, *Electromagnetic design and field emission studies for the inner electrode system of the KATRIN main spectrometer*, Diploma thesis, Münster: Institut für Kernphysik der Westfälischen Wilhelms-Universität, 2009 (cit. on p. 20).

[Zac14] M. Zacher, *High-field electrodes design and an angular-selective photoelectron source for the KATRIN spectrometers*, Ph.D. thesis, Münster: Fachbereich Physik der Mathematisch-Naturwissenschaftlichen Fakultät der Westfälischen Wilhelms-Universität, 2014 (cit. on p. 32).